Summer 2022

Spectral Variability in Naturally Weathered Rock Surfaces and Implications for Mars

Sabrina Curtis
Western Washington University, sacurtis004@gmail.com

Recommended Citation

Curtis, Sabrina, "Spectral Variability in Naturally Weathered Rock Surfaces and Implications for Mars" (2022). *WWU Graduate School Collection*. 1118.
https://cedar.wwu.edu/wwuet/1118

Spectral Variability in Naturally Weathered Rock Surfaces and Implications for Mars

By

Sabrina Curtis

Accepted in Partial Completion
of the Requirements for the Degree
Master of Science

ADVISORY COMMITTEE

Dr. Melissa Rice, Chair

Dr. Michael Kraft

Dr. Sean Mulcahy

GRADUATE SCHOOL

David L. Patrick, Dean

Master's Thesis

Sabrina Curtis

July 1, 2022

Spectral Variability in Naturally Weathered Rock Surfaces and Implications for Mars

A Thesis
Presented to
The Faculty of
Western Washington University

In Partial Fulfillment
Of the Requirements for the Degree
Master of Science

by
Sabrina Curtis
July 2022

ABSTRACT

Rock weathering products are important clues for understanding past environmental conditions on Mars. They can be identified using reflectance spectroscopy because the formation of new minerals and textures on a rock surface will change its spectral signature. Previous studies demonstrate that the spectral signature of coated rock surfaces can vary with viewing geometry (the angle between incident and emitted light); however, these photometric effects have not been extensively characterized for naturally weathered rocks. My goal in this study is to quantify how both weathering and viewing geometry affect visible to near-infrared (VNIR) reflectance spectra of a subset of naturally weathered igneous rocks. Improving our understanding of how weathering changes the spectral signature of terrestrial samples can be applied to Martian rocks to make inferences about their original compositions and the environmental conditions that formed any weathering products present.

I compared weathered surface compositions and textures to their unweathered rock interiors using powder X-ray diffraction (XRD), petrographic analysis of thin sections, and scanning electron microscopy (SEM) with energy dispersive spectroscopy (EDS). Differences between the surfaces and interiors are primarily textural with minor compositional variations. Weathering rind mineralogy is made up of majority primary minerals, with small volumes of secondary clays and Fe-oxides. Weathered surfaces show increased microfracturing and porosity in their rinds, especially within 1-2 mm of surfaces and macroscale fractures. I used Western Washington University's hemispheric spectrogoniometer to collect reflectance spectroscopy data from natural and cut rock surfaces at many viewing geometries covering the full scattering hemisphere. Additionally, I convolved lab spectra to Mastcam-Z wavelengths and compared them to Mastcam-Z spectra from olivine-bearing rocks in the South Séítah region within Jezero crater on Mars.

Viewing geometry findings indicate that spectra taken outside a lab standard geometry (e.g. i=30, e=0, az=0) allow for accurate mineral identification. Using band depth, magnitude of reflectance, or near-infrared slope to interpret differences between spectral observations is not recommended, however, if the spectra were collected at widely different phase angles. Band depths decrease and near-infrared slopes are more positive (red sloped) with increasing phase angle regardless of a sample's surface weathering or scattering behavior. Absorption band center positions can shift slightly with phase angle due to noise and sample heterogeneity, but changes are small with no correlation to viewing geometry. Minor compositional differences between samples create strong signals in the spectral data; thin, intermittent Fe-oxide coatings on a surface begin to mask the sample's primary mineralogy. Relatively unweathered samples tend to be more forward scattering, while weathered samples tend to be more backscattering. This is likely due to surface roughness and near-surface microporosity differences. Direct applications of these findings include making surface texture inferences based on remote phase angle experiments, especially for the olivine-bearing Séítah rocks.

ACKNOWLEDGEMENTS

I would like to thank my advisor, Melissa Rice, and my committee, Michael Kraft and Sean Mulcahy, for their support and guidance throughout this project. Their feedback and encouragement during the writing process has been invaluable. Thank you to Kristiana Lapo for helping collect the spectral data, and to Louise Duflot and Max Gabbert for their help collecting the rock composition and texture data. And thank you to Ben Paulson for making sure I always had the equipment and training I needed to process my samples, and for coordinating department Covid protocols to ensure those of us working on-campus during the height of the pandemic were as safe as possible.

Funding for this project was provided by a NASA Solar Systems Workings program grant and a Geological Society of America Graduate Student Research Grant.

TABLE OF CONTENTS

LIST OF FIGURES

LIST OF TABLES

INTRODUCTION

Mars is a planet of interest, across many scientific fields, because of its potential to preserve evidence of past life outside of Earth. Additionally, studying the geology of Mars is important in and of itself, even if life is never found on the planet, because understanding the planet's surface and climate history will aid in future human exploration of Mars. Studying other planets and rocky bodies in our solar system is necessary for understanding aspects of our own planet's geologic history. We can estimate Earth's bulk composition based on the composition of meteorites originating from asteroids that formed in the same region as the Earth. Bulk composition data is relevant to many fields in geology. For example, studies of the Earth's formation and evolution use comparisons between the current upper mantle composition sampled through rocks that have made their way to the surface and the mantle's original composition which is based on meteorite data. Our planetary neighbors also give insight into other planetary aspects of planetary evolution: Mars' small size and distance from the Sun means it is cold and dry with very little atmosphere today, while Venus is similar to Earth in size but has extremely high surface temperatures and pressure due to its thick insulating clouds. Understanding their atmospheric systems helps us constrain models of potential paths the Earth's climate could take in the future.

Several Mars research missions are currently active and sending data about its surface back to Earth, including NASA's Perseverance Rover. Visible and near-infrared (VNIR) spectroscopy is one technique used to study Mars' surface; Mastcam–Z and SuperCam on the Perseverance rover contribute to spectral observations of Mars rocks. Mastcam-Z is a pair of multispectral imaging cameras that cover wavelengths between 400-1020 nm (Bell et al., 2021). SuperCam is a spectrometer covering 400-850 nm and 1,300-2,600 nm wavelengths (Maurice et al., 2021). Together they cover most of the VNIR range. One of Mastcam-Z's main goals is to characterize Mars' geomorphology, landscape processes, and geologic record (Bell et al., 2021). In addition to the Perseverance and Curiosity rovers, VNIR spectrometers are included on orbiters. The Compact Reconnaissance Imaging Spectrometer for Mars (CRISM) on the Mars Reconnaissance Orbiter (MRO) and the Observatoire pour la Minéralogie, l'Eau, les Glaces et l'Activité (OMEGA) on Mars Express are VNIR spectrometers that have mapped the surface to create planet-wide mineralogical datasets.

Understanding the textures and compositions of rocks on the Martian surface is a key piece to understanding the bigger picture of the planet's geologic history. Previous studies have used VNIR spectroscopy to identify rocks and minerals on Mars' surface (e.g. Fischer and Pieters, 1993; Ehlmann et al. 2009, 2010; Ehlmann and Edwards, 2014). Successfully interpreting VNIR data requires an understanding of instrument variables and natural processes that alter rock surface textures and mineralogy. An instrument's viewing geometry (the angle between incident and reflected light) can change the measured reflectance spectrum from a surface (e.g., Fischer and Pieters, 1993; Hoza, 2019). Rock surface alteration also affects the resulting reflectance spectrum and can obscure the spectral signature of the underlying rock (e.g. Fischer and Pieters, 1993; Minitti et al., 2007; Salvatore et al., 2013).

Understanding weathering products present on the surfaces of Martian rocks and how they interact with our remote sensing techniques is a key piece in understanding Mars' geologic history as a whole; they tell us about processes and conditions in the environment where they formed. Past studies have explored how weathering affects the spectra of terrestrial rocks (e.g. Michalski et al., 2006; Minitti et al., 2007; Horgan et al. 2017; Zhou and Wang, 2017) and how viewing geometry changes affect the spectra of simple synthetic coatings (e.g. Fischer and

Pieters, 1993; Johnson et al., 2004). Recently, Yang et al. (2020) studied the effect of phase angle on spectra of *in situ* Lunar regolith with a limited range of viewing geometries. To our knowledge, no studies have investigated complex, naturally weathered surfaces at many geometries.

In this study, I use terrestrial analogs for Martian rocks to probe the relationship between weathering products, viewing geometry, and reflectance spectra. I collected VNIR spectra at many viewing geometries from naturally weathered terrestrial analogs for Martian rocks using a hemispheric spectrogoniometer. My goal is to answer the question: *What are the combined effects of rock surface alteration and viewing geometry on the spectral signature of naturally weathered, igneous rock surfaces?* Here 'rock surface alteration' refers to the combined effects of rock coatings deposited on a rock surface, the breakdown of a rock surface through physical weathering, and the dissolution and neoformation of minerals near or on a rock surface through chemical weathering. More specific questions that helped guide my exploration of rock surface alteration and viewing geometry include: *Where is reddening/weathering occurring in the rocks?;* and *How much are key spectral parameters for mineral identification - such as absorption band center - affected by viewing geometry?* Answering these questions will benefit future spectroscopic studies of weathered rocks in general by providing a starting point for building hypotheses about how other rock and weathered surface types interact with light at many viewing geometries. My findings will aid Mars exploration specifically by (1) acting as a reference for what could be occurring within a rock if the spectra recorded here are found to be very similar to spectral observations of Martian samples, and by (2) creating testable hypotheses for using viewing geometry to make inferences about *in situ* surface alteration on Mars.

BACKGROUND

Mars Geology Overview

Mars' upper crust is primarily basaltic with local heterogeneity (e.g. Ehlmann and Edwards, 2014). Variations in amounts of plagioclase, pyroxene, and olivine indicate differences in igneous processes on the regional scale; similarly, locally silicic rock have been found, including in Gale and Gusev craters (e.g. Ehlmann and Edwards, 2014; Sautter et al., 2015). Rocks from the oldest Noachian crust include low-Ca pyroxenes and are enriched in olivine (e.g. Ehlmann and Edward, 2014). Basalts in the southern highlands are plagioclase and clinopyroxene dominant, while the northern lowlands have the lowest pyroxene abundances and spectra from the region include signatures of high-silica phases (e.g. Ehlmann and Edwards, 2014). The current understanding is that high-silica phases are the result of aqueous alteration that formed phyllosilicates and/or Si-rich coatings on weathered basalt surfaces (e.g. Wyatt and McSween, 2002; Kraft et al., 2003).

Oxides are common across Mars, including the fine-grained red dust that covers much of the surface and is composed of ferric oxides and oxyhydroxides (e.g. Ehlmann and Edwards, 2014). Clays found in Noachian rocks (3.7+ Ga) indicate there was long-term interaction between rock and liquid water early in Mars' history (e.g. Mustard et al., 2008; Ehlmann et al., 2011; Ehlmann and Edwards, 2014). This could have been from hydrothermal groundwater circulation or surface water interactions (e.g. Ehlmann et al., 2011; Salvatore and Christensen, 2014). Through most of Mars' history, surface water-rock interactions would have been in vapor or ice form, with episodic melting creating liquid water (e.g. Ehlmann et al., 2011). Additional minerals present in some locations include carbonates, sulfates, chlorides, and silica (e.g. Ehlmann and Edwards, 2014).

Previous studies have shown that acidic weathering is likely dominant on Mars (e.g. Hurowitz et al., 2006; Hurowitz and McLennan, 2007; Horgan et al., 2017). Low pH and sulfuric environments, like those expected on Mars, promote dissolution of olivine and apatite, while low water to rock ratios keep reactions speeds slow and resistant minerals (plagioclase, pyroxene, etc.) are unable to contribute much to secondary mineral formation (Hurowitz and McLennan, 2007). As a result, many alteration products on Mars are Mg-sulfates and Fe-oxides, unlike Earth where clays and Al-oxides are common (Hurowitz and McLennan, 2007).

Palagonite is an amorphous alteration product of igneous glass that forms through low-temperature hydrothermal alteration that can also form in semiarid conditions at slower rates (e.g. Singer, 1982). Palagonite from Hawaii has been proposed as an analog for Martian soils (Singer, 1982), and is an example of a terrestrial sample that can act as an analog for Mars despite forming in a different environment. There are also localized areas on Mars where conditions are less acidic and more like terrestrial weathering environments (e.g. Elhmann et al., 2009). For example, alteration minerals found at Nili Fossae are believed to have formed under neutral to alkaline conditions instead of acidic (e.g. Elhmann et al., 2009).

This study looks at three suites of rocks: dunites, basalts, and andesites. Basalts were selected to represent most rocks on Mars' surface, while dunites and andesites were selected to cover a wide range of compositional end members. Previous studies identified weathered Columbia River Basalts as possible spectroscopic analogs for Martian basalts (e.g. Michalski et al., 2006; Hoza, 2019). Weathered Table Mountain andesites and Twin Sisters dunites were selected based on their intermediate and ultramafic compositions and ease of travel to sampling sites. Over the past year the inclusion of dunites has proven to be a good choice; layered rocks in the South Séítah region within Jezero crater on Mars have Mastcam-Z spectra consistent with weathered ultramafic rocks (Rice et al., 2022a).

Perseverance and Séítah

The Perseverance rover launched in the summer of 2020 and landed on Feb. 18th, 2021 in Jezero crater at the edge of Mars' Isidis basin. The mission's overarching goals are to search for signs of past life and collect samples for potential return to Earth as part of a future mission. Mastcam-Z supports the mission goals and rover operations by characterizing the geologic setting around the rover through multispectral images of rocks, outcrops, and soil; this provides scientific context for rover navigation (Bell et al., 2020).

Prior to Perseverance's landing on Mars, orbiter observations detected carbonates with a possible fluvio-lacustrine origin due to their proximity to Jezero's delta (e.g. Horgan et al., 2020). Basement rocks were predicted to have a primitive igneous composition based on a spectral signature consistent with low-Ca pyroxene (e.g. Horgan et al., 2020). Most notably for this study are strong olivine spectral signals indicating an olivine-bearing unit (e.g. Horgan et al., 2020). Once on the surface, the rover confirmed that some rock surfaces in the Séítah formation are olivine-like with abrasion patches and drill tailings showing the most olivine-like spectra (e.g. Nuñez et al., 2022; Rice et al., 2022a).

Spectroscopy Overview

Visible and near-infrared (VNIR) reflectance spectroscopy is a remote sensing method used to study the mineralogy of rocks on Earth and Mars (e.g., Clark, 1999). Reflectance spectroscopy works by sending light of known wavelengths to a surface and measuring the amount of each wavelength of light that is reflected off the surface and received by a detector.

Some of the light will not be reflected and will instead be absorbed by or transmitted through the surface. A reflectance spectrum can be created from the reflected light measured by a detector; different surface types will result in different spectra. Texture (e.g. grain size) and mineralogy (e.g. mixtures of minerals) both affect the reflectance of rock surfaces (Clark, 1999). Dips in a spectrum indicate a surface is absorbing light at those specific wavelengths and can be key features for mineral identification.

Viewing Geometry

Reflectance spectra give clues to the mineralogy of weathering products and underlying rock (e.g., Fischer and Pieters, 1993, Salvatore et al., 2013), but changes in viewing geometry can affect the measured reflectance spectrum of a surface (e.g., Fischer and Pieters, 1993; Johnson and Grundy, 2001). Viewing geometry (also called phase angle or viewing angle) refers to the angle between the incident light and the reflected light (Figure 1). The “standard” viewing geometry in laboratory measurements places the incident light at 30 degrees from vertical, and the detector for measuring reflected light at 0 degrees. On Mars, the incident light comes from the Sun, and the reflected light is measured with instruments on a rover or satellite. However, the many operations and science tasks scheduled for Perseverance and other rovers/orbiters to complete each sol (a Martian day) make it logistically impossible for multispectral images to be taken in the exact same viewing geometry every time. This makes understanding the relationship between viewing geometry and the measured reflectance of any given rock target critically important.

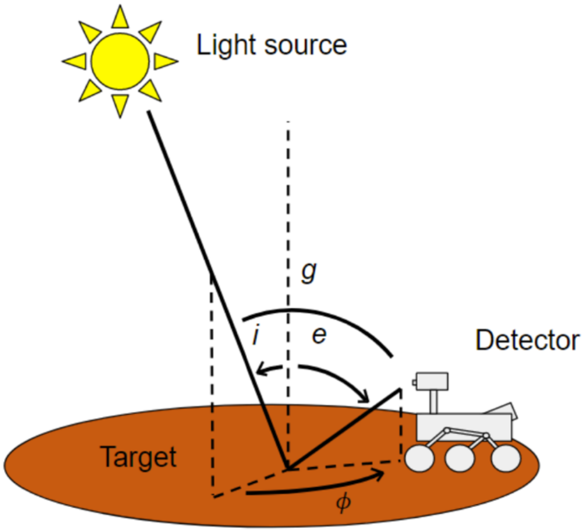

Figure 1: A diagram of how light's incidence angle (i) and reflected angle (e) contribute to the viewing geometry (g). The azimuth (phi) is the angle between i and e in the horizontal plane. Credit: Hoza (2019)

Simple Coatings and Viewing Geometry

Additionally, studies have looked at how simple coatings are affected by viewing geometry (e.g. Fischer and Pieters, 1993; Hoza, 2019). Figure 2 shows an example of the difference viewing geometry alone can make in recorded spectra without alteration to surface texture or composition. Johnson et al. (2004) were able to successfully determine the compositions of a thin coating and the substrate rock using a two-layer model to interpret the reflectance spectrum from the sample.

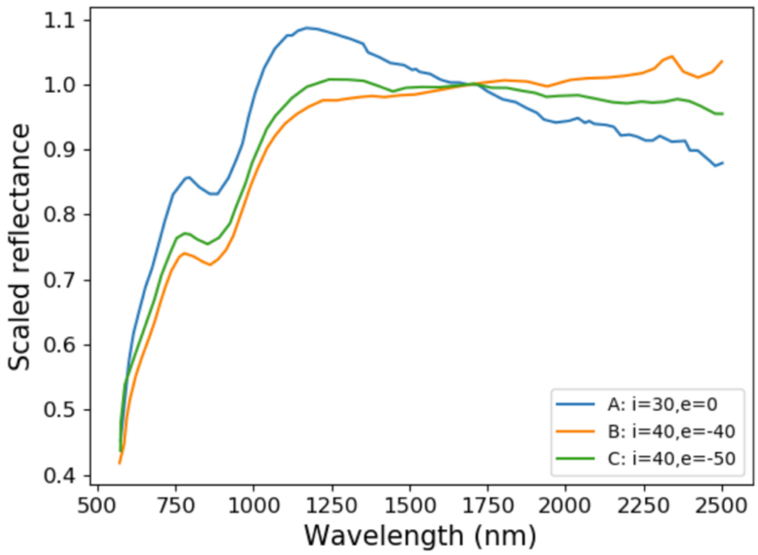

Figure 2: Scaled reflectance of a basalt slab coated in a 225 µm ferric powder. The three curves represent three different viewing geometries: specular (a), forward-scattering (b), and standard (c). Credit: Hoza (2019) using data from Fischer and Pieters (1993).

A Hemispheric Spectrogoniometer

Hoza (2019) developed a custom automated planar (two-dimensional) goniometer for collecting reflectance spectra from rock surfaces. The goniometer can be programmed to automate the collection of spectra from several surfaces at many viewing geometries within a plane. Hoza (2019) collected reflectance spectra from a series of synthetically coated and naturally weathered basalts using the planar goniometer. Her results demonstrate the changes in rock spectral properties with changing viewing geometry. I expand on that work by including a wider range of naturally weathered surfaces across three rock types, and by increasing the number of viewing geometries using WWU's new hemispheric (three-dimensional) automated goniometer (Figure 3). The new goniometer allows for adjustments to the azimuth angle in addition to the incidence and emission angles. The hemispheric goniometer has stages for up to five samples that it can cycle through while automatically collecting reflectance spectra over however many viewing geometries are selected (Rice et al., 2022b).

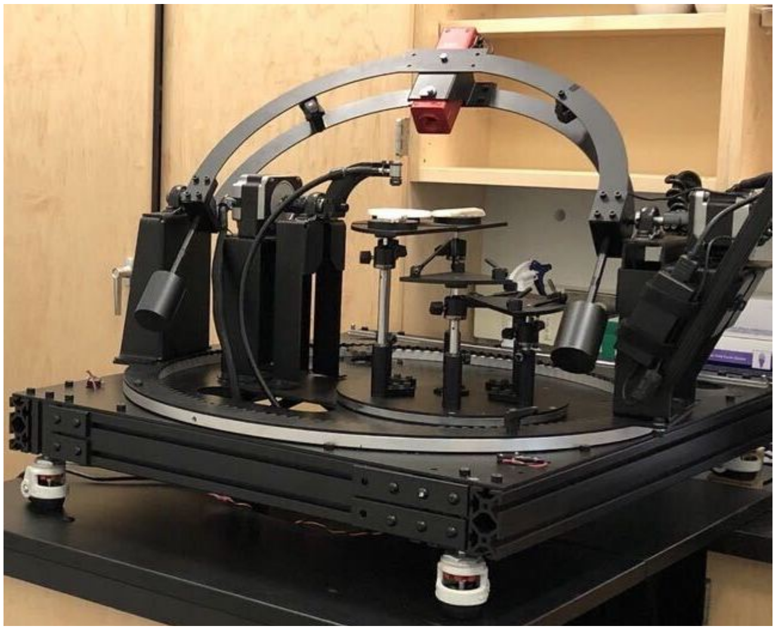

Figure 3: WWU’s new hemispheric goniometer. Photographer: Kristiana Lapo.

Rock Weathering

Previous studies have explored the ways Martian rocks could change as a result of weathering using terrestrial analogs (e.g. Minitti et al., 2007; Greenburger et al., 2012; Salvatore et al., 2013). Minitti et al. (2007) explored how simple coatings over basaltic rocks affect reflectance spectra collected from the rocks. They found that even very thin coatings (3-80 µm thick) were able to partially to completely obscure the VNIR spectral signature of underlying basalt (Minitti et al., 2007). Salvatore et al. (2013) explored the effects of leaching on spectra from Antarctic dolerite and found that even very small changes in composition between the interior and weathered surface created big changes in the spectral signature. VNIR spectra from Columbia River Basalts show weathered surfaces with redder and brighter surfaces than fresh surfaces, but clay precursors hinted at in thermal infrared spectra are not present in the VNIR data (Michalski et al., 2006). Colman (1982) attributes the alteration colors on weathered surfaces to oxidation of volcanic glasses and olivines.

Rocks with complex weathering rinds tend to gradually shift from a relatively unaltered interior to an altered exterior that can look very different from the original rock (e.g. Colman, 1982; Eggleton, 1987; Nesbitt and Wilson, 1992) (Figure 4). Weathering causes changes to rock surfaces that can include: grain coatings, weathering products finely intermixed with primary rock minerals, and micrometer-scale textures, all of which affect spectra and obscure the underlying rock to varying degrees, depending on viewing angle. For example, as grain size decreases, the amount of light reflected off a rock surface will increase (Clark, 1999).

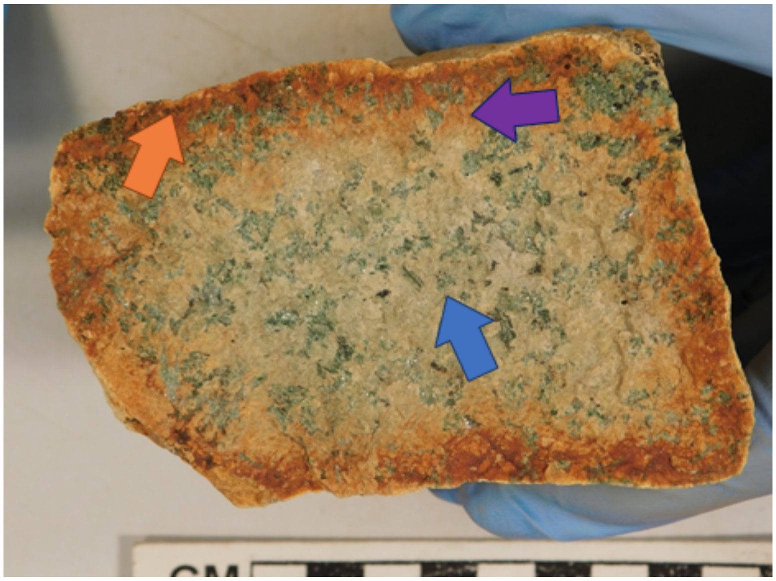

Figure 4: Photo of a Twin Sisters dunite sample with a bright orange weathered exterior (orange arrow) and a relatively unaltered green interior (blue arrow). An approximately 2 cm thick gradient between the two is present (purple arrow).

Several studies have classified the formation of weathering rinds as a degradational process that primarily alters the rock texture with only minor formation of secondary minerals (e.g. Colman, 1982; Salvatore et al., 2013). Alteration starts along grain boundaries and within fractures in a rock (Colman, 1982). Olivine's weathering path is particularly important here because the dunites are primarily olivine. During incipient weathering olivine alters through Fe-oxidation and a breakdown of the olivine structure into a mix of microcrystalline, amorphous weathering products referred to as “iddingsite” (e.g. Colman, 1982; Smith et al., 1987). Extensive weathering of olivine leads to the formation of goethite, Fe-rich smectite, and eventually halloysite (Smith et al., 1987).

Incipient weathering of basalt and andesite proceeds through hydrolysis, leaching, oxidation, and/or destruction of primary minerals (Colman, 1982). Expected weathering products at this stage are amorphous and microcrystalline, including allophane (hydrated Al-silicate), Fe-oxides and hydroxides, poorly developed clays, and palagonite (Colman, 1982). In incipient weathering, Fe oxidation and the incorporation of water alter primary minerals, and discoloration is the result of glass alteration (Colman, 1982). Olivine and glass are the least stable phases and will tend to alter first, followed by pyroxene and plagioclase, with titanomagnetite left behind as the phase most resistant to alteration (Colman, 1982). If conditions allow for allophane and other amorphous weathering products to dehydrate and crystallize, then clay minerals will form (Colman, 1982). When clays begin to form, Fe-bearing smectites (mainly nontronite) are the first expected in weathered basalts (Baker and Neill, 2017). Continued, extensive weathering will eventually increase the permeability of a rock through leaching; at that point aluminous clays (e.g. kaolinite and montmorillonite) can form (Baker and Neill, 2017).

SAMPLE DESCRIPTIONS

Twin Sisters Dunites

The first group of samples are ultramafic rocks from Twin Sisters quarry in western Washington. At the sample site, samples were collected from exposed cobbles within the quarry. Many of the weathered surfaces are a bright orange, and cross sections of the weathering rinds show a gradational transition to green interiors with mm-scale black chromite crystals visible to the unaided eye (Figure 5). The precise weathering environment of these samples is unclear, but field observations indicate they likely weathered at the surface or in fractures within the shallow subsurface.

The samples are medium- to coarse-grained dunites made up of over 90% olivine, with minor pyroxene and chromite/chrome spinel (Ragan, 1963; Onyeagocha, 1978). The olivine is anhedral, homogeneous in composition, Fo_{90}-$Fo_{91.8}$ (Onyeagocha, 1978), and has a fabric made up of dunite compositional layering, some foliation and lineation of spinel, and later cross-cutting by dunite bands and pyroxene dikes (Toy et al., 2010). The pyroxene is a mix of clinopyroxene and orthopyroxene, and the chromite is euhedral to subhedral (Onyeagocha, 1978). Serpentine is present within fractures and joints that allowed for the introduction of water (Ragan, 1963).

The Twin Sisters dunites originated in the mantle and were emplaced on the continent along thrust faults (Ragan, 1963; Onyeagocha, 1978). Previous studies found it difficult to give the faulting a precise age, but there is agreement that they are no older than late-Cretaceous (87-93 Ma) and no younger than Eocene (45-50 Ma) (Frasse, 1981; Brown, 2012). These rocks weather to a light red-brown color (Ragan, 1963). The Twin Sisters region was covered by the Cordilleran Ice Sheet until ~11 ka and the bedrock was primarily eroded by abrasion under the glacial ice (Francis, 2019). Glacial retreat left behind fresh rock faces that have been exposed to weathering for a geologically short period of time and are in the incipient stage of weathering today. Well-developed clay minerals are therefore not expected in these rocks' weathering rinds.

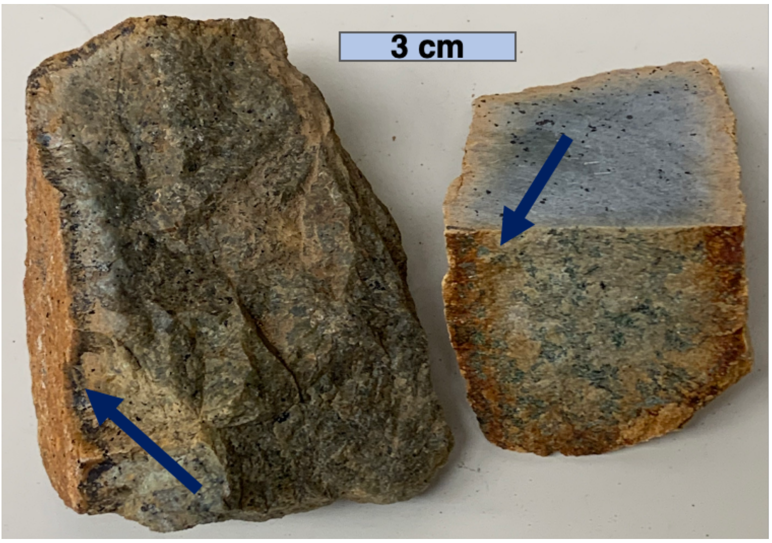

Figure 5: Photo of two Twin Sisters dunite samples. Visible are bright orange weathered surfaces connected to green interiors through weathering rinds (blue arrows).

Columbia River Basalts (CRBs)

Mafic rocks collected in 2018 from Frenchman Coulee and Dry Falls make up the second group of samples. They are from the Roza flow in eastern Washington's Channeled Scablands (Figure 6) (Hoza, 2019). The Roza flow is part of the Wanapum Basalt formation and is approximately 15 Ma (e.g. Thordarson and Self, 1998; Reidel et al., 2002). In the field, samples were selected as a representative suite of weathering patterns in the area (Hoza, 2019); they range from dark brown to reddish to a yellow-green (Figure 7). Dry Falls samples were collected from a weathered roadside cliff face, and the Frenchman Coulee samples were collected as cobbles from a scree slope. Weathering likely occurred at the surface and in near-surface fractures. Minerals present in these samples include plagioclase, pyroxene (augite), ilmenite, apatite, olivine, and an altered mafic phase (Hoza, 2019). There is also a felsic interstitial glass present (Hoza, 2019).

Hoza (2019) describes the weathering rinds as mineralogically similar to the rock interiors, with increases in pore space and fractures. Additionally, Michalski et al. (2006) notes weathered surfaces are spectroscopically brighter and redder than fresh surfaces. The Cordilleran Ice Sheet began to retreat from this area in 15.5 ka (Balbas et al., 2017). Episodic flooding (including the Missoula floods which carved out Dry Falls) continued in this area for approximately 1,000 years (Balbas et al., 2017). This marks a potential 14-15 ka exposure age for the CRB samples.

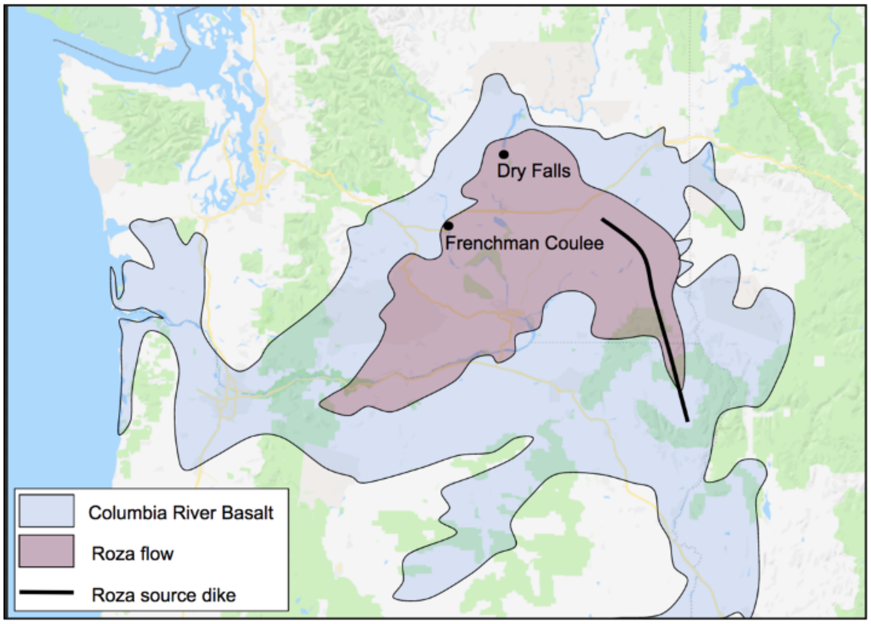

Figure 6: Map of the Columbia River Basalt extent (blue) and the Roza flow in particular (red) with the sample collection sites marked. Credit: Hoza (2019).

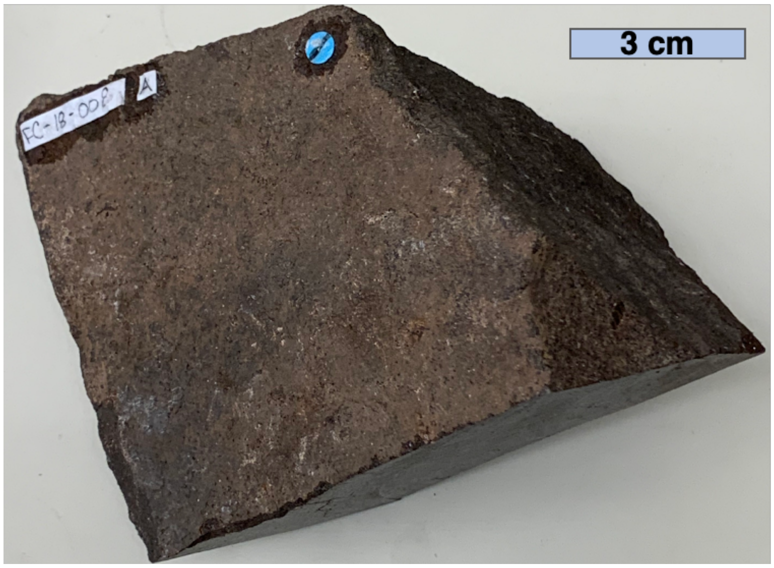

Figure 7: Photo of a Columbia river basalt sample with a dark brown weathered surface.

Mount Baker Andesites

The third group of samples are from Table Mountain, northeast of Mt. Baker in western Washington. They were collected as cobbles (Figure 8) from a scree slope approximately 0.6 km along the Table Mountain trail starting at the Artist Point parking area. Mt. Baker is an andesitic stratovolcano; most of its flows are andesitic, with a few that are more mafic (Moore and DeBari, 2012). The Table Mountain unit is a plagioclase-rich pyroxene-andesite (59%-63% SiO_2) erupted in the mid-Pleistocene (c. 300-310 ka) (Hildreth et al., 2003). Some flows in this unit may contain minor hornblende (Hildreth et al., 2003).

As far as we are aware, no previous studies have investigated altered surfaces of Mt. Baker andesites. Weathering on these samples likely occurred at the surface and in fractures within the rocks; samples with relatively unaltered surfaces and no surface discoloration can be split along fractures to reveal orange to brown discoloration from alteration within the fractures. Francis (2019) used Mt. Baker glacial records as a proxy for the Sisters Glacier, meaning the Table Mountain andesites experienced similar glaciation events and were also covered by the

Cordilleran Ice Sheet where they experienced abrasion under glacial ice until ~11 ka. At present the sample site is buried under snow for much of the year.

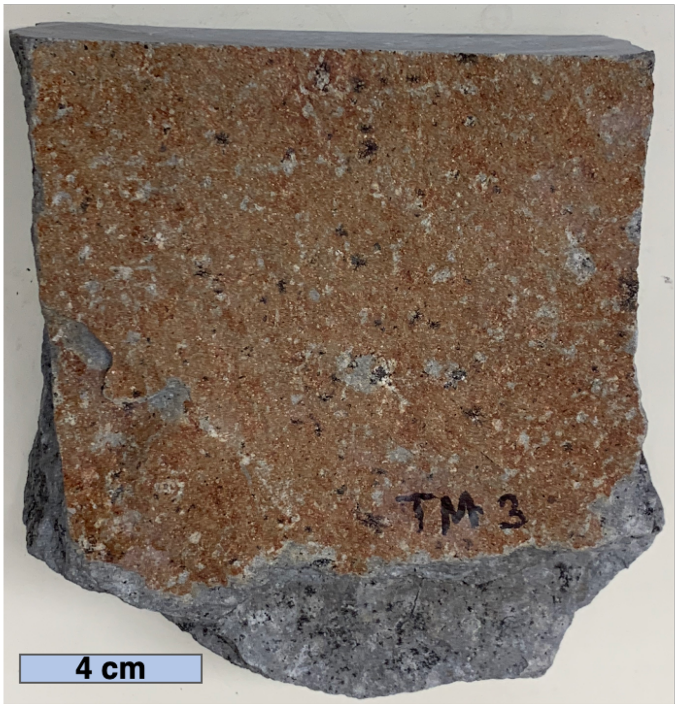

Figure 8: Photo of one Table Mountain andesite sample with a red-orange weathered surface. Relatively unaltered gray areas are also visible on the sides and where the orange material has chipped off.

METHODS

Cutting Slabs

I selected ten dunite, five basalt, and five andesite surfaces to cut into square slabs for in-depth analysis (Figure 9) The slabs are approximately 5 cm by 5 cm across and 1 cm tall. They are larger than the spectrometer's spot size, but small enough to fit in the scanning electron microscope (SEM). I cut one slab of each rock type from sample interiors (as close to the centers as possible) and polished them to 600 grit using silicon carbide powder. This standardized the interior "unweathered" slabs' textures. The samples I selected to cut into smooth slabs have little to no visible weathering on their surfaces.

The rest of the slabs are all natural surfaces with a variety of colors and textures. My initial gauge of weathering was surface redness. The dunite slabs range from green to tan to red and brown, where green samples are generally the least weathered and red samples have the thickest weathering rinds. Although color and rind thickness alone are not good indicators of how much weathering a rock experienced, they are still useful tools for selecting a diverse sample set. For the basalts and andesites I selected rock faces that were distinct from each other. The basalt interiors are black with primarily brown and dark orange-red exteriors. The andesite interiors are light gray with darker gray, orange, and brown exteriors.

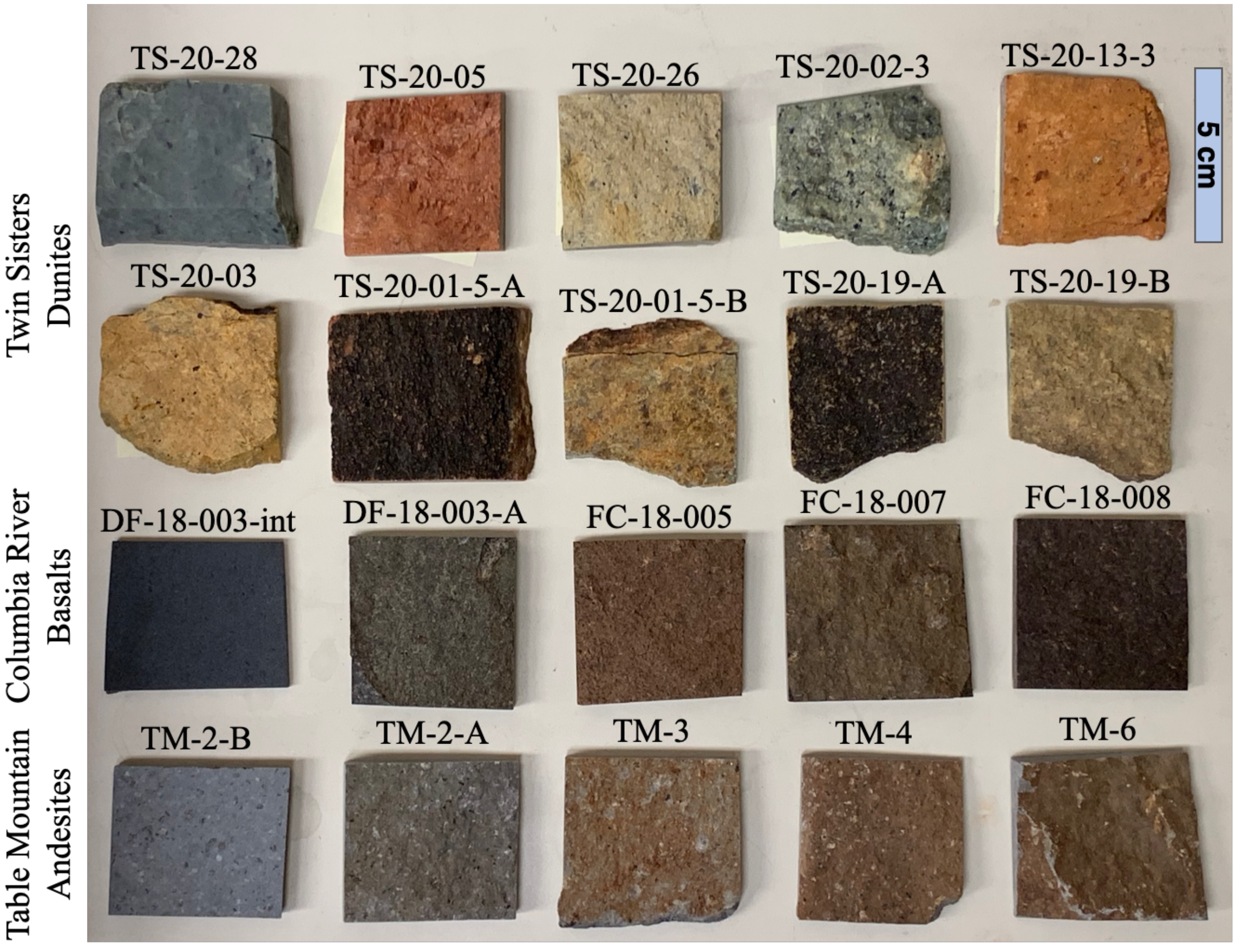

Figure 9: Photo of 20 slabs cut from rock interiors and surfaces of interest.

Spectroscopy

TANAGER

The Western Mars Lab's spectrometer is an Analytical Spectral Devices (ASD) FieldSpec 4 Hi-Res spectrometer with a spectral range of 350 nm to 2500 nm. Using the spectrometer in conjunction with the TANAGER (ThreeAxis N-sAmple Goniometer for Evaluating Reflectance) and its software (Rice et al., 2022b), allows for efficient automatic collection of reflectance spectra at many viewing geometries. The rotating sample stage can accommodate up to five samples along with a white reference. I placed my samples on the stage, leveled them, then moved the surfaces into the spectrometer's focus by raising/lowering the slabs until two laser pointer spots overlapped. Once the samples were set I used the TANAGER's software to start an automatic run collecting spectra across many viewing geometries. For incident and emitted light geometries, I selected angles between -50 and 50 degrees with a 10 degree step size. Azimuth angles ranged from 0 to 150 degrees with a 30 degree step size.

First the goniometer cycled through the samples and white reference in a single geometry while the spectrometer collected spectra from each stage position, then the azimuth moved one step and spectra were collected again. Once all azimuths were covered, the goniometer returned to the starting azimuth and moved the emission angle one step. Once all emission and azimuth angles were covered for the first incidence angle, the incidence arm moved one step and the process repeated. This continued until the spectrometer had completed a measurement for each sample at all incidence, emission, and azimuth angles. Each five sample run took several hours to complete, usually over two days.

TANAGER automatically went through several important steps for spectral data collection and processing. It connected remotely to a separate computer where it applied corrections through the RS^3 and ViewSpec Pro programs. RS^3 optimized the spectra by adjusting the detector's gain to ensure measurements were not saturated. It also performed the white references by taking dark current (records background noise) and white reference measurements, and setting the Spectralon's relative reflectance to 100% reflectance. Spectra from the samples were recorded relative to the Spectralon. ViewSpec Pro processed the data through a splice correction at 1000 and 1800 nm where the three detectors meet and exported the relative reflectance as a CSV for plotting and additional analysis.

Small Diameter Probe

With the spectrometer connected to a Malvern Panalytical Small Diameter Reflectance Probe, I collected spectra along cross sections of 8 samples. They include 4 dunites, 2 basalts, and 2 andesites. The small diameter probe's spot size is approximately 1-mm wide, and the phase angle is nearly zero. The 8 samples are polished slabs cut perpendicular to natural weathering surfaces; several samples show clear weathering rinds in cross section. I collected spectra in transects along these cross sections, pausing to white reference every ten minutes. Figure 10 below shows the cut sample pieces with the spots of interest labeled. The thickest weathering rind on these samples is ~1 cm, while the thinnest is sub-1 mm with no discoloration visible.

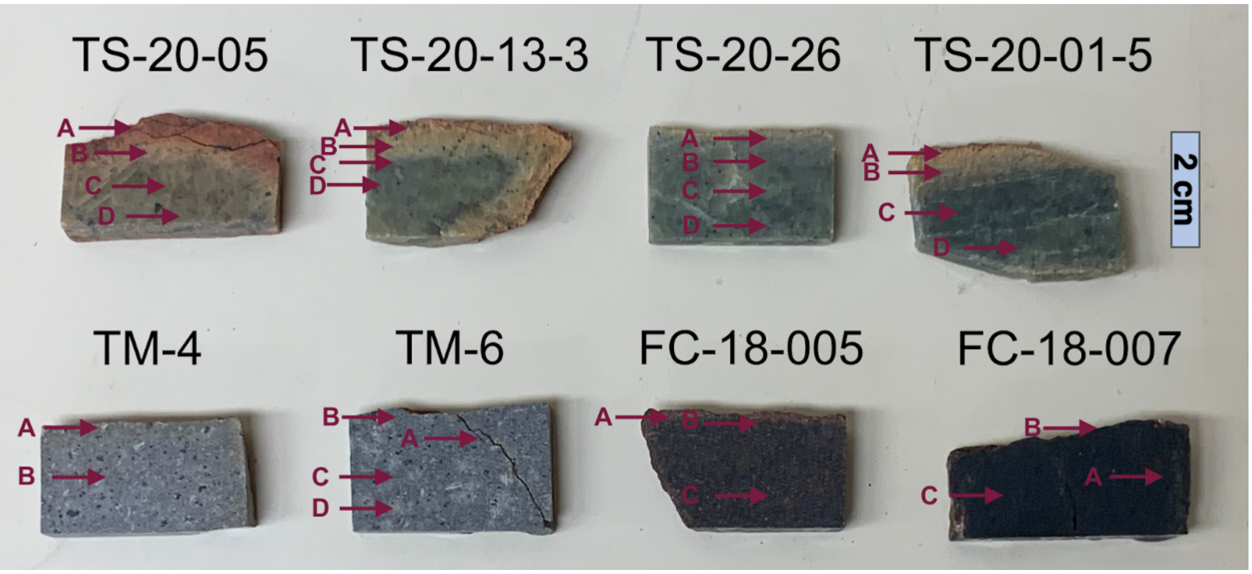

Figure 10: Photo of the 8 cross section pieces, with their spots of interest marked.

Scanning Electron Microscopy (SEM)

I used an SEM Tescan Vega 3 equipped with an Oxford Instruments XMax^N-80 energy-dispersive spectrometer (EDS) to characterize my samples' surface compositions and textures. I analyzed the uncoated slabs in a variable-pressure SEM under a 10 Pa N_2 atmosphere with the beam energy set to 15 keV. The slabs were left uncoated to check for carbon-based features on the surfaces (e.g. lichen). To explore surface textures and assess compositional variability I took backscattered electron (BSE) images of all 20 slabs. Further characterization of surface textures used directional BSE imaging with the detector offset slightly, which created the illusion of a light source to the right of the samples and gave features depth (similar to using the Sun's illumination in orbiter images to identify positive and negative relief features on planetary surfaces). For simplicity I will refer to these as "shadow images" from here on. I collected pairs of BSE shadow images from spots on the sample surfaces that showed representative textures for each sample; the first image in each pair was taken with the sample stage flat, and the second was taken at a 10 degree tilt. I loaded them into the MountainsSEM software and created 3-dimensional models of surfaces through stereoscopic reconstructions of surface topography.

I examined the mineralogical compositions using EDS elemental maps at areas of interest on the slabs. Elemental maps display the qualitative distribution of elements and minerals; EDS point analyses to determine quantitative chemistry could not be performed on the slabs because beam skirting under low vacuum sampled materials outside the selected points of interest.

Thin Sections

I sent 8 samples to Vancouver Petrographics to be made into thin sections: 4 dunites, 2 basalts, and 2 andesites out of the 16 slabbed samples. The selected samples all include naturally weathered surfaces, and some show visible weathering rinds. The thin sections are approximately 30 μm thick (some vary slightly), polished thin sections that were vacuum epoxy impregnated to preserve microtextures within the weathering rinds. All 8 thin sections have at least one edge that is the natural rock surface; several have two weathered edges. A couple thin sections include large fractures containing alteration materials.

Using a petrographic microscope, I noted changes in rock composition and texture from the surfaces inwards. Additionally, I scanned the thin sections using a slide scanner with transmitted light for high-quality reference images. I loaded the scans into the program JMicroVision and used its point counting function to estimate secondary oxide abundances. From 300 randomly selected points in the upper 2-5 mm of each thin section, I classified areas with reddening and amorphous opaque minerals as altered. I rounded them to the nearest whole number and report them here as "% reddening". After collecting the petrographic data, I carbon coated the samples and looked at them under the SEM. The EDS data I collected from these carbon coated thin sections is more precise - with less beam skirting - than when I analyzed the slabs. I made EDS maps and collected data from individual points. SEM data complements the petrographic microscope findings.

X-ray Powder Diffraction (XRD)

I collected XRD data using the Rigaku Miniflex 6G in Western's AMSEC lab. It is a high throughput powder X-ray diffractometer. The samples I selected include 4 dunites, 2 basalts, and 2 andesites with weathered surface material, and one powdered interior of each rock type. The powdered interior samples were from the same rocks I used to cut interior slabs for spectral and SEM analysis. Most weathered surfaces were from the samples I selected for thin sections.

Powdering Interiors and Removing Rinds

For the 3 interior samples, I crushed a small chunk of each with a rock hammer, then powdered the chips with a Spex Mixer Mill for 6 minutes. The end result was a fine powder suitable for XRD analysis. For weathered surfaces, I used a percussive hammer to carefully remove the outer layer of weathered material from the samples. Weathered material on the surfaces came off with more easily than relatively unaltered material further from the surface. The material that came off these samples is a mix of grain sizes, with some grains up to sand size. Ideally, XRD samples are powdered finer than this, but with time constraints they worked well enough for the few initial runs before clay separation.

Clay Separation

To isolate any secondary minerals - specifically clays - in these samples, I separated out the clay-sized fraction from the rinds and interiors. I began by separating out material <2 μm in diameter via standard sedimentation (Poppe et al., 2001). An initial XRD look at the <2-μm fraction showed compositions nearly identical to the bulk sample. To separate out the <0.2 μm material from the clay-sized fraction I used a centrifuge with run times and speeds calculated based on the methods outlined in Poppe et al. (1988) and Jackson (2005). Running Western's centrifuge at 2400 rpm for 35 minutes and 20 seconds removed approximately all material >0.2 μm in diameter from the supernatant liquid. Running the supernatant again at 8700 rpm for 30 minutes settled the <0.2-μm sample from the water. I pipetted a slurry of <2-μm material onto zero-background sample holders and allowed them to airdry to create oriented clat mounts for XRD analysis.

Instrument Parameters

I ran the Rigaku in XRF reduction mode using the parameters listed in Table 1 below. listed in Table 1. For large sample volumes I used standard zero-background sample holders provided by AMSEC, and for <0.2-μm samples with very small volumes I used Rigaku zero-background flush-mounts. The first row has the parameters I used for samples pre-separation. The second and third rows are parameters for the <0.2-μm fractions. Most notably I slowed down the scan speed to account for lower counts due to smaller sample volumes. The third set of parameters covers a shorter range of angles to focus on any potential clay peaks.

Table 1: XRD Parameters

	Range (degrees)	**Step Width (degrees)**	**Scan Speed (degree/min)**
Initial runs	3-90	0.04	10
Post-separation	3-90	0.04	5
Clay range re-runs	3-35	0.04	0.4

Plotting Mars Data

Mastcam-Z's multispectral surface observations are calibrated to I/F through near-simultaneous observations of calibration targets mounted on the rover (Hayes et al., 2021) and pre-flight calibration coefficients (Kinch et al., 2020). Reflectance factor (R*, the y-axis on Figures 51 and 53) is calculated by dividing I/F by the cosine of each observation's solar incidence angle. New observations are run through asdf to create an array of rapid look multispectral products, including natural and enhanced color images, decorrelation stretches, and maps of other spectral parameters that highlight variations in rock and soil composition (Million et al., 2022; St. Clair et al., 2022). Regions of interest (ROIs) are selected in each observation and extracted to create a set of R* spectra representative of the observation.

For this study, I selected ROIs from three observations of olivine-rich rocks in the Séítah formation because they are spectroscopically similar to my weathered terrestrial dunites, along with one ROI of a rock coating to highlight compositional variability. The Sampling and Caching Subsystem on Perseverance's arm includes a Coring Drill, Abrading Bit, and Gas Dust Removal Tool; they work together to create 5-cm wide, 2-mm deep, dust free abrasion patches where rover instruments can study relatively fresh rock surfaces (Moeller et al., 2020). I chose my olivine-like ROIs from three such abrasion patches named Garde, Dourbes, and Pont du Loup.

To compare my lab spectra to my selected ROIs, I started by convolving the hyperspectral lab data to Mastcam-Z's wavelengths. I ran a python script that automatically re-binned the data and exported a CSV file with reflectance at each of Mastcam-Z's wavelengths (Hoza, 2019). Then, I plotted my data alongside Mastcam-Z spectra using asdf's pretty-plot (Million et al., 2022; St. Clair et al., 2022).

RESULTS

Composition and Texture

Dunites

The dunite samples are primarily composed of olivine, specifically forsterite (Figure 11). Pyroxene, chromite, and serpentine are also present in the samples (Figure 12). See Table 2 for a detailed list of surface compositions and textures. Serpentine and small amounts of Fe-oxides fill interior fractures, but most of the Fe-oxides are found on natural rock surfaces or in near-surface fractures (Figures 13 and 15).

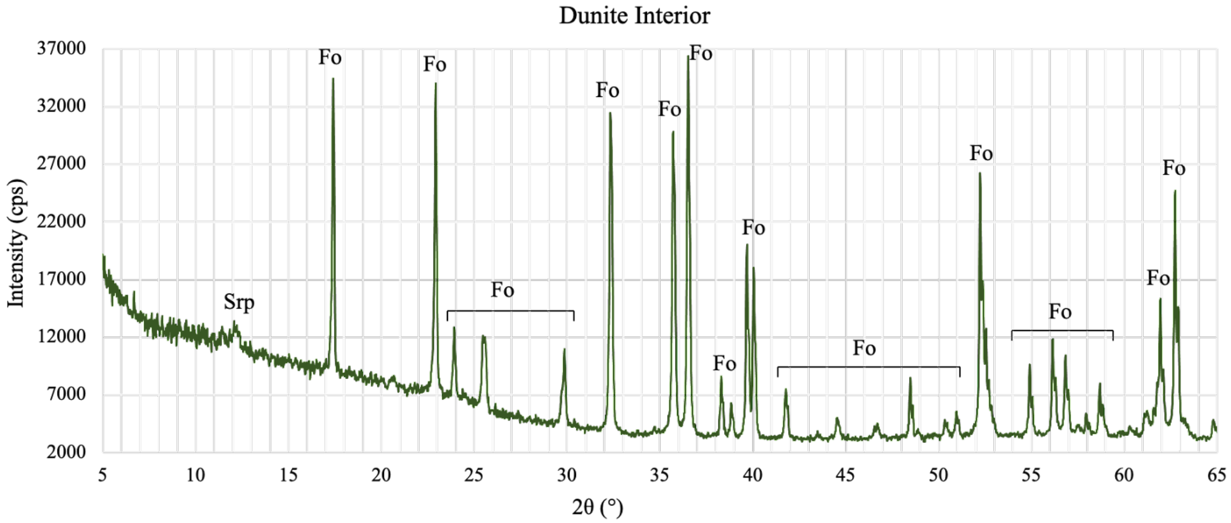

Figure 11: XRD data from TS-20-28 (bulk interior). The composition is primarily forsterite, with a small serpentine peak at 12 degrees.

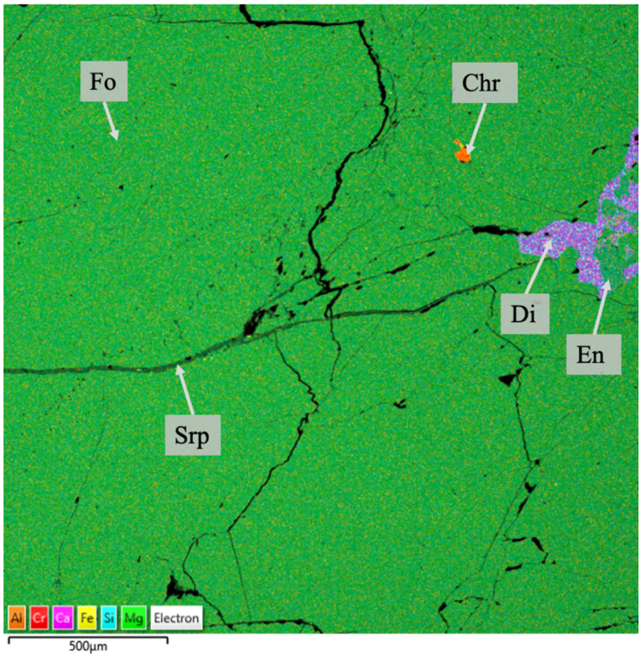

Figure 12: EDS element map of TS-20-26’s thin section interior. Green is olivine (mostly, small amounts are enstatite), purple is diopside, and orange is chromite. Large fractures are filled with dark green serpentine.

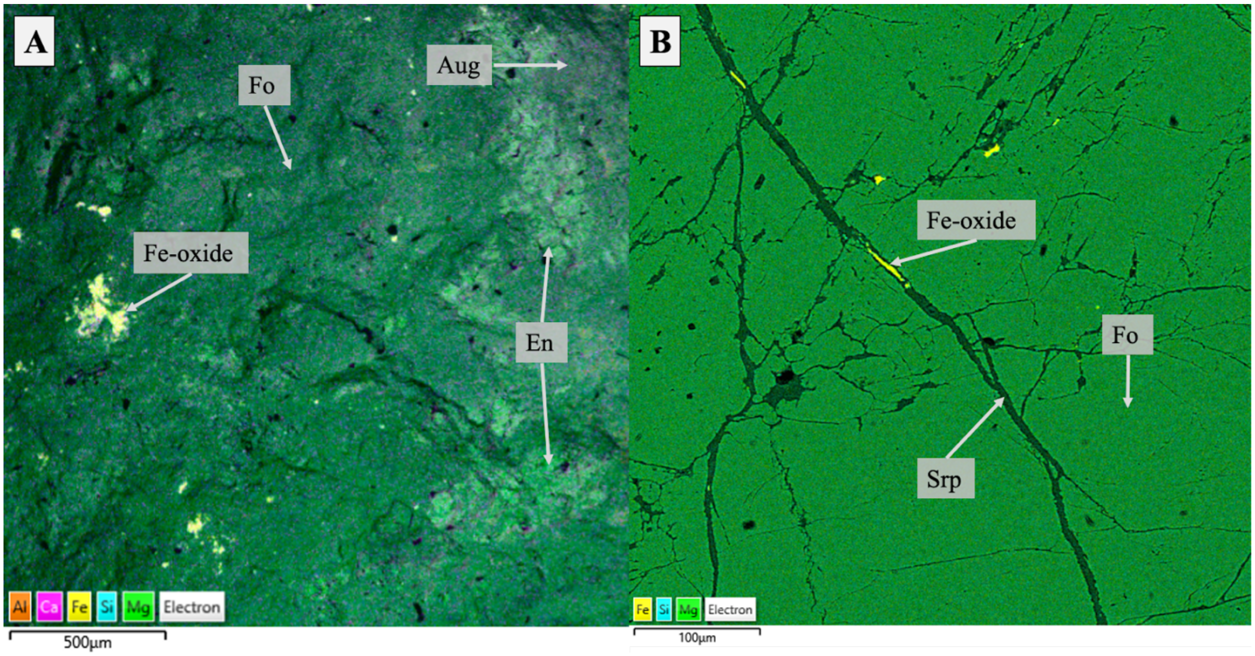

Figure 13: (A) EDS element map of TS-20-02-3’s surface. (B) EDS element map of TS-20-26’s thin section. Most of the image is olivine, dark green is serpentine, and yellow spots are Fe-oxides. Olivine makes up most of the minerals present, pale green is a Ca-poor pyroxene, and yellow spots are Fe-oxides. Al is present as substitutions in the pyroxene formula.

XRD patterns from the <0.2-µm size fraction of the weathering rinds show more forsterite and serpentine peaks, along with a small smectite peak at ~6.1 degrees in one sample (Figure 14). The wide peak at ~9.5 degrees appears in the data from every sample run on one specific sample mount and is assumed to be an artifact related to the mount.

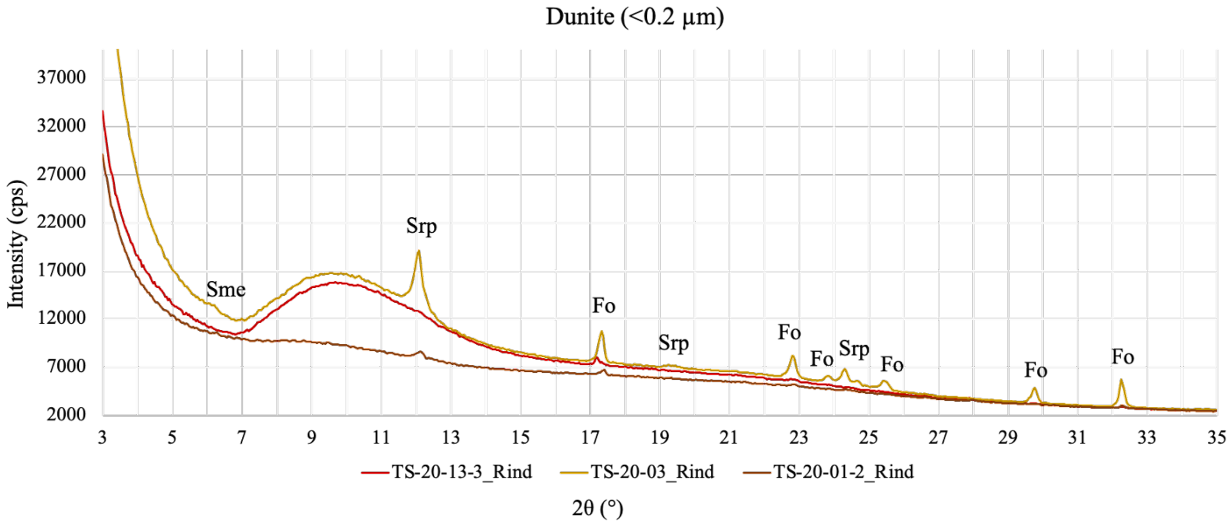

Figure 14: XRD patterns from the <0.2-µm size-fraction of three dunite weathering rinds. Forsterite and serpentine peaks are the most prominent. There is a peak at ~6.1 degrees that could be smectite or another phyllosilicate. The wide amorphous peak at ~9.5 degrees is an artifact likely related to the sample mount.

The red samples have the most Fe-oxides on their surfaces, followed by the brown and tan samples, while the green samples have the least. (Sample color groupings are listed in Table 2.) Fe-oxides can be found on sample surfaces and in near-surface fractures (Figure 15). They appear as discontinuous <5-µm thick coatings on the red dunites surfaces (Figure 15) and fine-grained clusters on the other natural surfaces (Figures 13 and 16). The distribution and size of areas covered by <5-µm thick Fe-oxide coatings is similar to the distribution and sizes of small dark red spots on TS-20-05 and TS-20-13-3 (Figure 9).

Carbon and fine-grained material are most abundant on dark brown samples (Figure 16). The fine-grained material includes orthoclase, plagioclase, pyroxenes, olivine, and titanomagnetite (Figure 17). The tan samples also have the occasional feldspar or titanomagnetite crystal that clearly does not match the rock’s primary mineralogy and is caught in a depression on the surface (Figure 20).

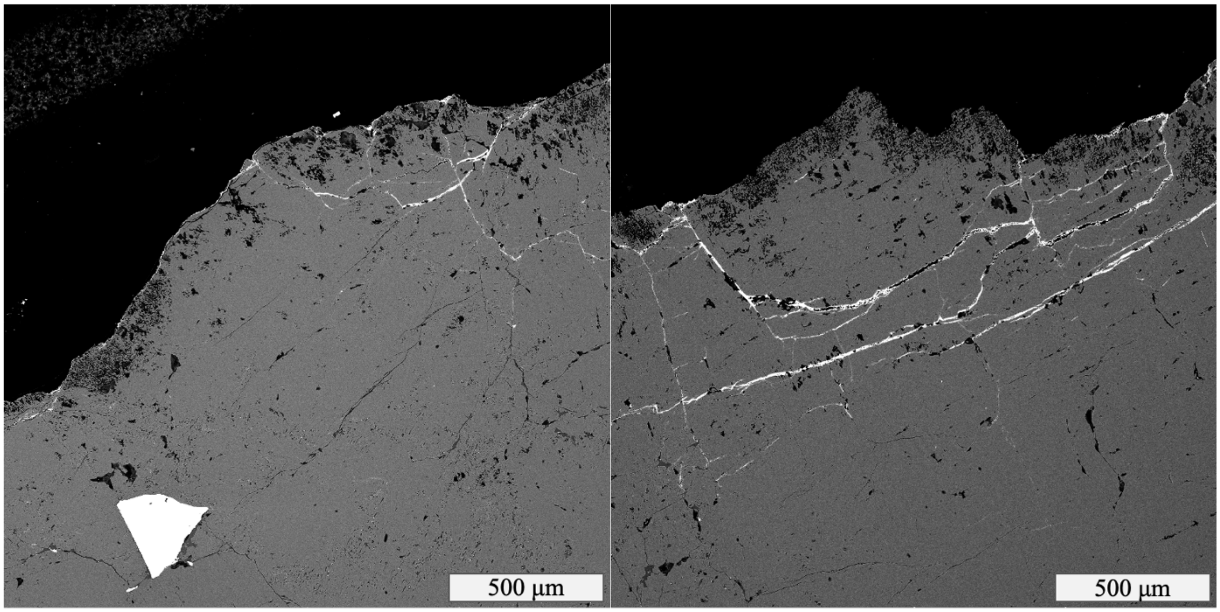

Figure 15: Two SEM backscatter images of TS-20-13-3’s thin section at the sample surface. The bright white euhedral mineral in the left image is chromite. The bright white material lining the surface in places and filling fractures is an Fe-oxide.

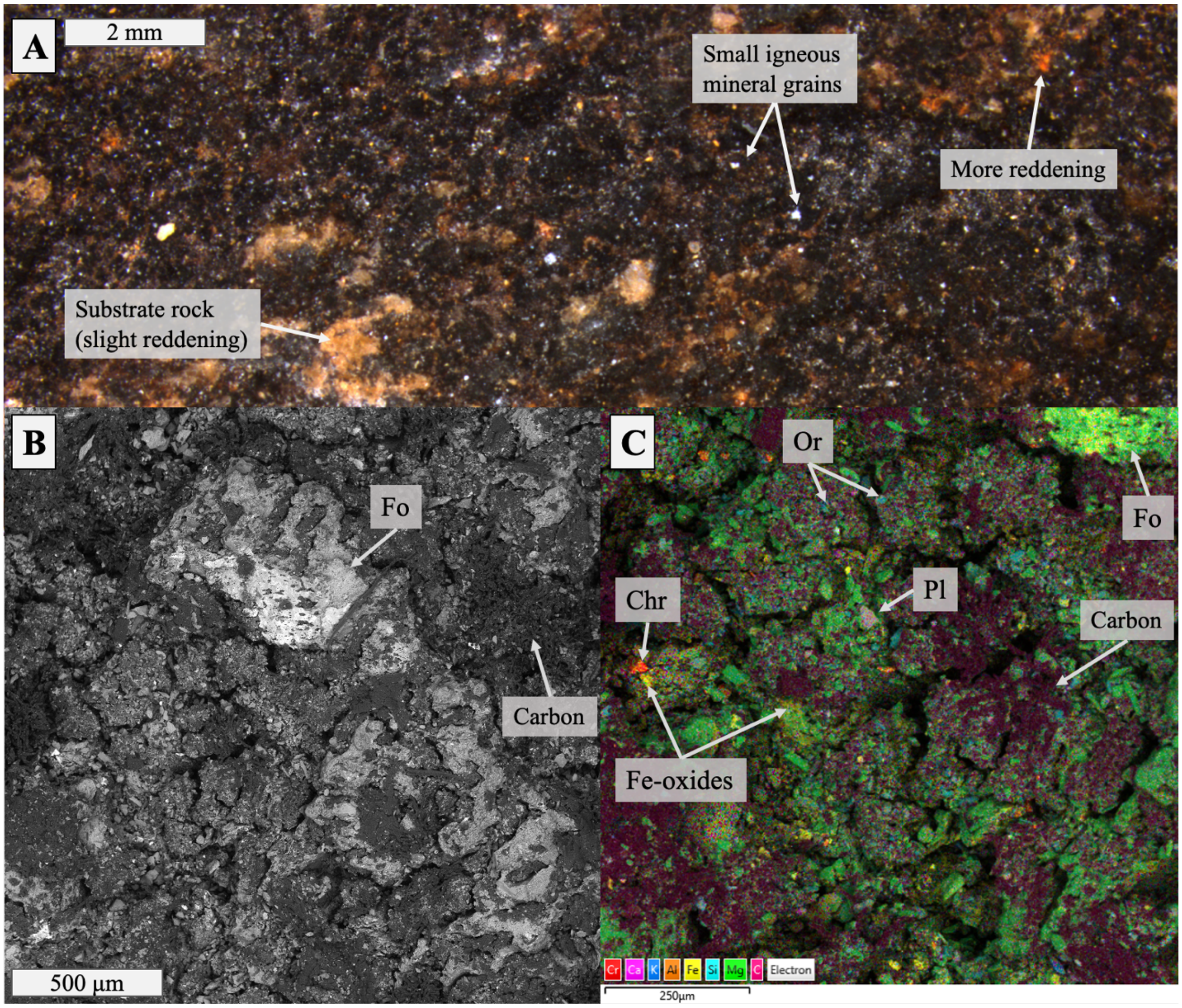

Figure 16: (A) Low magnification image of TS-20-01-5-A. (B) Backscatter image showing the fine-grained texture common to TS-20-01-5-A's surface. (C) EDS element map at a slightly higher magnification to highlight the compositional variability and abundance of carbon on TS-20-01-5-A's surface.

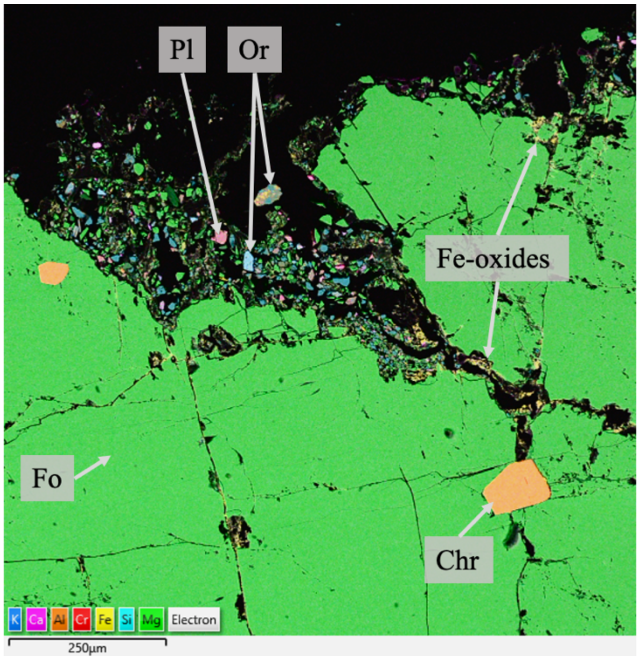

Figure 17: EDS element map of the TS-20-01-5-A thin section Showing the compositional variability of the fine-grained material covering the surface. Here it is collecting in the mouth of a fracture.

The green samples with natural surfaces are relatively smooth when compared to other dunite slabs. Fracturing is minimal, there are few holes or pits, and changes in topography are accompanied by gentle slopes rather than steep cliffs (Figure 18). Thin sections show fractures extend completely through the samples, but there is little change in the pattern of fracturing related to distance from the surface of relatively unweathered samples (Figure 19). There is little to no near-surface reddening or formation of opaque oxides in these fractures.

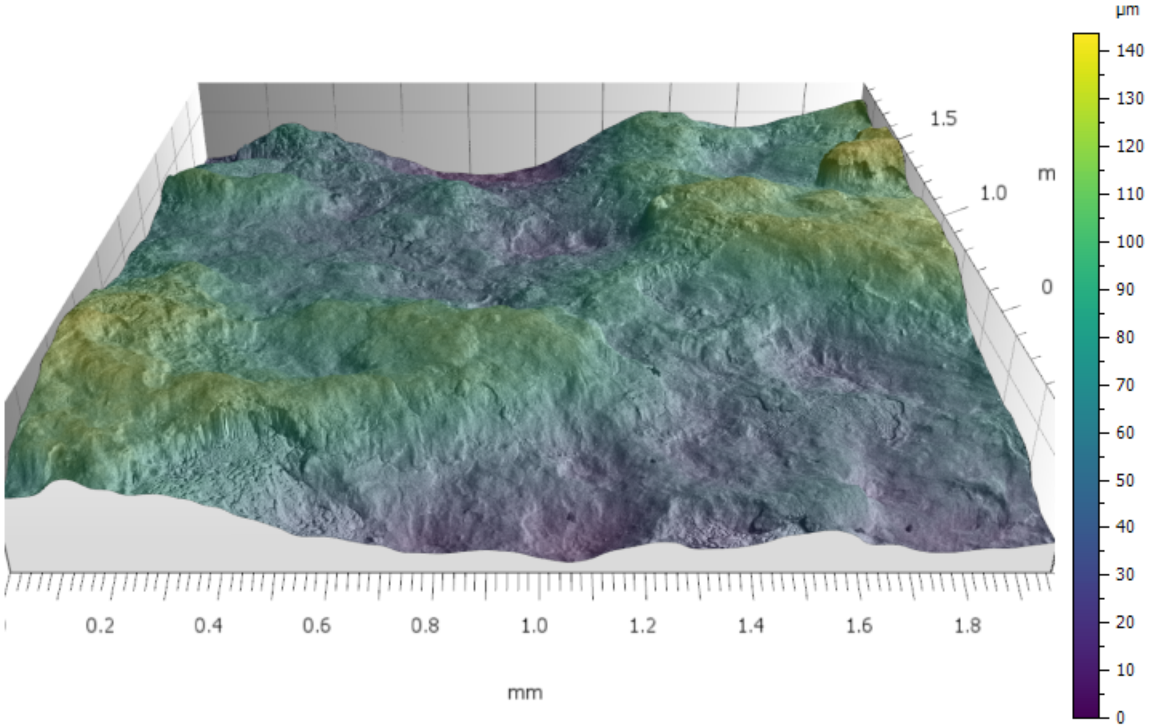

Figure 18: 3D surface topography map of TS-20-02-3. The area shown is 4 mm^2 and has a range in surface elevation of 150 µm. The z-axis is amplified 15%.

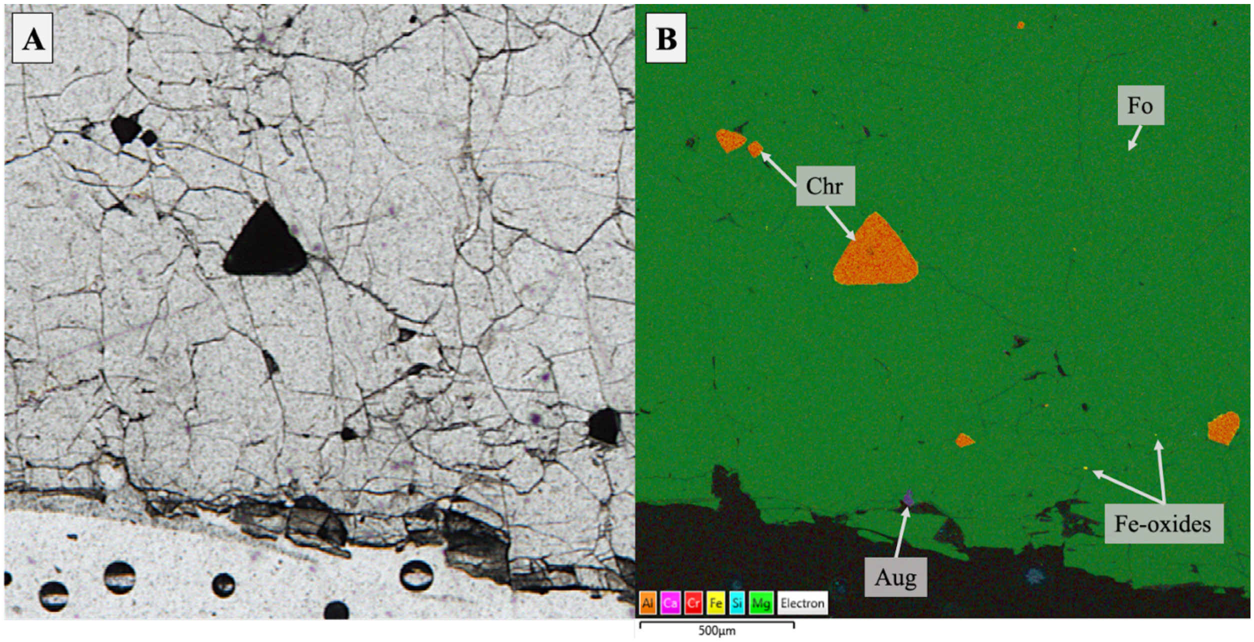

Figure 19: (A) TS-20-01-5 thin section scan, transmitted light (no polarization). The bottom edge of the sample is TS-20-01-5-B's weathered surface. Fractures extend through the whole sample and do not change in pattern or frequency between the interior and exterior. There is a slight change in color for olivine grains at the very edge of the sample, but any compositional changes are not enough to appear in (B) an EDS element map of the same location on the thin section.

Surface textures among the tan samples are a mix of smooth areas with large primary minerals, and blocky angular areas that can include fine-grained material made up of broken up pieces of the primary minerals and the occasional feldspar (Figure 20). Small pits and fractures are common. Fe-oxides appear as very small individual grains occasionally across the surfaces. En echelon etch pits can be seen on forsterite grains (Figure 21). Velbel (2009) describes the formation of these types of etch pits, and finds they are most often empty of secondary minerals in the early stages of weathering. They appear to be empty here as well.

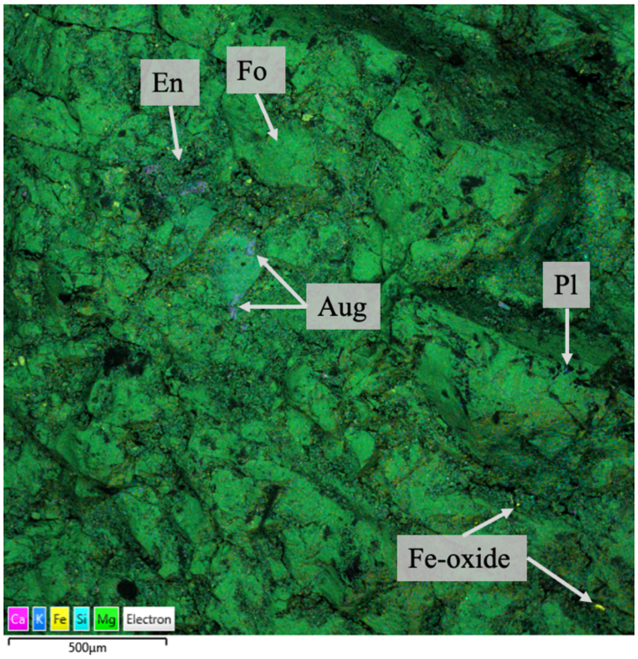

Figure 20: EDS element map of TS-20-19-B’s surface. Black spots with fuzzy edges are carbon stuck to the surface.

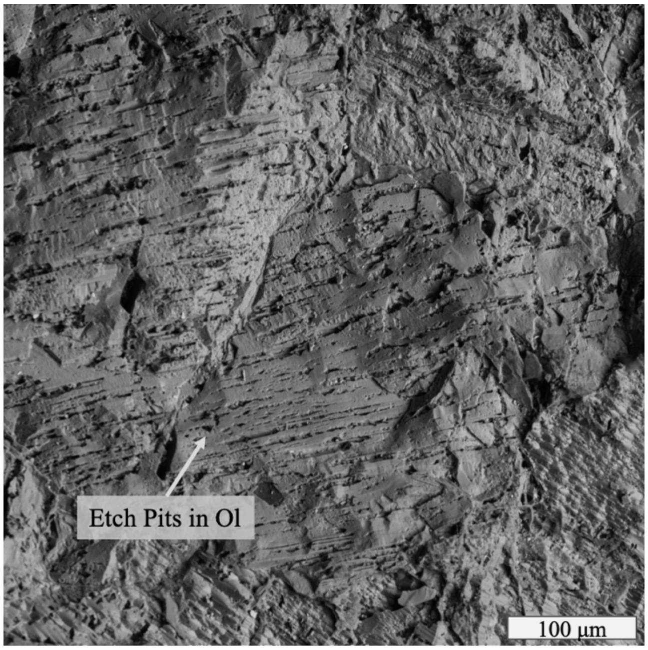

Figure 21: SEM backscatter image of TS-20-26 with BSE detector offset from center to create depth by simulating a light source to the right/east of the image. En echelon etch pits cut across olivine grains.

Red samples are even more broken up than the tan group. Large primary minerals are surrounded by fine-grained material that collects in areas of low topography. Deep pits and trenches are present (Figure 22) and fracturing is widespread. Fractures widen and become more common near the surface (Figure 23). Reddening and alteration of primary minerals to form opaque oxides occurs at the surface, in near-surface fractures, and along mineral grains (Figure 23). Porosity increases and grain size decreases towards the surface as well. Porosity changes the most in the upper 5 mm of the weathering rind (Figure 23).

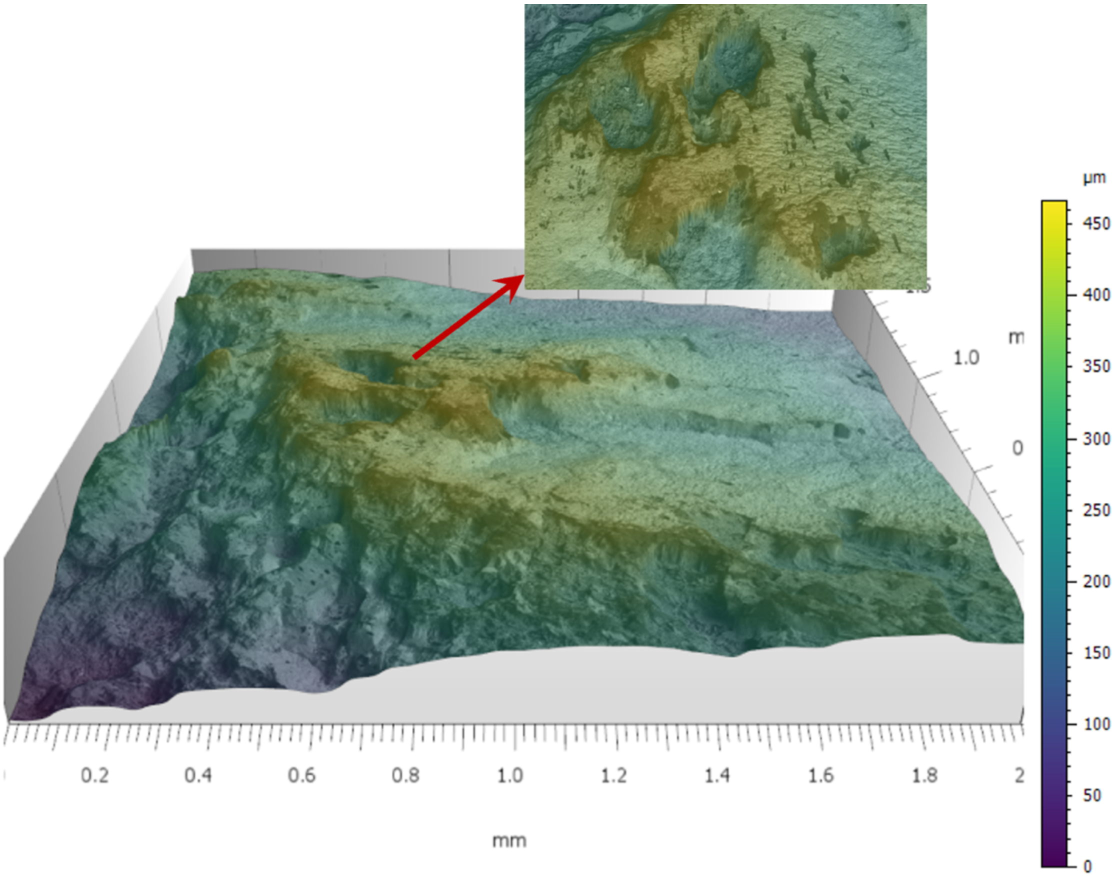

Figure 22: 3D surface topography map of TS-20-05. The area shown is 4 mm^2 and has a range in surface elevation of 460 µm. The z-axis is amplified 15%. The inset image is another angle of large pits on the surface.

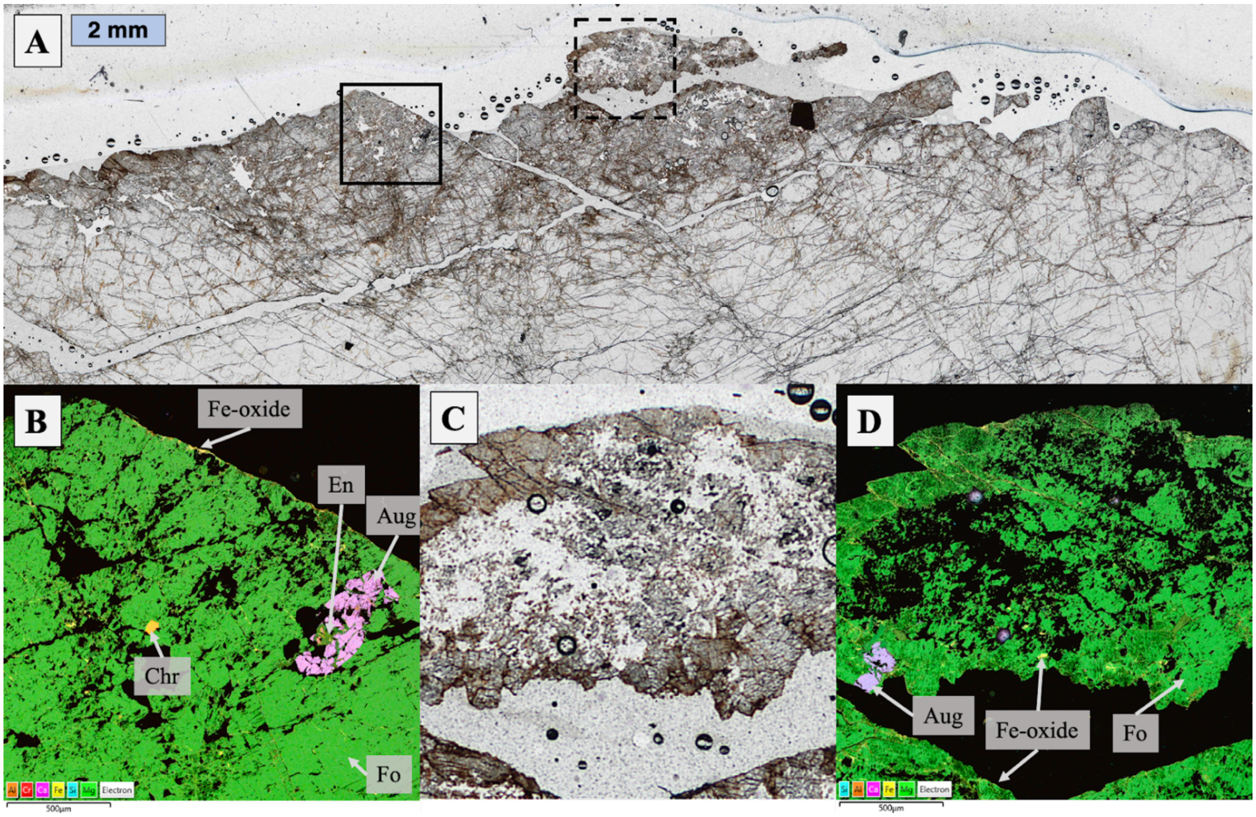

Figure 23: (A)TS-20-05 thin section scan; transmitted light (no polarization). The upper half of this thin section is thinner than the standard 30 µm thick, making some oxides appear red to brown, instead of opaque. Grain size is smaller near the surface and porosity increases. (B) EDS map of the area outlined by the square with solid lines. (C) Zoomed in view of the area outlined by the square with dashed lines. (D) EDS map of the same area as C.

The brown dunites have rough surfaces with relatively large fractures (Figures 16 and 24). The fine-grain material can be seen in thin section within the mouths of large fractures and in pits at the surface (Figure 24). Smooth primary mineral grains appear on occasion but are often partially to mostly covered by carbon (Figure 16). Carbon is abundant across the surfaces and can take the form of radial fibers (Figure 16) or near-circular nodules (Figure 25) in addition to fine-grained amorphous masses.

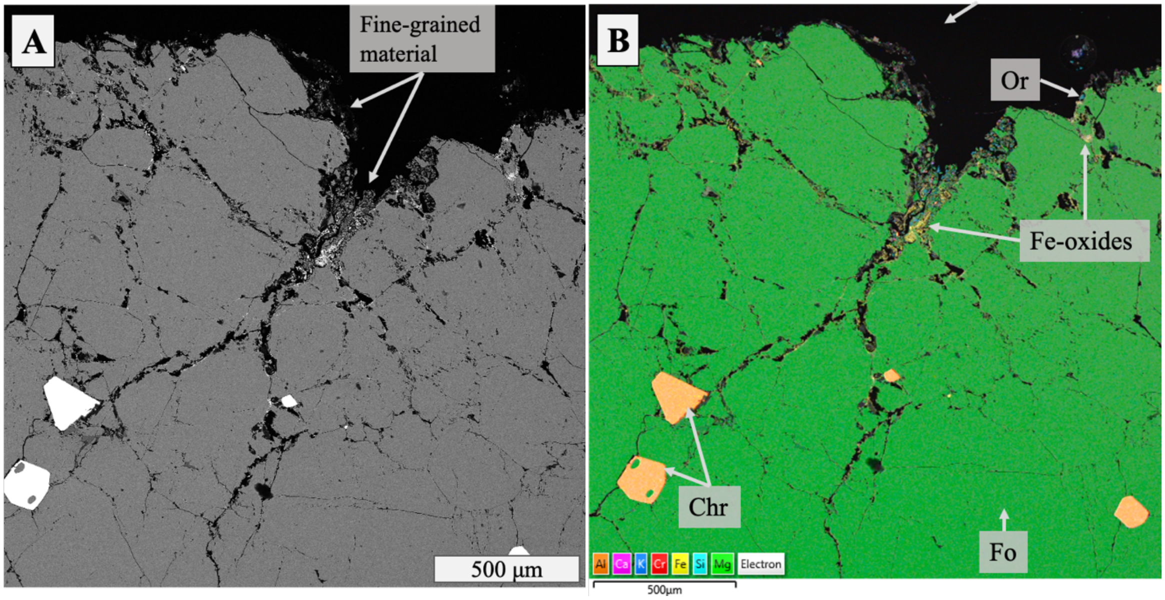

Figure 24: (A) Backscatter image of a fracture in TS-20-01-5's thin section. Fine-grained alteration products can be seen in the fracture and along the sample surface. (B) An EDS element map of the same spot with mineralogy labeled.

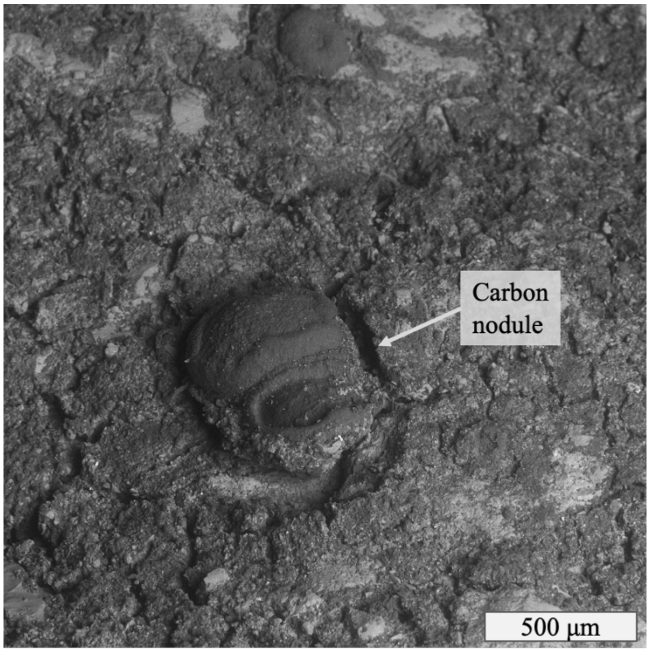

Figure 25: SEM backscatter "shadow mode" image of a carbon nodule on TS-20-19-A. The carbon nodules are more common on TS-20-19-A than TS-20-01-5-A.

Table 2: Summary of the Twin Sisters dunite samples' surface composition and textures. Groupings are primarily based on surface texture.

Sample Name	**Group**	**Surface Composition**	**Texture**	**Thin Section Observations**
TS-20-28	Green	Primarily Fo. Minor Aug, En, Chr, and Srp. Very few Fe-oxides in fractures	Cut slab; polished to 600 grit	n/a
TS-20-02-3	Green	Primarily Fo. Minor Aug, En, Chr, and Srp. Fe-oxides form occasional amorphous blobs	Relatively smooth and intact surface, few fractures	n/a
TS-20-01-5-B	Green	Primarily Fo. Minor Aug, En, Chr, and Srp. Fe-oxide coatings starting to form	Smoothest natural surface, few fractures	2% reddening in upper 5 mm
TS-20-19-B	Tan	Primarily Fo. Minor Aug, En, Chr, and Srp Occasional fine-grained Or, Pl and Fe-oxides	Mix of smooth and blocky textures, fine-grained material common	n/a
TS-20-26	Tan	Primarily Fo. Minor En, Aug, Chr, and Srp. Occasional Fe-oxides. Highest En to Aug ratio of the dunites.	Mix of smooth and blocky textures, fine-grained material and small fractures are common, olivine grains have many etch pits	10% reddening in upper 5 mm
TS-20-03	Tan	Primarily Fo. Minor Aug, En, Chr, and Srp. Fe-oxide coatings are common	Mix of smooth and blocky textures, fine-grained material and small fractures are common	n/a
TS-20-13-3	Red	Primarily Fo. Minor Aug, En, Chr, and Srp. Fe-oxide coatings are widespread.	Most surfaces are rough and angular, large pits and trenches are common, high porosity. Fe-oxides form thin, discontinuous coatings	28% reddening in upper 5 mm

TS-20-05	Red	Primarily Fo. Minor Aug, En, Chr, and Srp. Fe-oxide coatings are widespread.	Most surfaces are rough and angular, large pits and trenches are common, highest porosity of all dunites. Fe-oxides form thin, discontinuous coatings	27% reddening in upper 5 mm
TS-20-19-A	Brown	Primarily Fo and carbon. Minor Aug, En, Chr, Srp, and Fe-oxides. Fine-grained material includes abundant Or and Pl, with occasional titanomagnetite	Rough surfaces with deep fractures filled with fine-grained material, widespread fracturing, carbon nodules abundant	n/a
TS-20-01-5-A	Brown	Primarily Fo and carbon. Minor Aug, En, Chr, Srp, and Fe-oxides. Fine-grained material includes abundant Or and Pl, with occasional titanomagnetite.	Rough surfaces with deep fractures filled with fine-grained material, widespread fracturing	13% reddening in upper 5 mm

Basalts

The DF-18-003 interior composition includes plagioclase, augite, ilmenite, apatite, a felsic interstitial glass, and an altered mafic phase (Hoza, 2019). See Table 3 for sample specific composition and texture notes. Hoza (2019) notes changes in the chemistry of DF-18-003's mafic phase with distance from the weathering rind; the Fe content is lower near the surface than the interior. Additionally, DF-18-003's rind has a 2:1 swelling clay with an XRD peak at d=14.5 angstroms, making it a smectite or vermiculite clay (Hoza, 2019). XRD data from Frenchman Coulee weathering rinds show very similar compositions to the Dry Falls analysis by Hoza. However, XRD data from the <0.2-µm size-fraction for the Frenchman Coulee weathering rinds do not have a clay peak at ~6 degrees like the Dry Falls samples (Figure 26). Thin sections further confirm a similar mineralogy between the two groups of basalts (Figure 27). All are porphyritic, with plagioclase making up nearly all the largest phenocrysts.

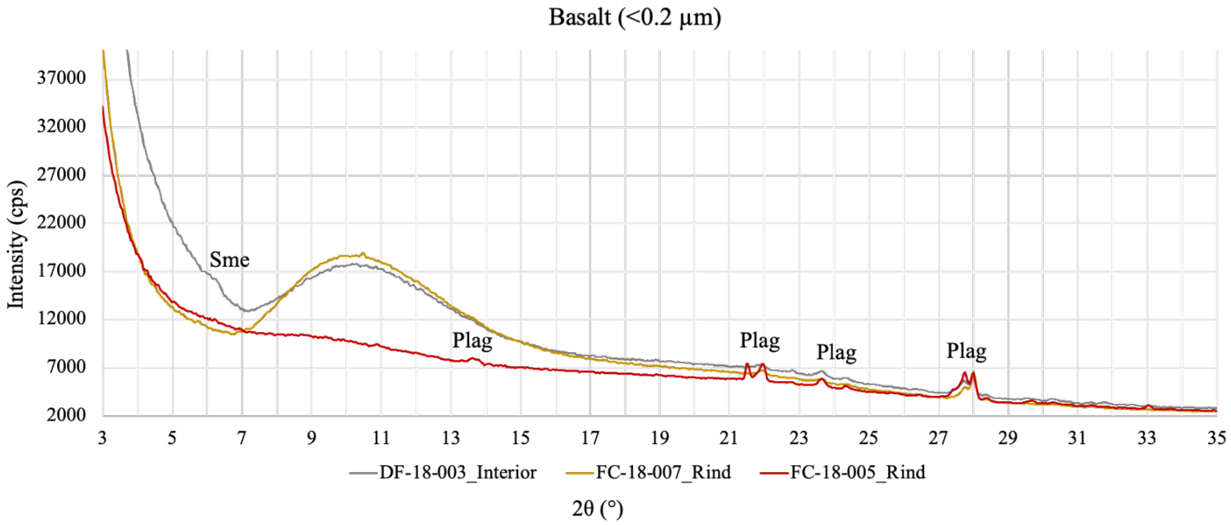

Figure 26: XRD patterns from the <0.2-µm size-fraction of three basalt samples: one interior and two weathering rinds. All have plagioclase peaks. A small peak at ~6.1 degrees could be smectite or another phyllosilicate. The wide amorphous peak at ~10 degrees is an artifact likely related to the sample mount.

Chemical alteration is visible in thin sections (reddening and the formation of opaque oxides) and is most obvious within 2 mm of sample surfaces and near large fractures (Figure 27). Glass and the altered mafic phase show the most reddening and darkening (Figure 27). Pyroxene and olivine show some reddening and plagioclase shows very little. Alteration is present throughout the samples; thin fractures through plagioclase phenocrysts filled with red material and the altered mafic phase's presence far from sample surfaces indicate this alteration is not related to the surface weathering. Additional reddening at sample surfaces visually marks mm scale weathering rinds where chemical and textural changes related to weathering primarily occur. The reddening indicates a chemical change is occurring, even though it is subtle enough to not appear in the Figure 27 EDS map.

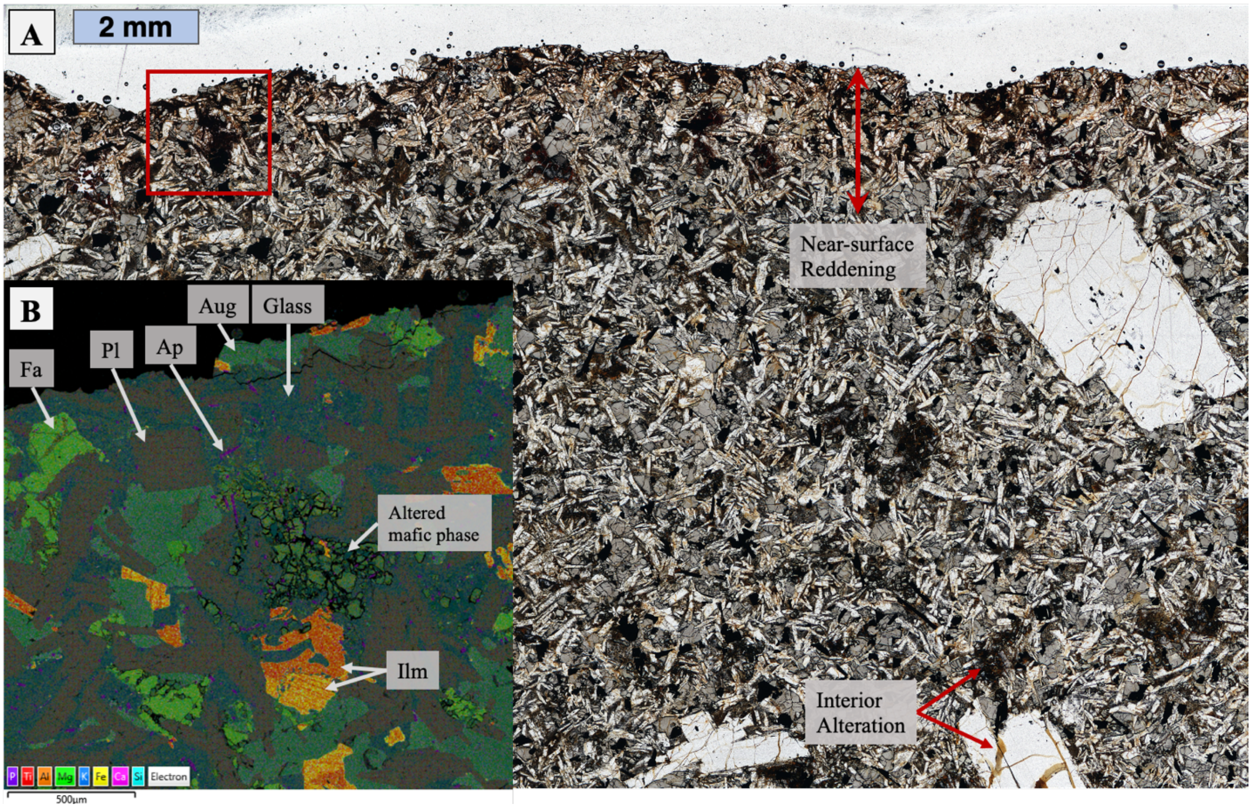

Figure 27: (A) Scan of FC-18-005's thin section (transmitted light, no polarization). The altered mafic phase and small fractures with red material are present throughout the sample. Reddening increases overall in the 2 mm closest to the surface. (B) An EDS element map of the area outlined by a red square. Microfracturing increases within ~200 µm of the surface.

DF-18-003's surface texture is rough with lots of pits and fractures (Figure 28). Subhedral plagioclase grains cross over pits where material more susceptible to weathering has been removed (Figure 28). Large plagioclase phenocrysts (up to 2 mm long) create smooth areas on the sample surface. Fine-grained material is common and tends to collect in pits and fractures. Porosity and fracturing increases towards the surface (Figure 29).

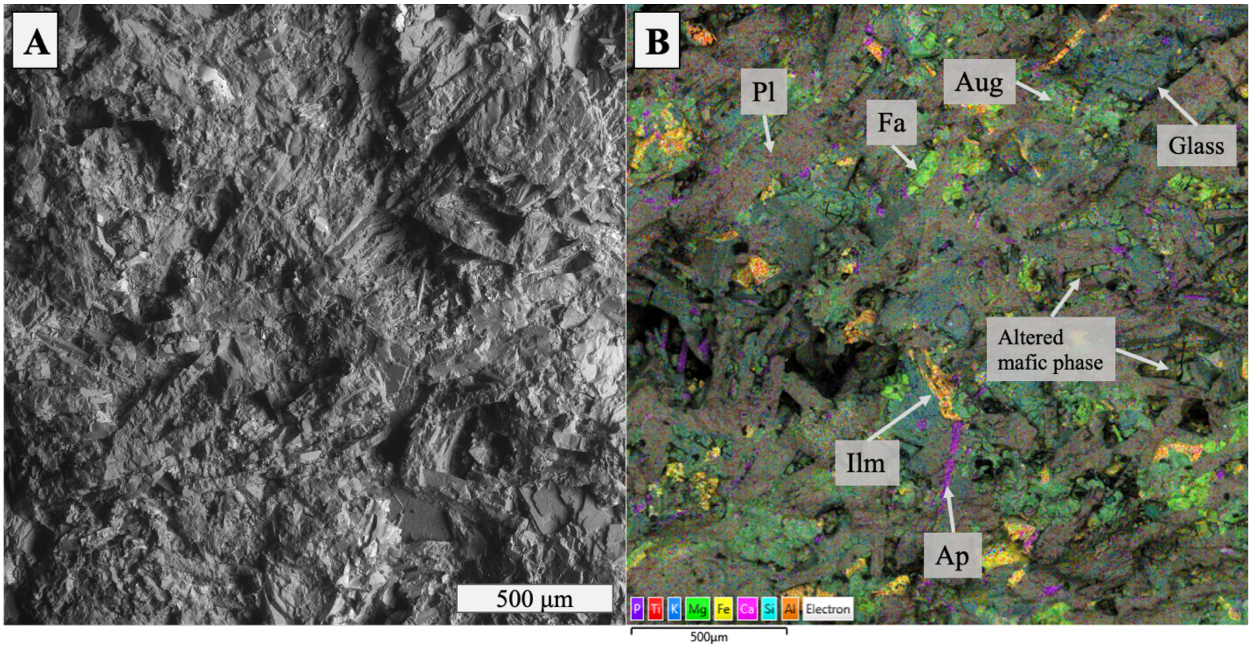

Figure 28: (A) SEM backscatter "shadow" image of DF-18-003-A showing the texture. The surface is rough where the altered mafic phase and glass has been removed, leaving behind rough edges of subhedral plagioclase. (B) An EDS element map of another spot on the same sample highlights how composition relates to texture.

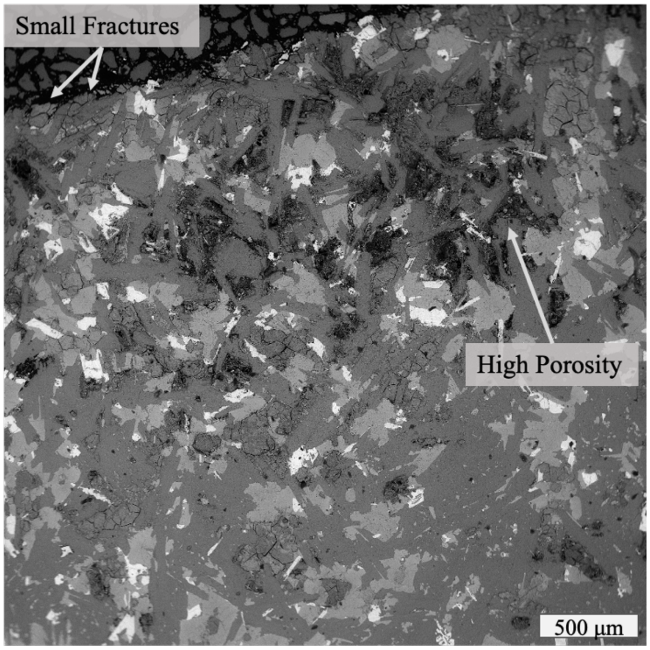

Figure 29: New SEM BSE image of DF-18-003's thin section from Hoza (2019). Porosity increases in the upper 2 mm of the sample by removing the altered mafic phase and glass. Fracturing increases in the upper ~200 µm.

Surfaces on the Frenchman Coulee samples have a mix of smooth and rough areas. Large plagioclase phenocrysts create smooth areas on the surface, like in the Dry Falls group (Figure 30). Pits and fractures are common, but smaller than those on DF-18-003 (Figure 30). Fracturing increases towards the surface (Figure 32), but at this scale porosity does not change to the same extent as the Dry Falls sample (Figure 29). The altered mafic phase is more porous than the surrounding minerals, but its porosity is consistent through the samples.

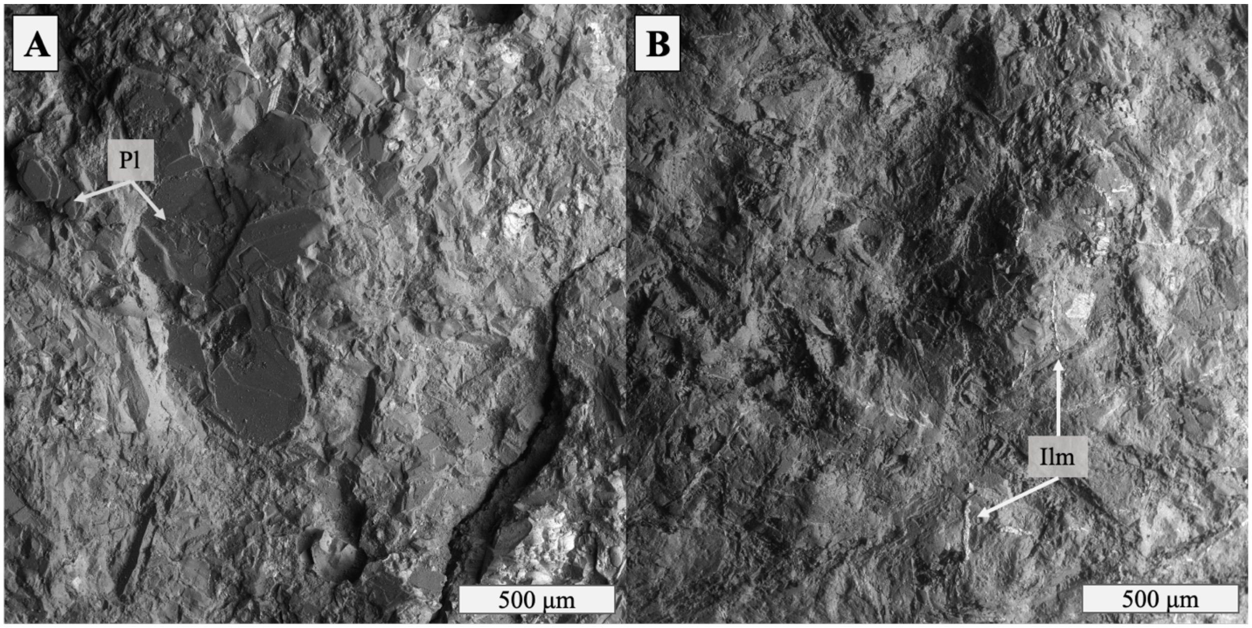

Figure 30: (A) SEM backscatter "shadow" image of FC-18-008. Large plagioclase phenocrysts create smooth areas on the surface. (B) SEM backscatter "shadow" image of FC-18-007. Elongated, high relief minerals are ilmenite; they are most abundant in this sample.

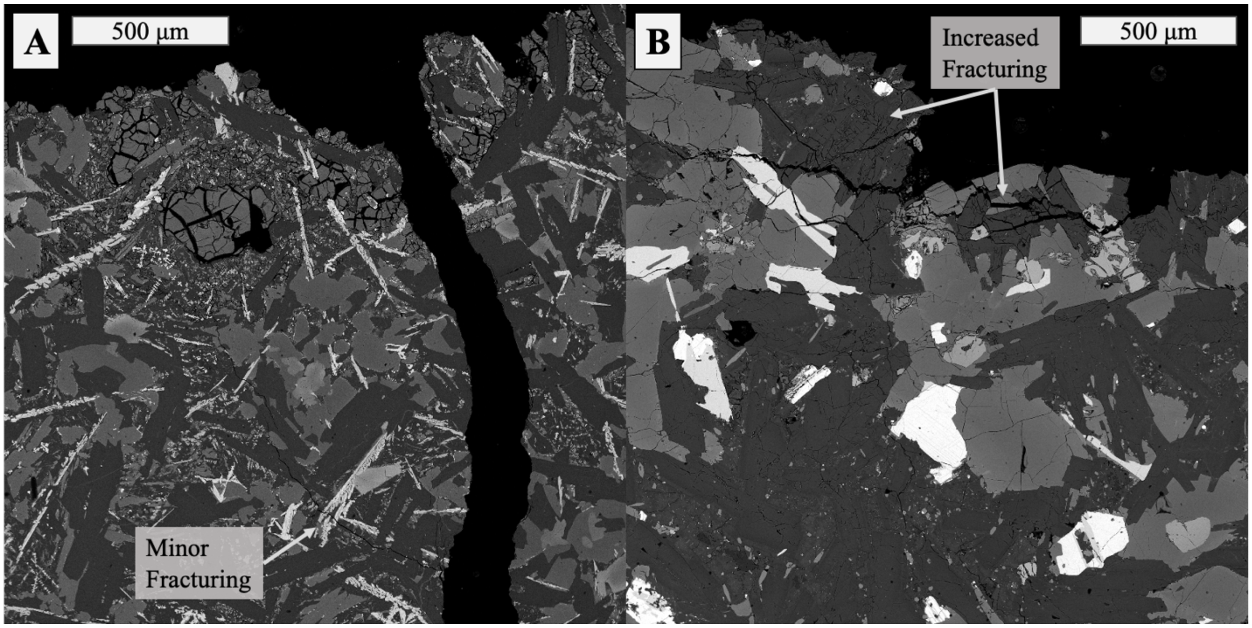

Figure 31: (A) SEM BSE image of FC-18-007's thin section. (B) SEM BSE image of FC-18-005's thin section. There is no great change in porosity in either sample. The more notable texture change is the increase in fracturing visible in image B.

Table 3: Summary of the Columbia River Basalt samples' surface composition and textures.

Sample Name	**Group**	**Surface Composition**	**Texture**	**Thin Section Observations**
DF-18-003 (Int)	Dry Falls, Interior	Pl, Aug, Ol, Ilm, Ap, and felsic glass. An altered mafic phase enriched in Fe relative to DF-18-003-A.	Cut slab; polished to 600 grit	n/a
DF-18-003 (A)	Dry Falls	Pl, Aug, Ol, Ilm, Ap, and a Sme/Vrm clay. Glass and the altered mafic phase are less abundant.	Rough/angular, mix of grain sizes, highest near-surface porosity. Large pits and fractures are widespread where glass and the altered mafic phase are removed	n/a
FC-18-005	Frenchman Coulee	Pl, Aug, Ol, Ilm, Ap, an altered mafic phase, and felsic glass. Fine-grained titanomagnetite common.	Rough/angular, mix of grain sizes, pits and fractures common, small amount of fine-grained material	12% reddening in upper 2 mm

FC-18-007	Frenchman Coulee	Pl, Aug, Ol, Ap, an altered mafic phase, and felsic glass. Abundant Ilm.	Rough/angular, mix of grain sizes, pits and fractures common, elongated ilmenite grains	10% reddening in upper 2 mm
FC-18-008	Frenchman Coulee	Pl, Aug, Ol, Ilm, Ap, an altered mafic phase, and felsic glass. Occasional fine-grained titanomagnetite.	Rough/angular, mix of grain sizes, pits and fractures common	n/a

Andesites

XRD data from one andesite interior (TM-2) indicates the composition is primarily plagioclase with pyroxene, ilmenite, and orthoclase (Figure 32). Thin sections from TM-4 and TM-6 confirm the plagioclase, pyroxene (augite and enstatite), and ilmenite, while expanding the list of minerals present to include: Fe-oxides, apatite, and a felsic matrix (Figure 33). There are no orthoclase phenocrysts visible in the thin sections; orthoclase in the XRD data is from crystallites in the matrix. All the samples are relatively porous compared to the dunites and basalts; this porosity extends through the sample interiors (Figure 33). See Table 4 for individual sample compositions and textures.

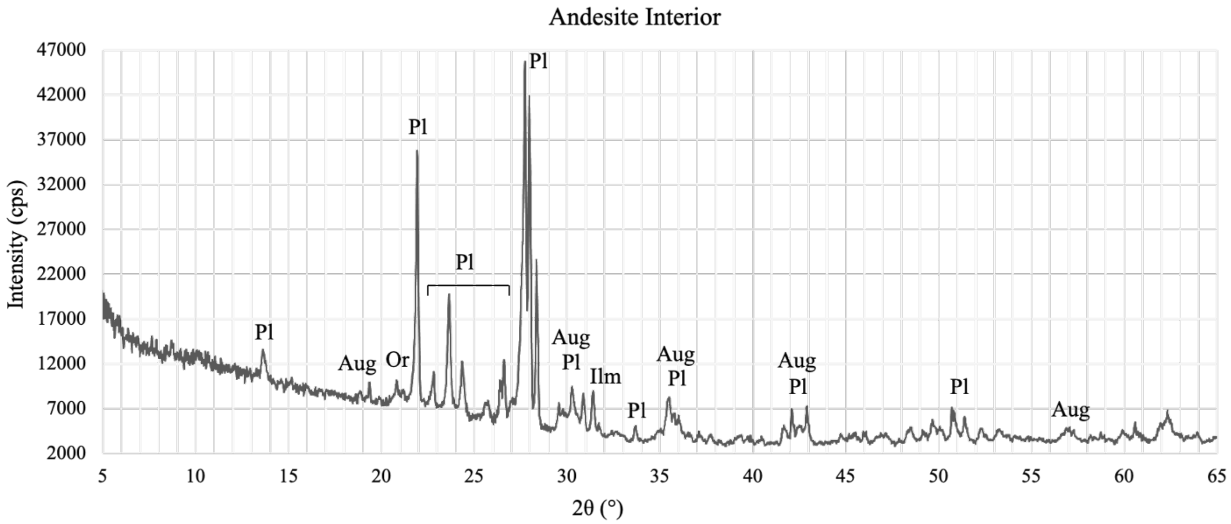

Figure 32: XRD data from TM-2 (bulk interior). The composition is primarily plagioclase and pyroxene, with a small ilmenite peak at 32.5 degrees and an orthoclase peak at 21 degrees..

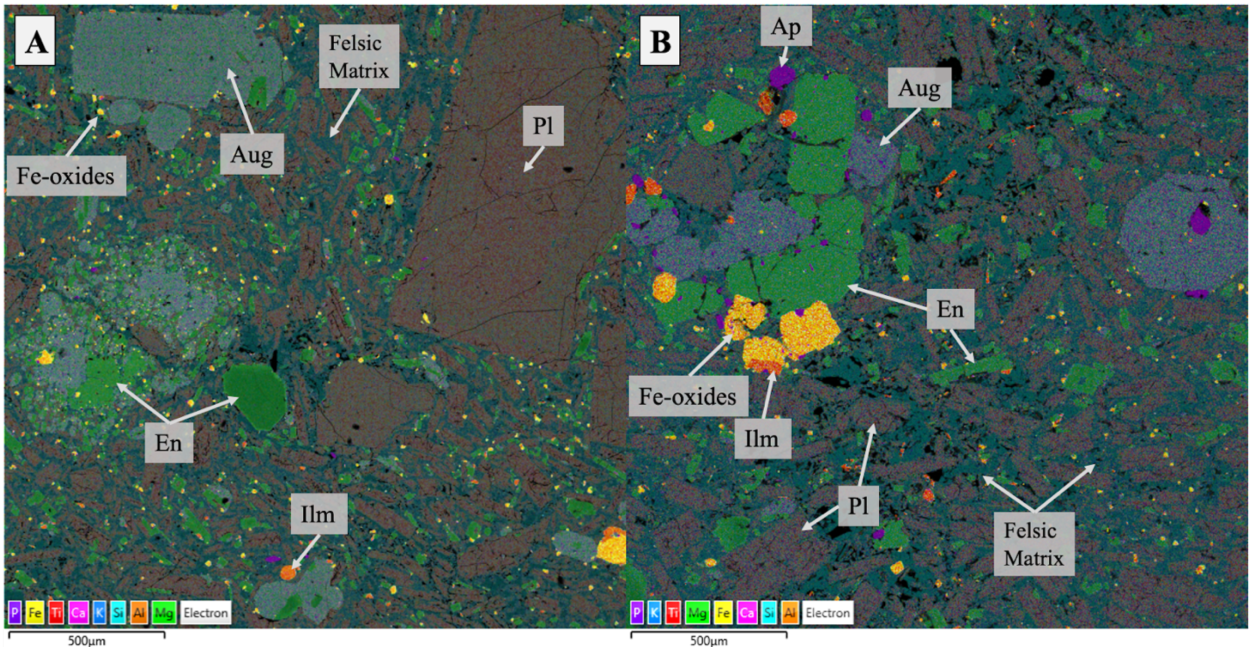

Figure 33: (A) EDS element map of TM-4's thin section. (B) EDS element map of TM-6's thin section. The texture is porphyritic with large plagioclase, augite, and enstatite phenocrysts.

TM-2's naturally weathered surface has the same composition as its interior (Figure 34). There are little to no weathering related Fe-oxides on the surface, and ilmenite grains are relatively small (Figure 34). The brown samples' overall compositions are very similar to each other and the gray samples, but differences appear at the weathered surfaces. XRD data from the

<0.2-µm size-fraction of TM-4 and TM-6's weathering rinds show plagioclase in both, with chlorite in TM-6 (Figure 35). Fe-oxides are much more abundant on the three brown samples' surfaces than TM-2-A. They form a smooth coating that covers much of the surface (Figure 36).

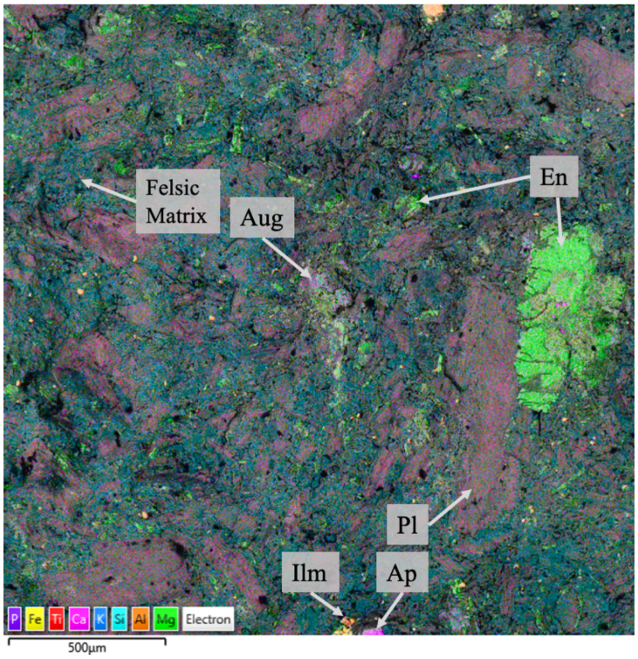

Figure 34: EDS element map of TM-2-A's weathered surface. There is no notable change in composition from the interiors in Figure 33.

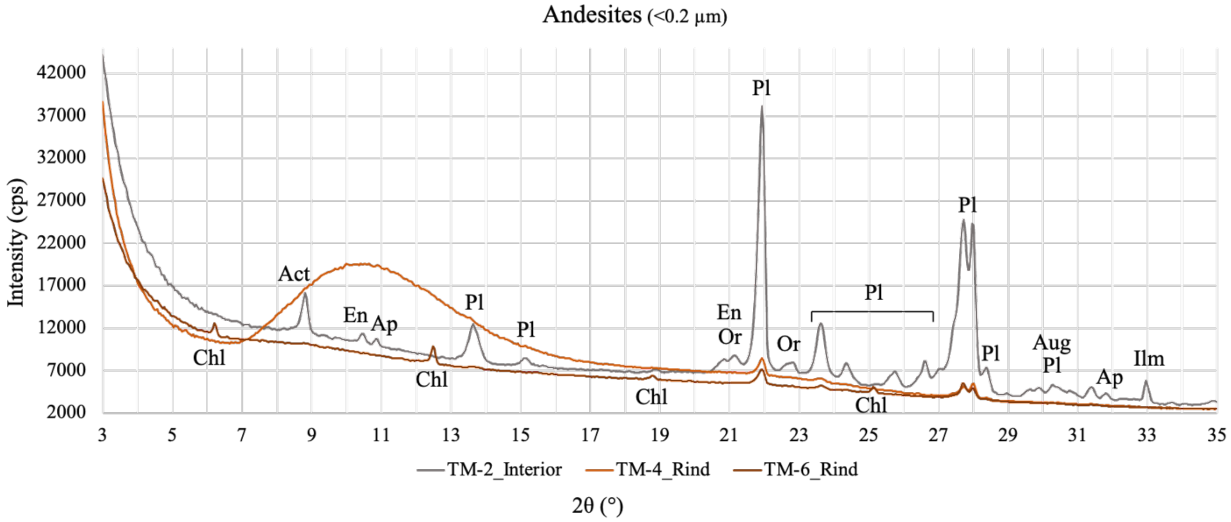

Figure 35: XRD patterns from the <0.2-µm size-fraction of three andesite samples: one interior and two weathering rinds. Plagioclase peaks appear in all three patterns and are largest for the interior sample; the interior also has small orthoclase peaks. A possible actinolite peak is present in the interior sample's data. One weathering rind has clay peaks (labeled as chlorite). The amorphous peak at ~10.5 degrees is an artifact likely related to the sample mount.

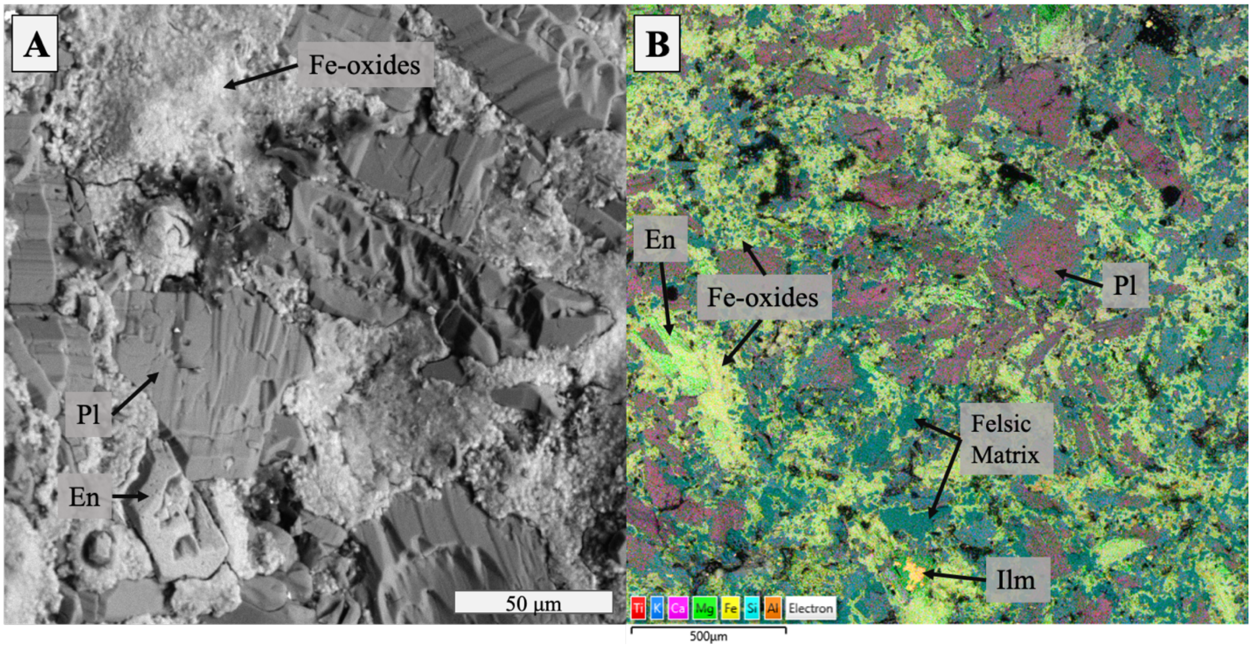

Figure 36: (A) SEM backscatter "shadow" image of TM-3. The Fe-oxides form a coating on the surface that covers the primary minerals and smooths rough edges. (B) EDS element map of a different location on TM-3's surface.

The andesite surfaces are less rough and broken up than the basalts, especially with the Fe-oxide coating smoothing the edges of any angular mineral grains (Figure 37). TM-2-A has the overall smoothest surface and TM-4 has the roughest. Fracturing and shallow depressions are the norm for TM-2-A, but deep pits where materials most susceptible to weathering have been removed are not common (Figure 34). The brown sample surfaces are a mix of smooth plagioclase phenocrysts, rough/angular areas, and smooth Fe-oxide coatings (Figure 37).

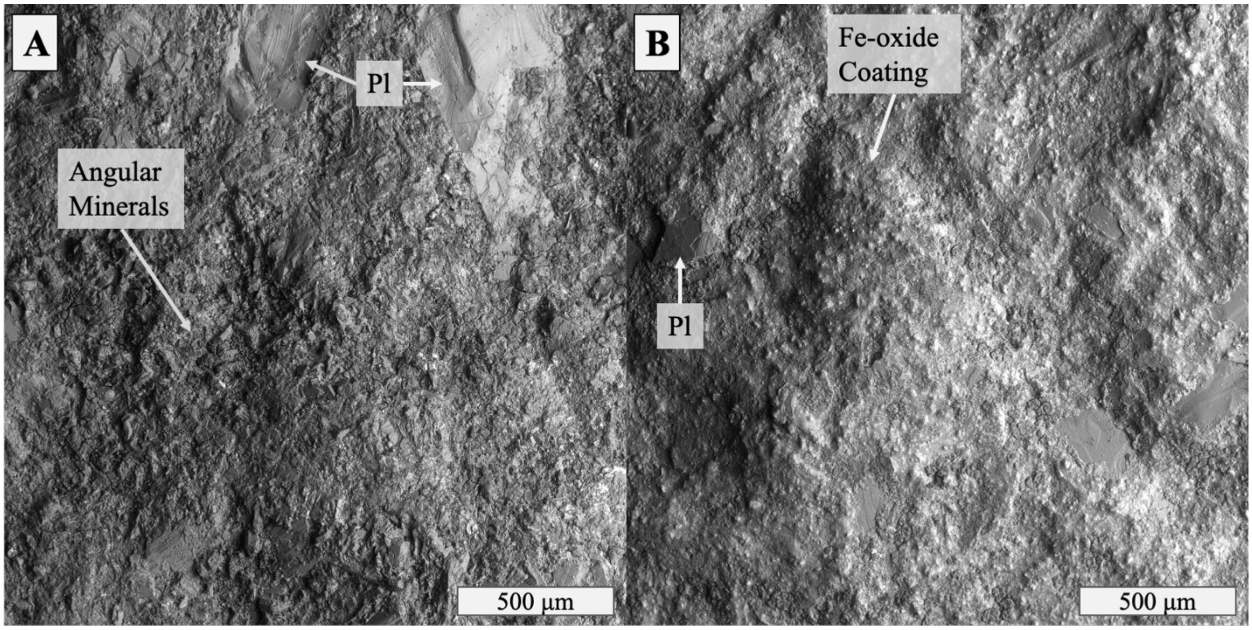

Figure 37: (A) SEM backscatter "shadow" image of TM-4's surface. Of the brown andesites, this surface has the least widespread Fe-oxide coatings, leaving much of the surface angular. (B) SEM backscatter "shadow" image of TM-6's surface. This sample has the most abundant Fe-oxide coatings. They fill in surface depressions and smooth angular mineral edges.

In addition to the surface, Fe-oxides line large fractures within the samples (Figure 38). The images in Figure 38 were taken ~0.5 cm inwards from the weathered surface of one of the brown andesites. Besides the Fe-oxides, reddening in the matrix near the surface fractures are signs of alteration. Unlike the basalts, small fractures in interior phenocrysts (those far from the surface or large fractures) are uncommon and do not show nearly the same level of reddening (Figure 38). Towards the surface, fracturing increases slightly and reddening is more common, but porosity does not change at the scale of these observations.

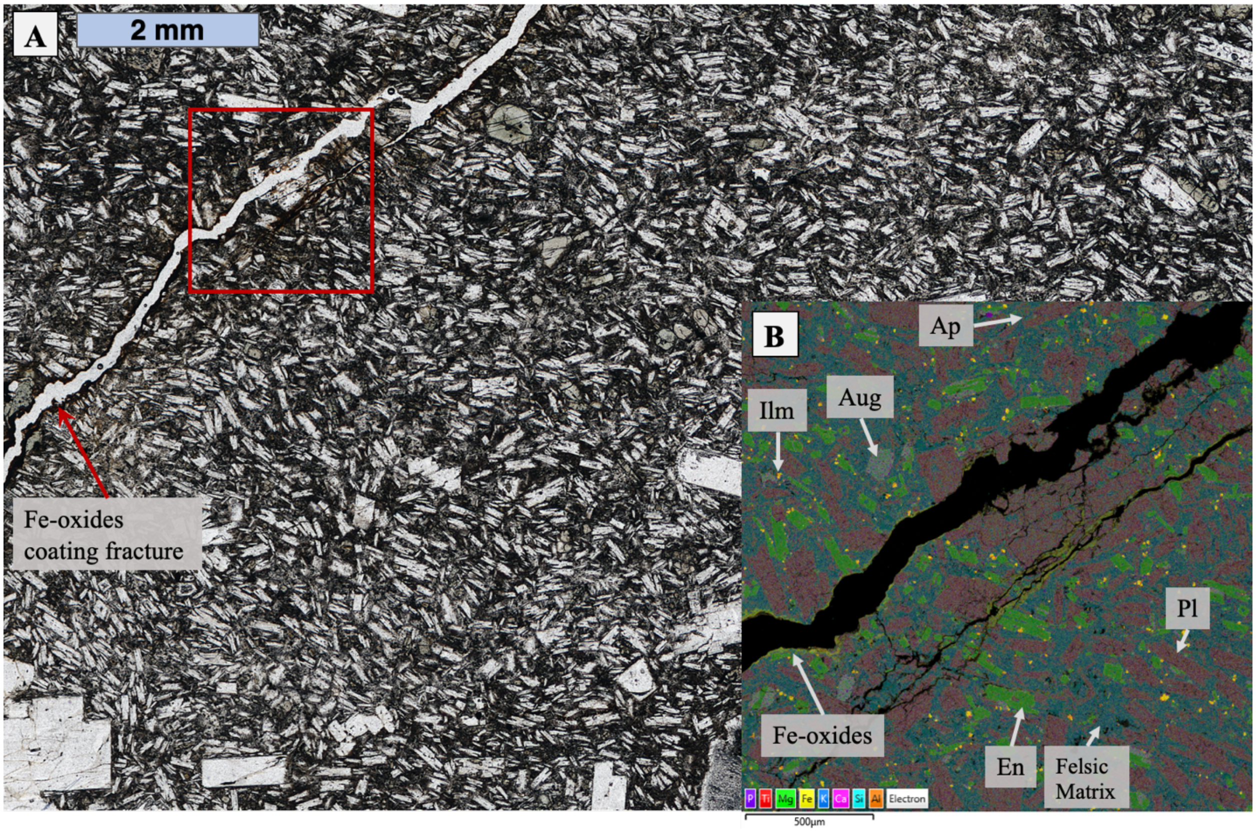

Figure 38: (A) Transmitted light scan of thin section TM-6. (B) An EDS element map of the area outlined by a red square. Reddening in A shows up as yellow Fe-rich coatings in B.

Table 4: Summary of the Table Mountain andesite samples’ surface composition and textures.

Sample Name	**Group**	**Surface Composition**	**Texture**	**Thin Section Observations**
TM-2-A	Gray	Pl, Aug, En, Ilm, Ap, and a felsic matrix. Little to no Fe-oxides	Smoothest andesite, pits and fractures uncommon, phenocrysts create smooth spots	n/a
TM-2-B (Interior)	Gray	Pl, Aug, En, Ilm, Ap, Act, and a felsic matrix	Cut slab; polished to 600 grit	n/a
TM-3	Brown	Pl, Aug, En, Ilm, Fe-oxides, Ap, and a felsic matrix. Moderate Fe-oxide coatings	Plagioclase phenocrysts are surrounded by rough/weathered minerals, abundant Fe-coatings smooth rough edges	n/a

TM-4	Brown	Pl, Aug, En, Ilm, Fe-oxides, Ap, and a felsic matrix. Occasional Fe-oxide coatings.	Plagioclase phenocrysts are surrounded by rough/weathered minerals, intermittent Fe-coatings smooth rough edges	8% reddening in upper 2 mm
TM-6	Brown	Pl, Aug, En, Ilm, Fe-oxides, Ap, and a felsic matrix, and Chl/Sme clay. Abundant Fe-oxide coatings.	Plagioclase phenocrysts are surrounded by rough/weathered minerals, abundant Fe-coatings smooth rough edges	6% reddening in upper 2 mm

Spectroscopy

Pure Mineral Examples

Figure 39 below includes examples of pure mineral spectra from several rock forming minerals, and a handful of oxides and clays that could be present in the samples or on their weathered surfaces. These and other lab spectra of pure minerals are publicly available on the Western Washington University Vibisle-Infrared Spectral Browser (VISOR) database (Million et al., 2022; St. Clair et al., 2022). The original source of the spectra are: University of Winnipeg Spectrophotometer Facility (most of the reference spectra), ASTER / ECOSTRESS Spectral Library, and CSIRO National Virtual Core Library.

Diagnostic features for olivine include a peak in the visible range and a wide, deep absorption band at ~1050 nm. Clinopyroxene has two peaks at ~550 and ~850 nm, with a smaller absorption band at ~1050 nm. Orthopyroxene has wide, deep bands at ~915 and ~1850 nm. In the VNIR range, feldspar diagnostic features are easier to spot at longer wavelengths. Chromite and spinel have wide peaks across ~1100-1400 nm, with small absorption bands in the visible range. The Fe-oxides have one to two relatively narrow peaks in the visible range (the taller of the two at ~750 nm), followed by an absorption band, then a large increase in reflectance into the near-infrared. Chlorite and illite have peaks similar to olivine and clinopyroxene in the visible range, but they have a larger reflectance increase through the near-infrared. Clay spectra have clear hydration related absorptions at ~1400 nm, ~1900 nm, and in the 2000+ nm range; the positions of absorption band centers relative to each other indicate which clay is present. Nontronite stands out with its Fe-rich composition and hematite-like peaks in the visible range.

JSC Mars-1 is a nanophase Fe-oxide and analog for Mars dust. It is included here because all Mars spectra have some contribution from the ferric dust, even relatively fresh rocks in the abrasion patches. The spectrum has a bend at ~500 nm where the slope increases and a local maximum at ~750 nm. It has absorption bands at ~1400, ~1900, and ~2200 nm.

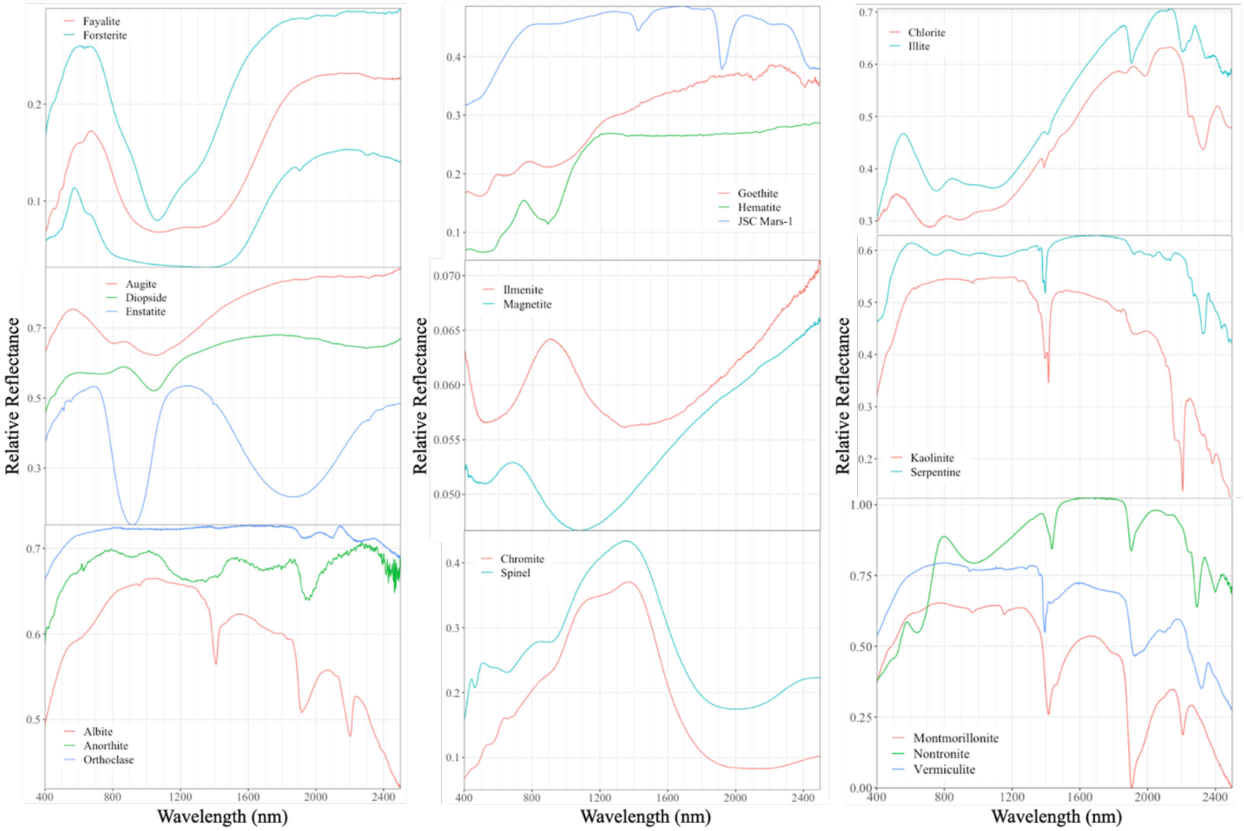

Figure 39: Reference spectra of primary minerals, oxides, and clays that can be present on weathered surfaces.

Dunites

Spectra from the green dunites are predominantly forsterite shaped with serpentine characteristics in the longer wavelengths (Figure 40). TS-20-28 and TS-20-02-3 have broad peaks centered at ~550 nm and deep and wide absorption bands centered at ~1050 nm. The spectrum from TS-20-01-5-B has a similar shape to the other two samples in the near-infrared range (800 nm and longer), with characteristics of more Fe-rich surfaces in the visible range: a steep slope up to a local maximum at ~700 nm. All three samples have absorption bands indicative of hydration at ~1400 nm (OH/H_2O), ~1900 nm (H_2O and/or pyroxene), and ~2320 nm (Mg-OH). In addition to these absorption features, the wide ~1900 nm band, two small peaks at ~2060 nm and ~2150 nm, and steep negative slope after 2200 nm are serpentine features.

The tan dunites have steep slopes leading up to local maximums close to 700 nm, and are more similar to TS-20-01-5-B than TS-20-28 or TS-20-02-3 (Figure 40). Wide forsterite-like absorption bands are centered around ~1050 nm (Figure 39). Absorption bands at ~1900 nm and ~2320 nm, as well as tiny bands at ~1400 nm, indicate hydration is present.

Spectra from the red dunites have steep positive slopes from 400 to 750 nm, with a local maximum at ~750 nm (Figure 40). A subtle absorption band at ~850 nm and the relatively narrow peak at ~750 nm indicate hematite is present on the sample surface (Figure 39). Both samples have an absorption band at ~1050 nm, and TS-20-05 has a small peak at ~925 nm. Absorption bands at ~1900 nm indicate the presence of H_2O, and the band at ~2310 nm is a metal-hydroxide.

Spectra from the brown dunites have positive slopes with little variation from 400 nm to ~1650 nm (Figure 40). There are slight changes in concavity at ~700 nm, ~900 nm, and ~1050 nm, probably from peaks and absorption bands that are being obscured by the surfaces' dark brown color and abundance of carbon. Small dips at ~1450 nm in both samples hint at subtle hydration related absorption bands; more obvious absorption bands at ~1920 nm and ~2300 nm are also caused by hydration. There are several small absorption bands in the longer wavelengths (1900 nm and longer); the specific bands indicate a mix of orthoclase and a smectite clay (Figure 39).

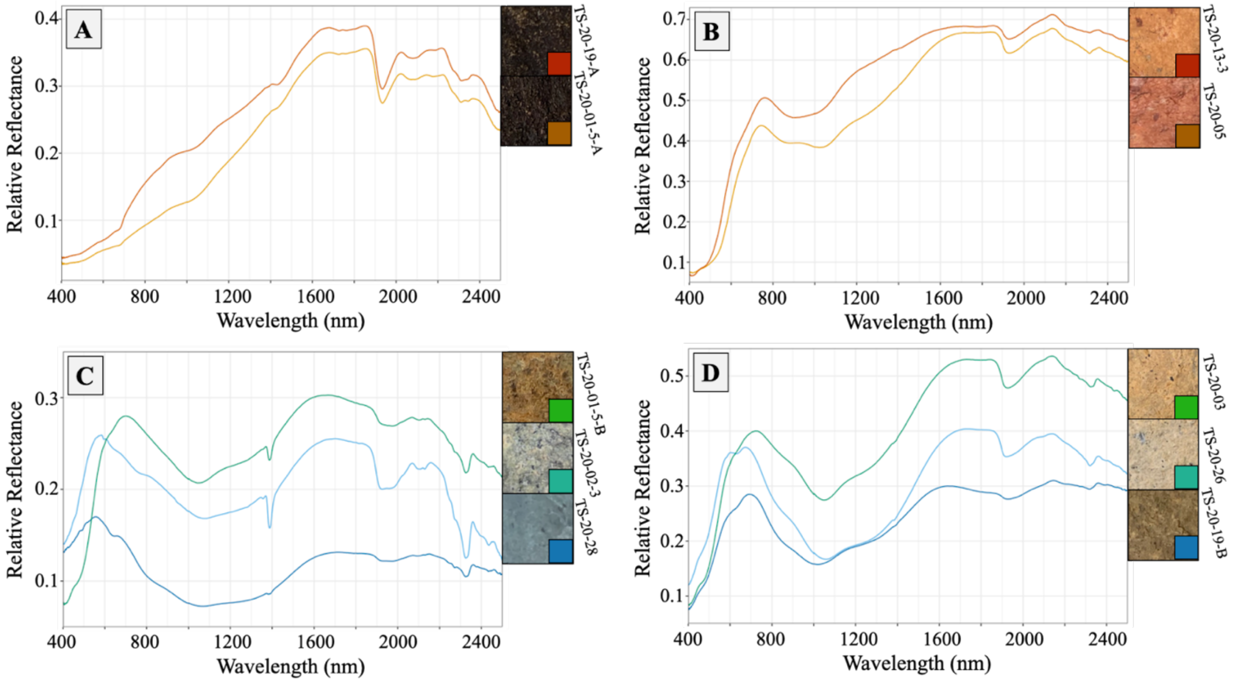

Figure 40: Spectra from (A) the brown dunites, (B) the red dunites, (C) the green dunites, and (D) the tan dunites. Viewing geometry: i=30, e=0, az=0. A spectral artifact between 2100-2200 nm creates a small artificial peak that can complicate mineral identification when using those wavelengths; see “Known Complications” in the Discussion Section for more details.

Spectra collected from the red dunites using the small diameter probe show similar compositional changes across single samples as across the whole dunite sample set (Figure 41). Spectra from points C and D on both samples are forsterite-like. Spectra from point A on TS-20-05’s cross section is hematite-like.

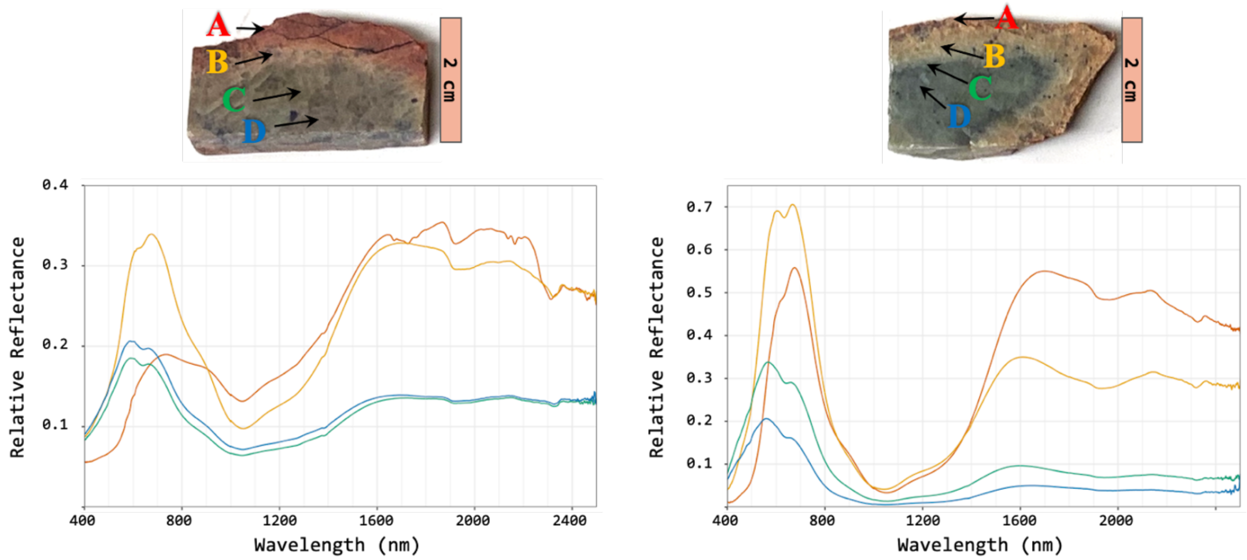

Figure 41: Spectra collected from two dunite cross sections using the small diameter probe. Arrows and color-coded labels on the included images show where on the cross section each spectrum was taken. On both plots the blue spectrum was taken furthest toward the sample interior and the red spectrum was taken closest to the surface. For scale, each sample cross section is ~2 cm tall. A spectral artifact between 2100-2200 nm creates a small artificial peak; see "Known Complications" in the Discussion Section for more details.

Basalts

In a standard viewing geometry (i=30, e=0, az=0), the five basalt slabs have a smaller range in reflectances than that of the dunites (Figure 42). FC-18-005 has the highest relative reflectance at just over 0.2, while in the dunite group TS-20-13-3's reflectance is up to 0.7 in the longer wavelengths (Figure 40). The DF-18-003-Int spectrum is very flat, while the four natural surfaces start out with an absorption band at <400 nm. They have a positive slope from 400 nm to a peak between 750-850 nm; the exact location of the peak varies by sample. On top of their wide peaks in that region, DF-18-003-A and FC-18-008 have small bumps at ~580 nm, ~750 nm, and ~850 nm (Figure 42). These indicate clinopyroxene (peaks at ~580 nm and ~850 nm) and plagioclase (peak at ~750 nm) are present (Figure 39). DF-18-003-Int has no peak in the visible range, and instead has a negative slope from 400 nm to a local minimum centered around ~1000 nm. All five spectra have minima in this region from two partially overlapping clinopyroxene absorption bands: ~950 nm and ~1040 nm. Two of the Frenchman Coulee samples: FC-18-005 and FC-18-007 are more Fe-oxide-like than the other three samples. FC-18-005's steep slope up to a relatively narrow peak at ~780 nm is similar to hematite and goethite (Figure 39). FC-18-007 has a spectral shape intermediate between the more pyroxene-like samples and FC-18-005.

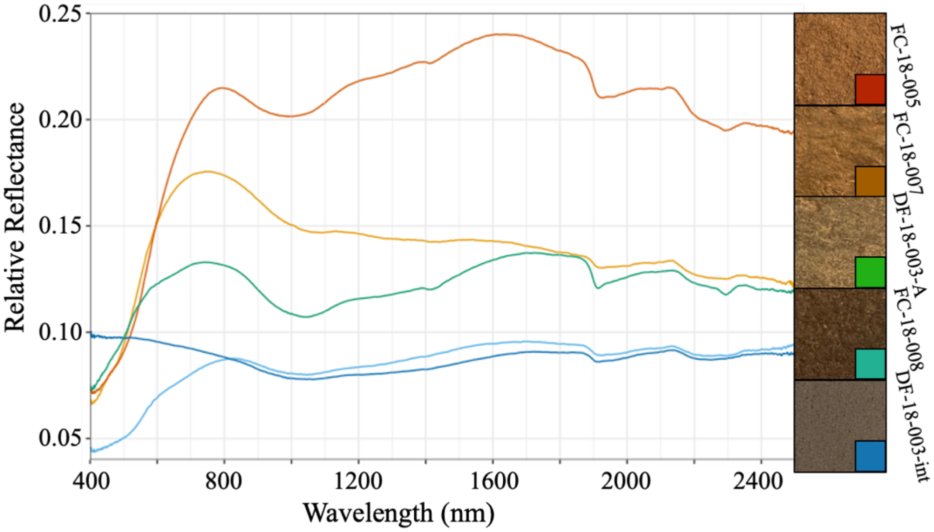

Figure 42: Spectra from five basalt slabs. The blue spectrum is DF-18-003-Int: the smooth slab cut from a rock interior. The other four spectra are naturally weathered surfaces. Viewing geometry: i=30, e=0, az=0. The key shows images of the surfaces spectra were taken from; each sample image is approximately 4 cm across. A spectral artifact between 2100-2200 nm creates a small artificial peak; see "Known Complications" in the Discussion Section for more details.

Andesites

Between 400-700 nm, spectra from the andesite natural surfaces differ greatly from the interior slab. The interior (TM-2-B) has a relatively high reflectance in the short wavelengths and reaches a local maximum at ~550 nm (Figure 43). The natural surfaces start with lower reflectances and steep positive slopes to local maxima at ~750 nm (Figure 43). All samples have a wide absorption band at ~915 nm that indicates the presence of enstatite (Figure 39). Hydration bands at 1400 nm, 1900 nm, and 2300 nm are present in spectra from all the natural surfaces. The brown samples may have absorption bands at 2200 nm as well, but a spectral artifact in that range makes it difficult to tell for sure (see Discussion Section for a more in-depth explanation of the artifact). The hydration bands are very faint in the interior slab's spectrum. The pattern of absorption bands for the brown samples is similar to that of smectite clays (especially nontronite), chlorite, and plagioclase (Figure 39).

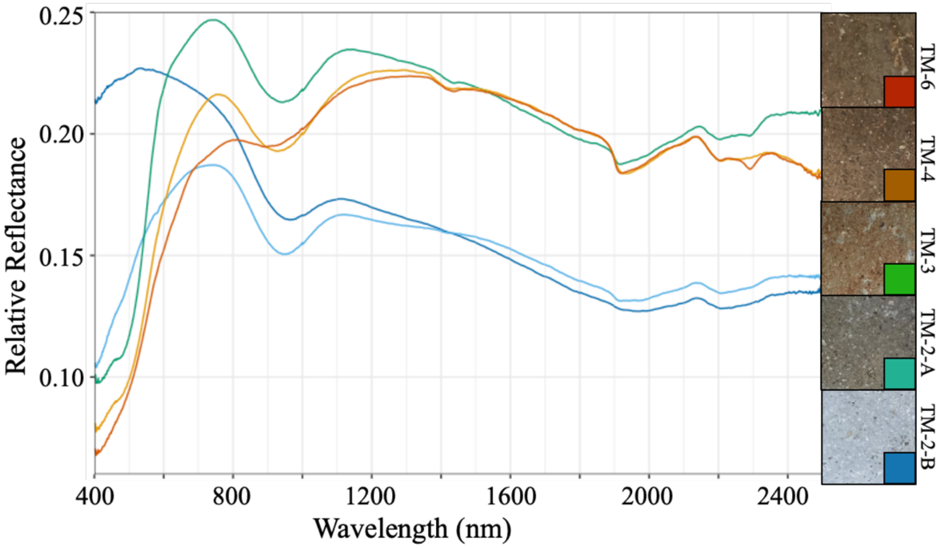

Figure 43: Spectra from five andesite slabs. The blue spectrum is TM-2-B: the smooth slab cut from a rock interior. The other four spectra are naturally weathered surfaces. Viewing geometry: i=30, e=0, az=0. The key shows images of the surfaces spectra were taken from; each sample image is approximately 4 cm across. A spectral artifact between 2100-2200 nm creates a small artificial peak; see "Known Complications" in the Discussion Section for more details.

Scattering Behavior

Reflectances are highest for forward scattering samples when phase angles are large (Figure 44). Their normalized spectra are flattest when phase angle is large as well; local maxima and minima are relatively larger when phase angle is small. In other words, the most red sloped spectra are recorded in forward scattering geometries. Backscattering samples have the reverse trend: high reflectances and flattest normalized spectra are recorded when phase angle is small (Figure 44).

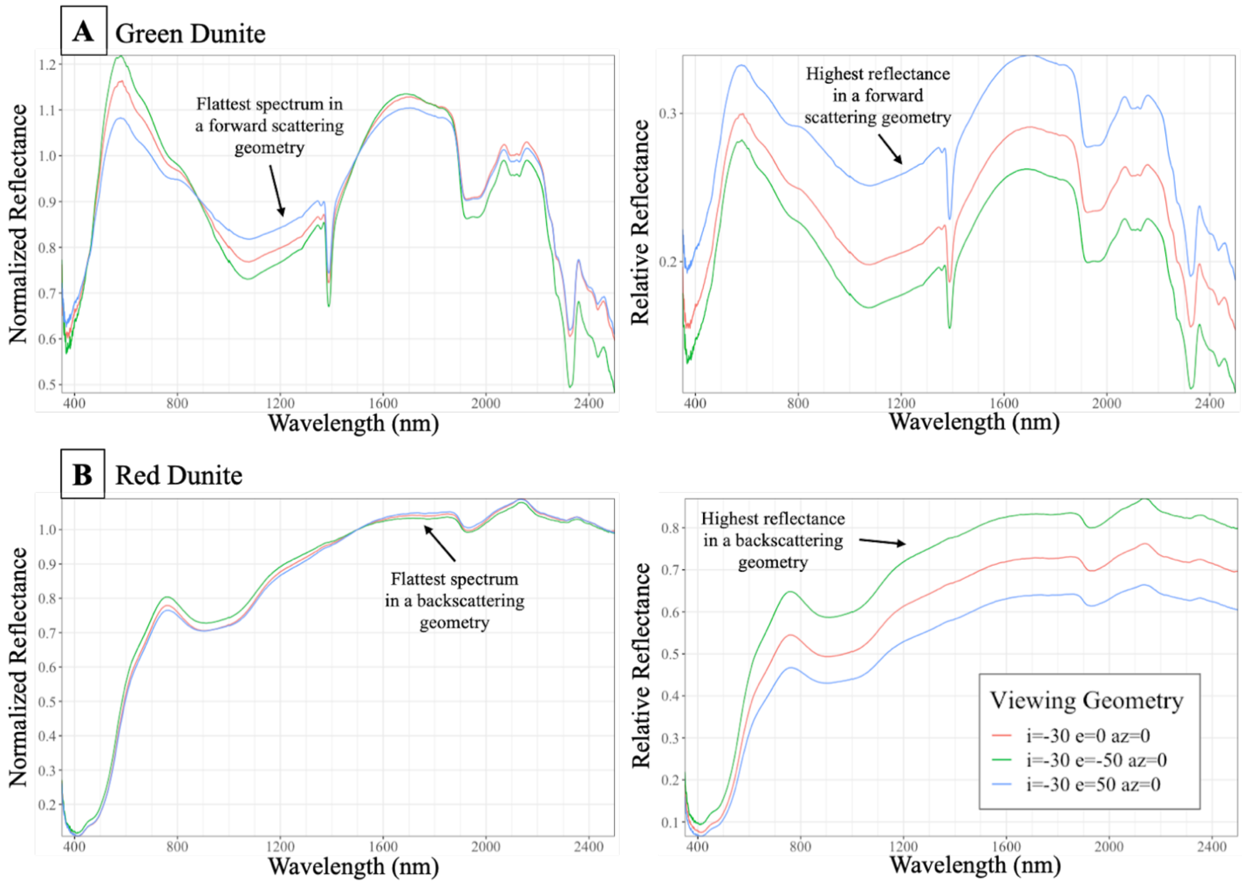

Figure 44: Spectra from (A) one green dunite and (B) one red dunite at three different viewing geometries (standard, backscattering, and forward scattering). The left panels are normalized to 1.0 at 1500 nm.

The interior dunite slab (TS-20-28) and relatively unweathered slab (TS-20-02-3) are strongly forward scattering while the other 8 dunite samples are strongly backscattering (Figure 44). TS-20-02-3 has a small uptick in reflectance on the backscatter side that the interior slab, TS-20-28, does not. All other dunite samples are strongly backscattering; reflectance is highest when the emission angle is negative and light is bouncing back toward the source.

The 2-dimensional scattering plots in Figures 44, 46, and 47 plot reflectance on the radial axis (increasing outwards) and emission angle across the outer edge of the semi-circle. There is an orange line on each plot set to i=-50 showing the direction of incident light. Samples that lean away from the orange line are forward scattering, and samples that lean back towards it are backscattering. Samples with more complex behavior, for example a “V” shape, are usually a mix of forward and backscattering. Azimuth equals zero on all the semi-circle scattering plots.

When the incidence angle is large, the Spectralon’s Lambertian behavior begins to break down. Here I use i=-50 for the scattering plots, which is right on the edge of trusted geometries for the calibration; however, I am confident the results shown here with i=-50 are trustworthy because the plots look nearly the same as those with i=-40.

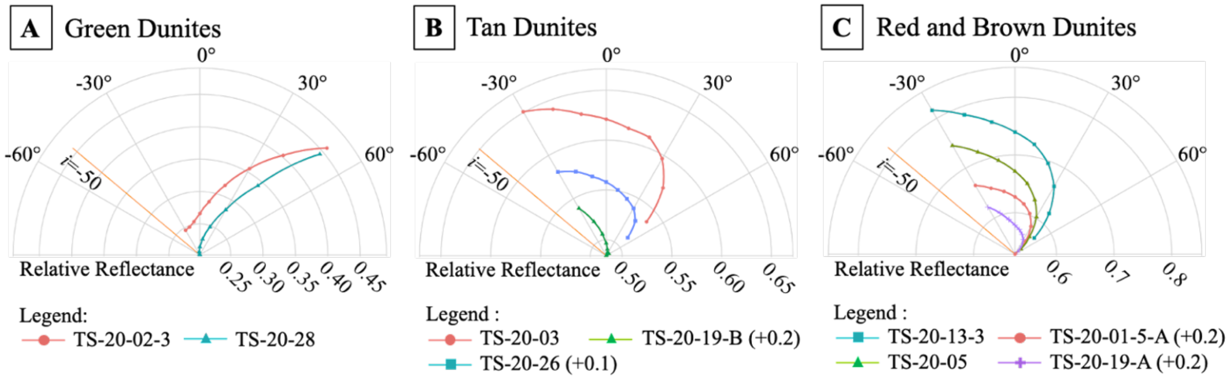

Figure 45: Scattering behavior in the az=0 plane for (A) two of the green dunites, (B) the tan dunites, and (C) the red and brown dunites. Incident light is -50 degrees from vertical (the orange line). Reflectance between 1700-1705 nm is averaged for each sample; these wavelengths were selected because reflectance is relatively flat in this region across all samples. Reflectance increases outwards radially from the bottom center of each plot. Some samples’ reflectance are offset so they can fit on the plots together.

3D plots of average reflectance show the highest reflectance tends to be in the same plane as the incident light, in other words when az = 0 and 180 (Figure 46). This is true for both backscattering and forward scattering samples. The 3-dimensional plots in Figure 46 below takes the half-circle scattering plots and wraps them around multiple azimuth angles to create “rainbow beach umbrella” scattering plots. In the top-down view of these plots (Figure 46), one can imagine the sample is placed directly under the center dot; light comes in along the orange line and bounces off the sample to all the black dots. Each dot is a detector that records the reflectance at its position. Reflectance between 3-4 dots are averaged and color is assigned based on reflectance magnitude – high reflectances are red and low reflectances are blue. Red zones opposite the orange line are forward scattering (the green dunite in Figure 46), and red zones near the orange line are backscattering (the red dunite in Figure 46).

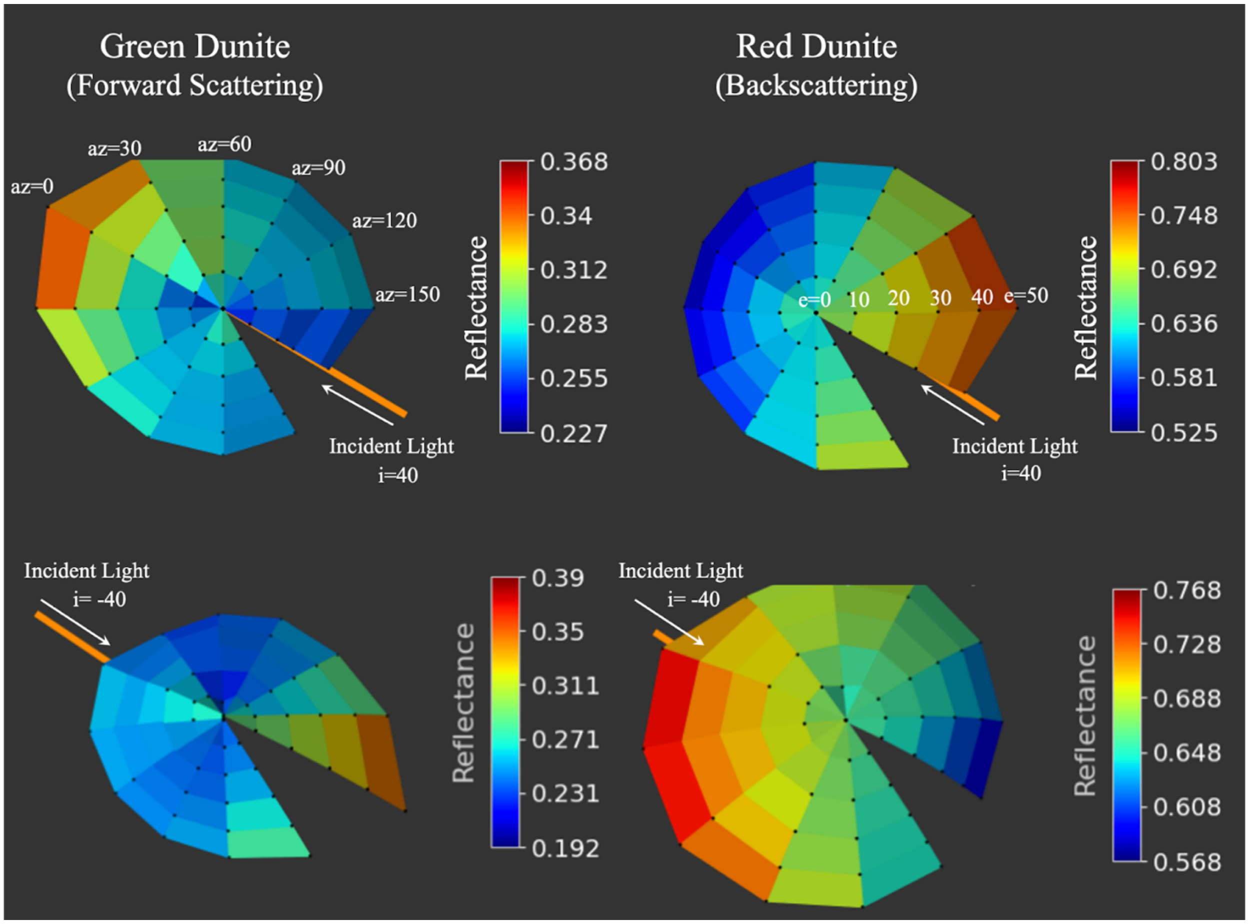

Figure 46: Plots showing how reflectance changes with viewing geometry for one green (TS-20-02-3) and one red (TS-20-05) dunite; reflectance is averaged over 1600-1700 nm. The orange line represents incident light. The black dots represent emission angles. Highest reflectance values are in or close to the az=0 plane.

Of the five basalt samples, DF-18-003-Int is the only one that is fully forward scattering (Figure 47). All four naturally weathered surfaces have two scattering lobes; three are slightly more backscattering than forward and their reflectances are lowest when the detector is at e=0 (Figure 47). FC-18-005, one of the more red basalts, is primarily backscattering with only a small uptick in reflectance on the forward scattering side of its plot in Figure 47. Like the dunites, the highest reflectances measured from all five basalt samples are in geometries where the detector is in the same plane as the light source (az=0).

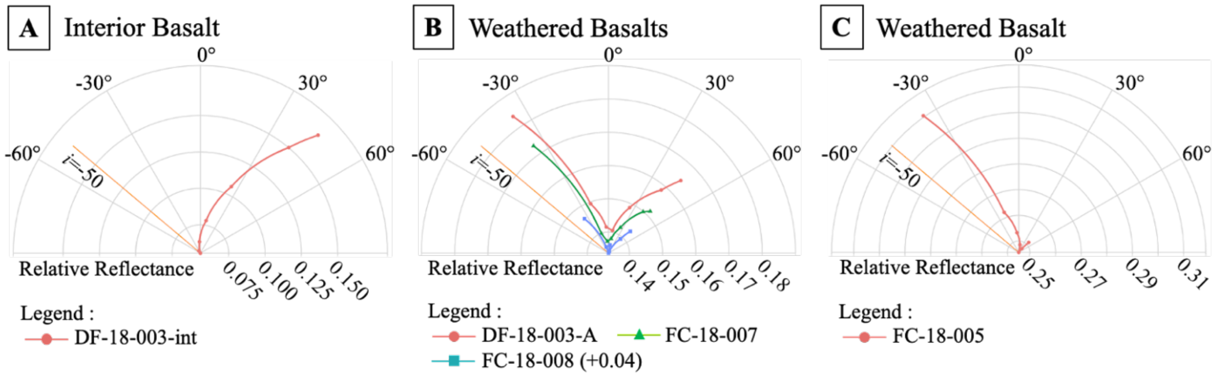

Figure 47: Scattering behavior in the az=0 plane for (A) an interior basalt slab (DF-18-003-Int), (B) three natural basalt surfaces with two scattering lobes each, and (C) one backscattering natural basalt surface. Incident light is -50 degrees from vertical (the orange line). Reflectance between 1700-1705 nm was averaged for each sample; these wavelengths were selected because reflectance is relatively flat in this region across all samples. Reflectance increases outwards radially from the bottom center of each plot. Some samples' reflectance are offset so they can fit on the plots together.

Three andesite samples are strongly forward scattering: the interior slab, the gray natural surface, and one brown sample (TM-3) (Figure 48). Two of the brown samples (TM-4 and TM-6) have two scattering lobes; their lowest reflectances are measured when the detector is almost directly above the sample (Figure 48). TM-4 has roughly even forward and backscattering lobes, while TM-6 is skewed slightly towards forwards scattering. Like the previous rock types, the highest reflectances are measured in the same plane as the incident light (az=0).

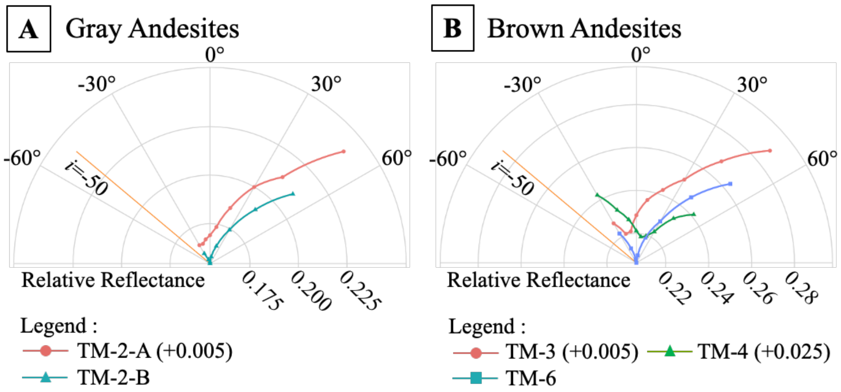

Figure 48: Scattering behavior in the az=0 plane for (A) the gray andesites and (B) the brown andesites. Incident light is -50 degrees from vertical (the orange line). Reflectance between 1700-1705 nm was averaged for each sample; these wavelengths were selected because reflectance is relatively flat in this region across all samples. Reflectance increases outwards radially from the bottom center of each plot. Some samples are offset so they can fit on the plots together.

Band Center vs Viewing Geometry

The specific wavelengths of absorption features can shift as viewing geometry changes, even when the spectra are collected from the same spot on a sample. The positions of absorption bands and reflectance peaks are important to understand because they are critical for mineral identification from spectra. Irregular surface compositions and textures mean each viewing geometry will record a slightly different spectrum, but my data indicate no correlation between band center position and phase angle (Figure 49). Band centers were calculated using the method outlined in Hoza (2019) with the shoulder values indicated in the Figure 49 caption.

Traditional spectral plots with wavelength on the x-axis and reflectance on the y-axis can be difficult to read when many spectra are plotted on the same panel. When looking at how a single spectral parameter changes between viewing geometries it can be easier to use a heat map like Figure 49. Emission and incidence angles are plotted on the x- and y-axes, and color is used to represent the parameter of interest, in this case band center position. The corners of the plots are forward and backscattering zones. If there was a correlation between band center and phase angle, the corners would be solid triangles of bright yellow or dark blue to indicate the centers are shifting up or down depending on viewing geometry.

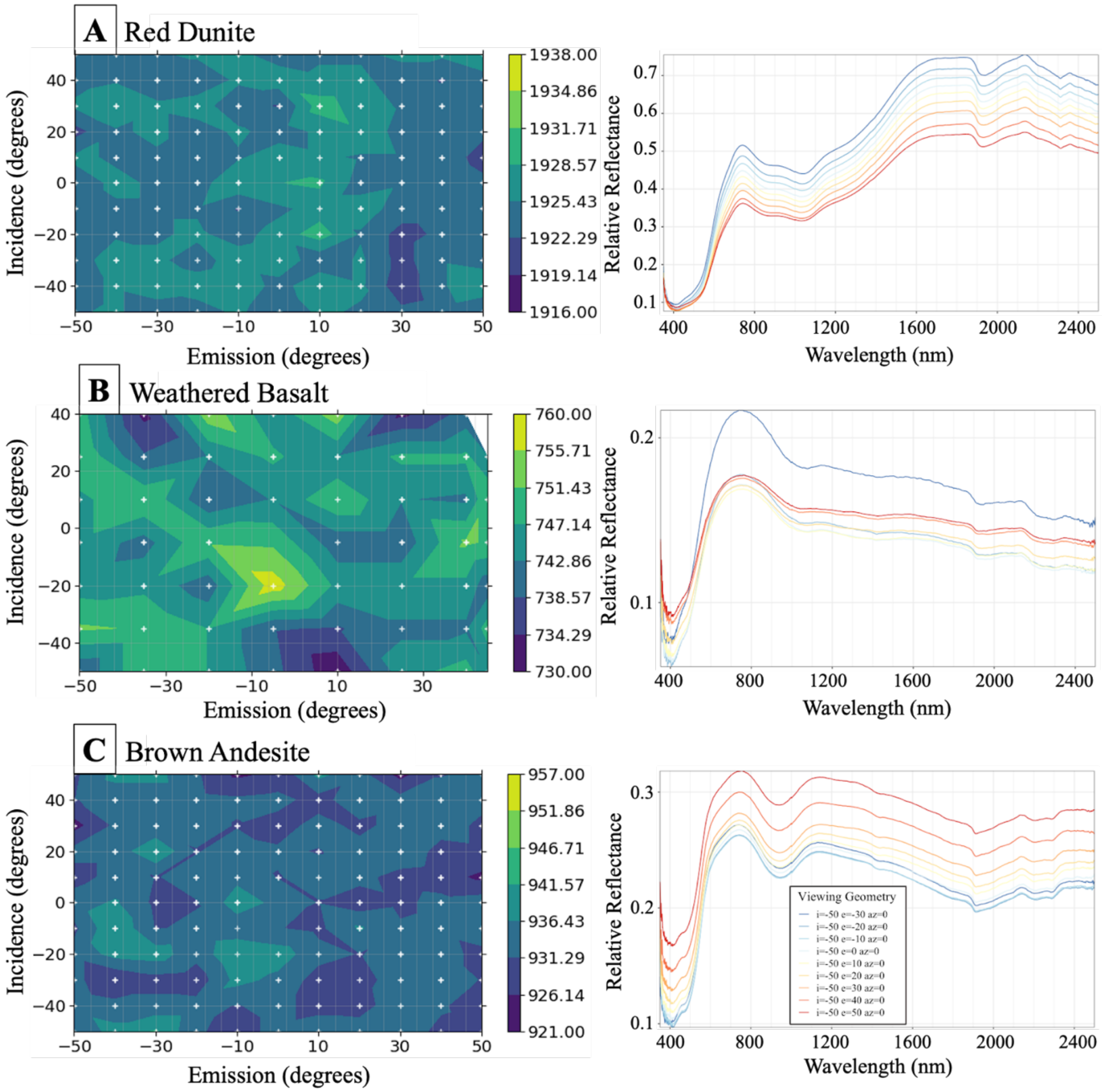

Figure 49: Incident vs emission angle plots of 3 samples, one per rock type; color represents an absorption band's center at a given geometry. (A) TS-20-05's ~1928 nm band center was calculated using 1870 and 2010 nm as its shoulders, (B) FC-18-007's ~745 nm peak center was calculated using 600 and 950 nm as its shoulders, and (C) TM-3's ~935 nm band center was calculated using 750 and 1100 nm as its shoulders.

Band Depth vs Viewing Geometry

Finding band depths is an intermediate step in calculating band centers; plotting band depths versus phase angle logically follows since the data was ready to go. Unlike the band centers, absorption band depth changes do correlate to changes in viewing geometry. As phase angles increase, band depths decrease (Figure 50). This happens across all three rock types and regardless of whether the rock surface is an interior slab, a naturally weathered surface, forwards scattering, or backscattering. Band depths were calculated using the method outlined in Hoza (2019) with the shoulder values listed in the Figure 50 caption.

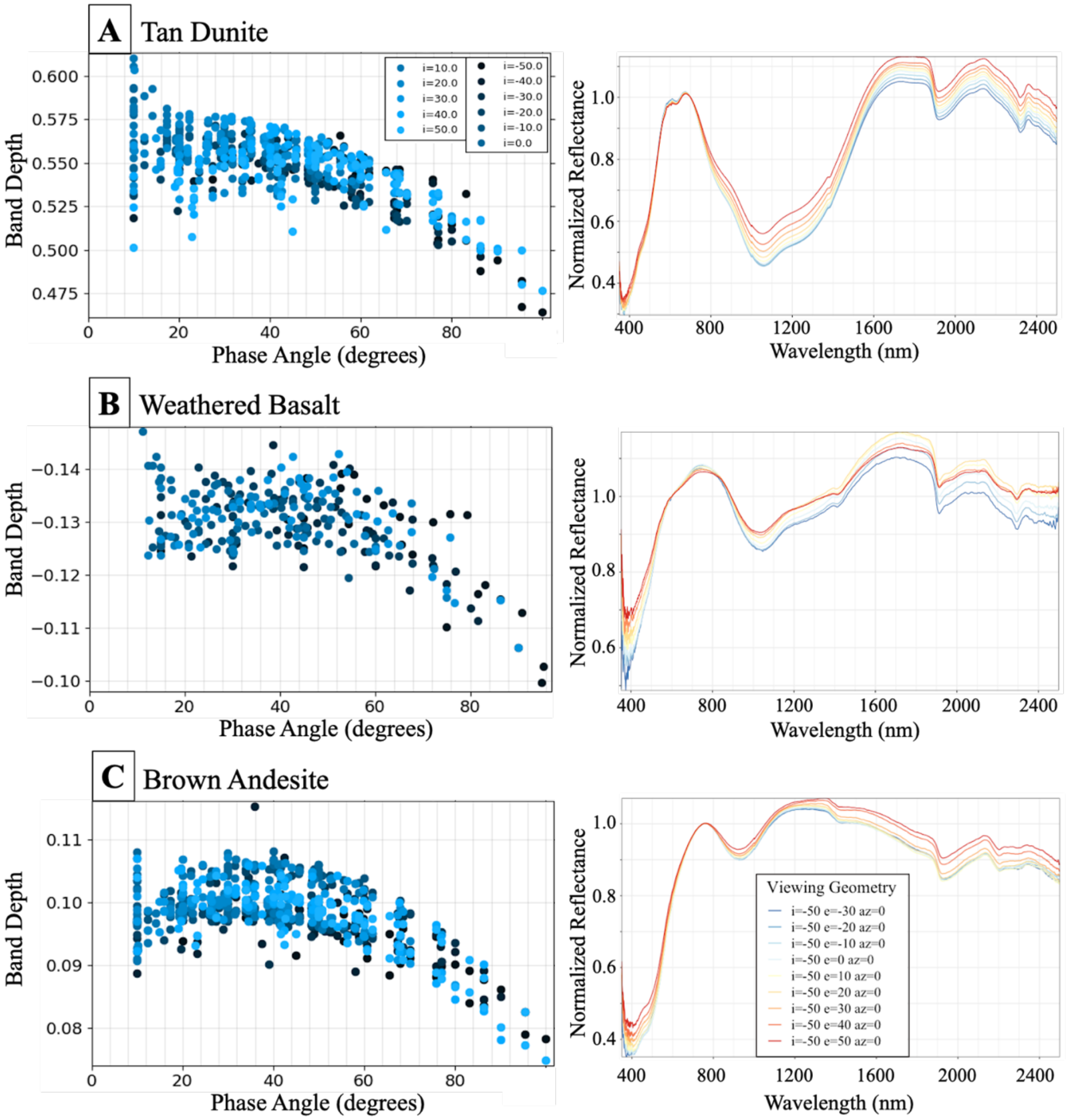

Figure 50: Band depth vs phase angle of three samples, one per rock type, and spectra at a range of geometries normalized to one shoulder. (A) TS-20-26's ~1050 nm band center was calculated using 700 and 1700 nm as its shoulders. (B) DF-18-003-A's ~750 nm peak center was calculated using 600 and 950 nm as its shoulders. (C) TM-4's 935 nm band center was calculated using 750 and 1100 nm as its shoulders. Dot color represents incidence angle.

Near-infrared Slope vs Viewing Geometry

Regardless of scattering behavior, near-infrared slopes (calculated over 1700-2400 nm) increase as phase angle increases (Figure 51). They are most negative in backscattering geometries. For some samples, the NIR slope is relatively flat and shifts from negative to positive with increasing phase angle; however, for most of the samples studied here the slope is alway negative, and shifts from more to less negative with increasing phase angle.

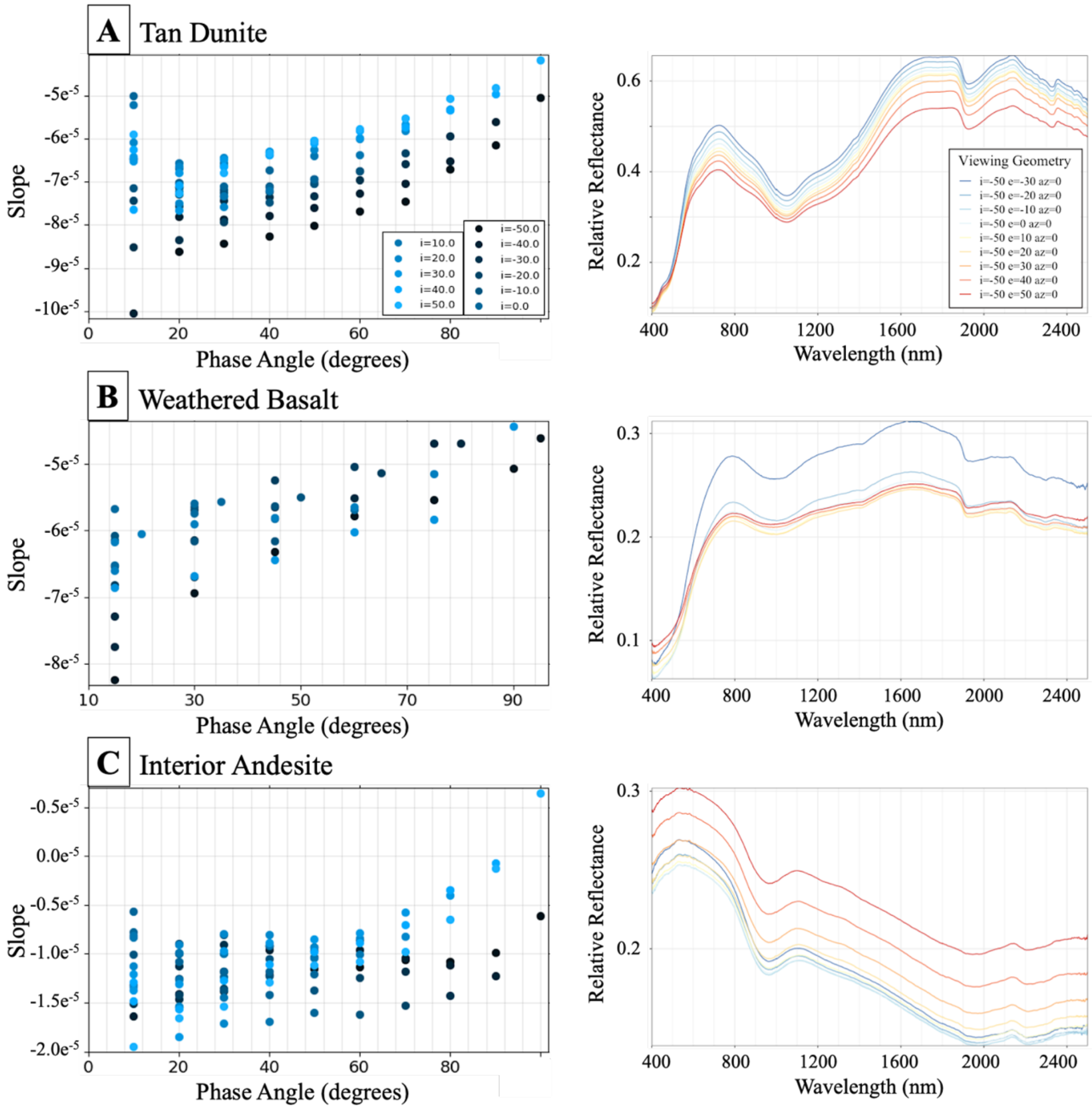

Figure 51: NIR slope vs phase angle of three samples, one per rock type. Slopes are calculated between 1700-2400 nm for (A) TS-20-03, (B) FC-18-005, and (C) TM-2-B.

Mars Data

Spectra from three Séítah abrasion patches are consistent with the presence of olivine. The spectra were collected from fresh rock faces at an abrasion depth of ~2 mm (Figure 52). In the context images, the colorful circles highlight regions of interest where spectra were collected (Figure 52). The abrasion patch spectra all have a positive slope from 442 nm to a peak at 677 nm (Figure 52). Moving to longer wavelengths, there is a steep negative slope from 754 nm to 866 nm. A peak in the 650-700 nm range is consistent with Fe-rich olivine (fayalite) (Figure 39). The purple spectrum taken from a coating has a peak at 754 nm and a slight absorption at 866 nm that give it a ferric dust or hematite-like shape (Figure 39; Rice et al., 2022a).

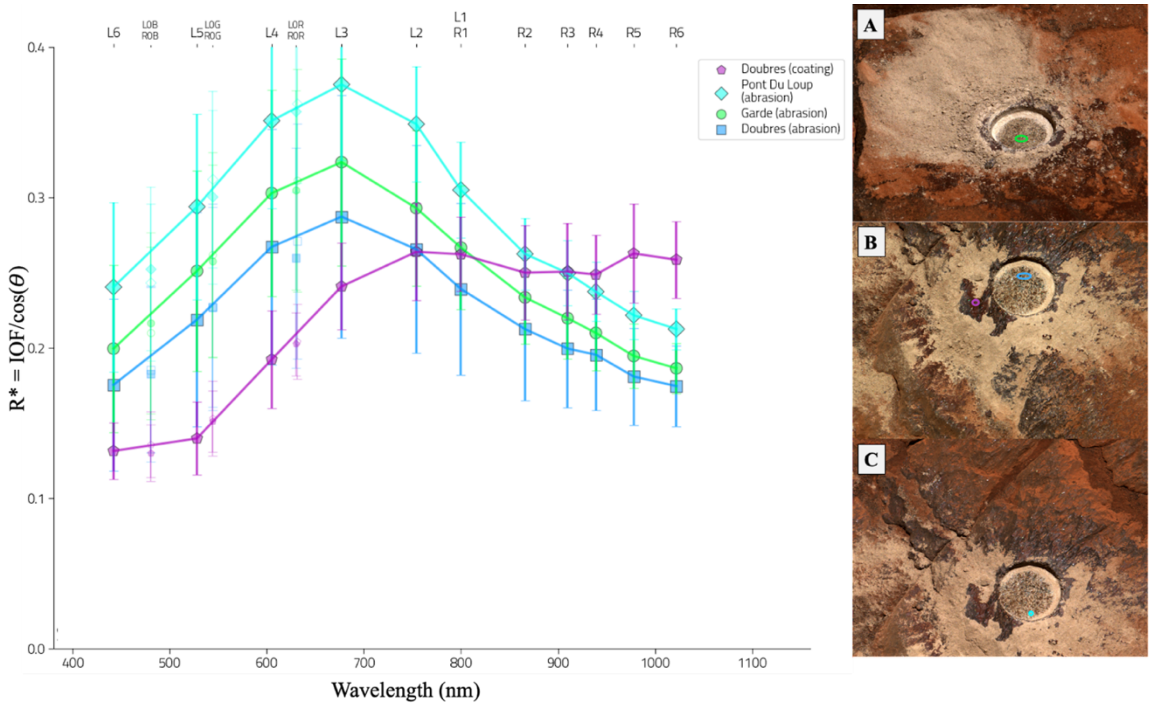

Figure 52: Spectra from three Séítah abrasion patches and one coating. The "error bars" represent variance of the pixels within each ROI and are not showing instrumental error, which is much lower. On the right, three natural color Mastcam-Z context images of the abrasion patches (5 cm diameter) show where the spectra were acquired: (A) the sol 207 Garde abrasion patch, (B) the sol 255 Dourbes abrasion patch, and (C) the sol 268 Pont du Loup partial abrasion. The regions of interest are outlined with circles; colors match the plotted spectra.

DISCUSSION

Changes with Viewing geometry

Reflectance

The viewing geometries where spectra from a sample are brightest (highest reflectances) depend on the sample's scattering behavior. Forward scattering samples are brightest when phase angles are large, and backscattering samples are brightest when phase angles are small. Additionally, normalized spectra from forward scattering samples are relatively flat when phase angle is large. Meanwhile normalized spectra from these same samples have exaggerated reflectance peaks and absorption bands when phase angle is small. Backscattering samples see the same pattern in opposite geometries. This is a quirk of the normalization process. Dividing a full spectrum by the reflectance of a single wavelength brings the reflectance at that wavelength up to 1.0, and the rest of the spectrum is stretched relative to that point. Spectra with low reflectances at the normalization wavelength are stretched further vertically than spectra that start off close to 1.0.

Slope

The near-infrared slope between 1700-2400 nm is more positive in forward scattering geometries and more negative in backscattering geometries for all samples regardless of an individual surface's scattering behavior. This is consistent with findings by Fischer and Pieters (1993) where slope was found to be negative when phase angles are small and positive when phase angles are large, and with Johnson and Grundy (2001) where a negative near-infrared slope was recorded for dark basalts with thin ferric coatings. They suggest that longer wavelengths penetrate deeper into the sample surface, which give samples with coatings a negative slope due to increased sampling of darker substrate material (Fischer and Pieters, 1993;

Johnson and Grundy, 2001). This seems like a logical explanation here, especially for the red dunites and brown andesites which have thin Fe-oxide coatings of various abundances on their surfaces. Extending the discussion to include phase angle, Hoza (2019) suggests forward scattering geometries have more positive slopes because light travels through a sample at shallower depths when phase angle is large, meaning less of the dark substrate is sampled. Not all samples studied here have thin coatings, but the trend still holds true for them, including the interior samples. This indicates bright coatings are not the only cause for the differences in NIR slope, and something else is contributing to the correlation.

Band Centers

Absorption band centers and reflectance peaks shift slightly as viewing geometry changes, but there is no correlation between the band center positions and phase angle. This is important because band center positions are key mineral identification features, and understanding how they change is needed for correction interpretation of spectra. Absorption band depths in cases where the centers can shift over a wide range of wavelengths are shallow and band center movement is most likely due to noise in the spectra. The most consistent band centers are calculated from samples with relatively deep bands or narrow tall peaks (for example: the brown dunites' 1935 nm band).

Band Depth

Band depth decreases with increasing viewing geometry for all samples regardless of other scattering behavior. Absorption bands are shallower and peaks are lower. As a material's grain size increases, initially so does band depth until it reaches a maximum and decreases again due to increased surface reflections (e.g. Clark, 1999). Something similar could be occurring here. Light striking a surface at a wide phase angle is more likely to reflect off the surface than light striking a surface closer to perpendicular, meaning less light is being transmitted through the sample and absorption band depths are shallower.

Changes with Weathering

Compositional Differences

All three rock types have several weathered samples with Fe-oxide-like spectra. The samples with more oxides on their surfaces (according to SEM data) also have the most hematite-like or goethite-like spectra. The difference in Fe-oxide abundance is very small between samples; thin sections and EDS surface maps show that Fe-oxides do not have to coat a surface for spectra to begin looking less like the primary minerals in the rock. In fact, none of the XRD patterns show any Fe-oxides present in the clay-sized portion of the weathering rinds, even the brightest red dunites. Increased surface reddening and Fe-oxide abundance on sample surfaces make the dunites' and andesites' spectra more hematite-like. The basalts' spectra become either hematite-like or goethite-like. The red dunites in particular have absorption bands at ~870 nm and peaks at ~750 nm that are characteristic of hematite (Figure 39).

In the basalt group, DF-18-003-A and FC-18-005, and FC-18-008 have some Fe-oxide-like peaks in the visible wavelengths. All three samples have absorption bands at ~1050 nm. Very shallow absorptions at ~940 nm could indicate the presence of goethite but are unlikely to indicate hematite (Figure 39). Augite is likely overprinting an oxide absorption with a deeper band at 1050 nm; a possible hematite band would be covered up by a pyroxene peak in that region. EDS maps of the surfaces show that Fe-oxides are rare on the basalts. Instead most of the oxides present are ilmenite and titanomagnetite.

The andesite samples progress from most clinopyroxene-like to most Fe-oxide-like from TM-2-A, TM-3, TM-4, to TM-6 (Figure 43). Similar to the dunites, the peak reflectance in the visible range decreases relative to the NIR range with each sample. Hematite's reflectance at 1200 nm and longer wavelengths is much higher than in the visible range. Lower reflectances in the visible range relative to the near-infrared along with peaks at approximately 600 and 750 nm are a sign of the increasing Fe-oxide coatings on these surfaces. The coatings are largely absent from TM-2-A and are most widespread on TM-6, which has the highest near-infrared to 750 nm peak reflectance ratio. Relative to the whole rock composition, the increase in surface Fe-oxide abundance is small but creates large changes in VNIR spectra.

Increasing Reflectance

Most of the weathered samples have overall much higher relative reflectances than the interior and relatively unweathered samples. This increase in albedo appears to be primarily due to textural differences. Published spectra of powdered samples show that reflectance increases as particle size decreases (e.g. Clark, 1999; Carli et al., 2016); this is especially well documented for hematite particles (e.g. Morris et al., 1985; Cudahy and Ramanaidou, 1997). The samples here are whole rock surfaces rather than powders, but the relationship holds true. The reddest samples of each rock type have the smallest grain sizes on their surface. Weathering causes minerals to break down and for new, poorly crystalline oxides and clays to form. The higher ratio of small particles to intact primary minerals on the redder surfaces leads to increases in reflectance.

A couple samples do not fit the trend described above and their surface compositions explain why. The brown dunites have the lowest reflectances out of the dunites through the visible range and only reach reflectance magnitudes comparable to the tan group in the near-infrared wavelengths (Figure 40). This is likely due to their surface compositions, namely the carbon coatings (Figure 16). Graphite spectra are very flat with low reflectances in the VNIR range, and the dark brown dunites have abundant carbon on their surfaces. There is plenty of fine-grained material on these samples, but the carbon is overriding any albedo increase imparted by the surface texture.

TM-2-A is a case where a natural surface has a slightly lower albedo than the interior slab. This is because of slight compositional differences due to incipient weathering. The region where TM-2-A has a noticeably lower reflectance than TM-2-B is in the visible range, specifically around the Fe^{3+} absorption, which pulls down reflectance and creates the steep slope up to 750 nm in all four natural surfaces' spectra (Figure 43). Slight reddening from Fe-oxidation on TM-2-A's surface is the cause of this sample's lower albedo; the Fe^{3+} absorption band darkens the albedo through the visible range. Reflectances increase again in the near-infrared range and overtake the interior slab's reflectance. Similarly, one basalt (FC-18-008) is a weathered slab with nearly the same spectral shape and albedo as its respective interior sample except for in the visible range where the weathered sample is darker due to an Fe^{3+} band (Figure 42). Oxidation in the thin weathering rind is likely causing the Fe^{3+} absorption band; Figure 27 shows where this is occurring in another Frenchman Coulee sample.

Changes in Scattering Behavior with Weathering

Out of the three rock types, dunites have the most extreme shift from forward scattering to backscattering with weathering. The interior slab and TS-20-02-3 are almost entirely forward scattering, while every natural surface with more reddening than TS-20-02-3 is almost entirely backscattering (Figure 45). The dunites also have the most notable color and texture change from relatively unweathered green samples to the weathered red samples. Spectra collected along cross sections using the small diameter probe indicate compositional changes are closely tied to the color change (Figure 41). XRD and SEM data record mostly primary minerals at the surface, but the spectrometer picks up on the small changes that cause the color change.

The basalt interior slab is forward scattering and DF-18-003-A is primarily backscattering (Figure 47). Unlike the dunites, the Frenchman Coulee samples have 2 scattering lobes and are only slightly more backscattering than forward (Figure 47). The highest reflectances from the natural surfaces are in forward scattering geometries, with backscattering geometries producing the second highest reflectances. The andesites all have two scattering lobes, but most are primarily forward scattering while TM-4 is half-and-half (Figure 48).

Textural differences appear to be the primary reason the dunite scattering behavior is bimodal (forward vs. backscattering) while the basalts and andesites are more complex. In sands, increased void space within individual particles leads to stronger backscattering behavior (Souchon et al., 2011); this relationship appears to hold true here for whole rock surfaces. The roughest sample surfaces with the most porous near-surfaces are the most backscattering. All of the weathered dunites have relatively angular surfaces with etch pits in olivine grains that further increase the roughness, making them clearly backscattering (Figures 21 and 45). The basalts' and andesites' more felsic composition is the underlying reason for the surface texture differences; plagioclase and pyroxenes are more resistant to weathering than olivine, so their near-surface porosity at the mineral grain scale is not nearly as high as the dunites and their surfaces tend to be smoother.

If texture is the main driver of scattering behavior, then the smooth coatings on the weathered andesites explain their less backscattering behavior relative to the weathered dunites and basalts. The coatings smooth out sharp angles and fill in pore space that pushes the reflected light into backscattering geometries. TM-4 is both the most backscattering andesite and has the least abundant Fe-oxide coatings, leaving its surface the roughest of the andesites (Figures 37 and 48). Figure 53 compares the surface profiles from randomly selected locations on a red dunite and a brown andesite with abundant coatings. The dunite has more variation in surface height, with much more angular minerals. Images of the surfaces show lots of pits on the dunite (Figure 22) and smooth coatings on the andesite (Figure 36 and 37). The dunite represented by the profile below is strongly backscattering, while the andesite is half forward scattering and half backscattering. An initial step to confirm these changes are texture based and not related to compositional differences between samples could be collecting spectra at many viewing geometries from slabs cut from the same rock and abraded to different grit sizes. Surface roughness is not the same as porosity, but it would be a very attainable first step, and could also indicate if porosity alone is the key factor or if roughness in general plays a part.

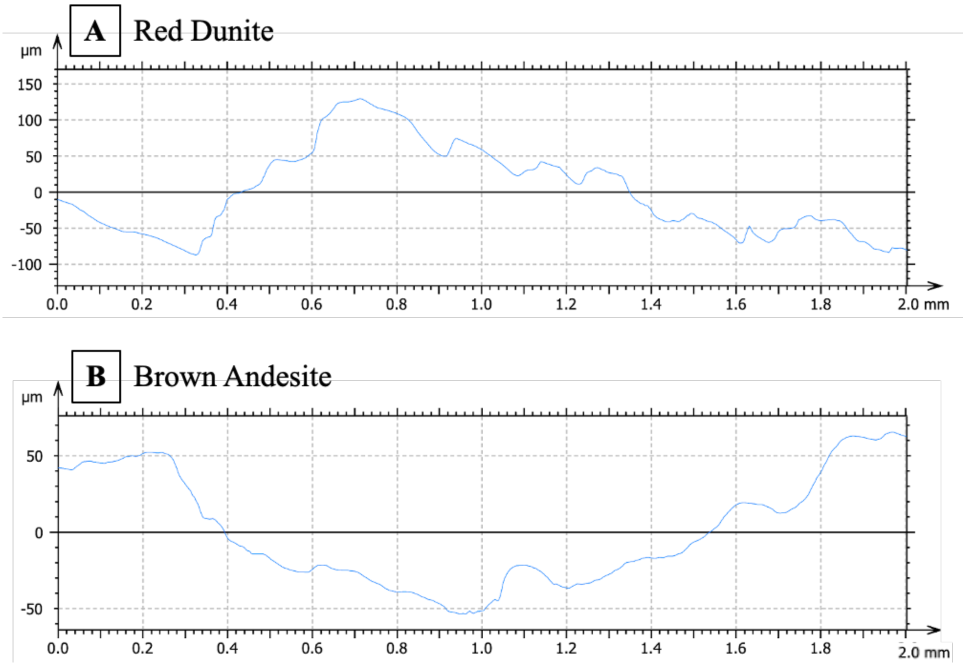

Figure 53: 2 mm wide surface profiles from randomly selected locations on the surfaces of (A) TS-20-05, a red dunite and (B) TM-6, a brown andesite. The profiles were selected from 3D surface reconstructions using MountainsSEM; the zero line or "sea level" is based on the average

in a 2 mm by 2 mm area. The dunite surface is more angular than the andesite with a larger vertical range.

The relationship between microscale textural features and scattering behavior could have applications for Mars remote-sensing experiments. If a multispectral imager like Mastcam-Z or a spectrometer like SuperCam collected a series of observations of a single spot of interest at multiple phase angles, the spectra would contain information about the surface's scattering behavior. A strongly backscattering surface could indicate a relatively high porosity at the sub-mm scale. Ideally this would be done on a dust free surface to avoid its compositional and textural inputs to the recorded spectra.

Comparisons to Mars

Convolving lab spectra to Mastcam-Z wavelengths makes comparisons to Mars data easier (Figure 54). The Séítah abrasion patches have peaks at 677 nm. They line up with 677 nm peaks in the convolved spectra from the tan dunites. The red dunites are more similar to a spectrum from a red-brown coating next to the Dourbes abrasion patch (see Figure 52 for context images). They have a ferric absorption at 866 nm and a slight downturn between the R5 and R6 filters that is the result of hydration.

The dunites are primarily a spectral analog for Séítah, not compositional, because the olivine is more Mg-rich in the dunites. They can still be used to make estimates about the weathering processes the Martian rocks have experienced. The spectral similarities between the tan dunites and Séítah abrasion patches indicate incipient weathering has occurred within Séítah rocks to at least the depth of the abrasion (~2 mm). A Mastcam-Z observation of a dust-cleared natural surface may produce red dunite-like spectra. The abrasion depth is on a similar scale to changes in color and spectra within the red dunite rinds (Figure 41). Their similarity to weathered dunites indicate Séítah rocks likely have backscattering photometric behavior.

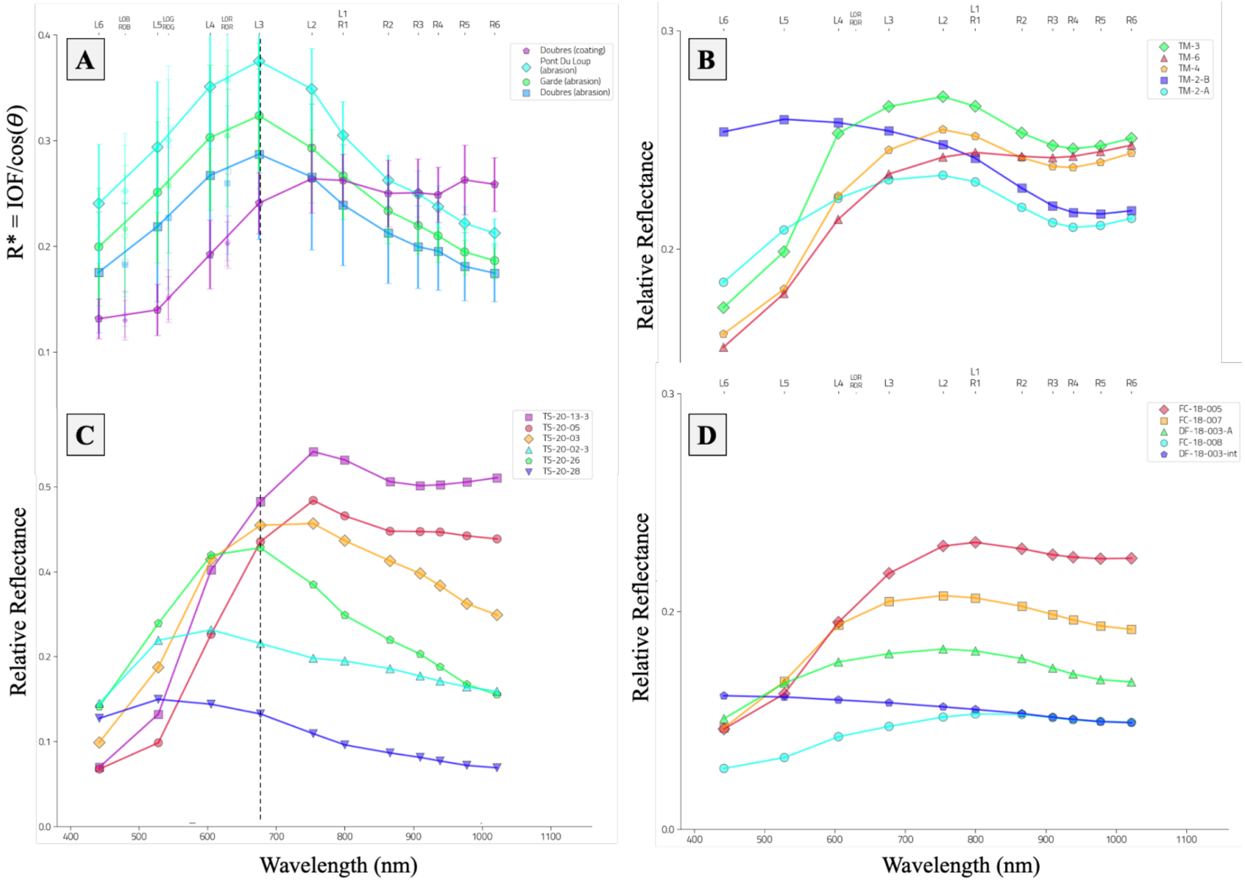

Figure 54: (A) Mastcam-Z spectra from three Séítah abrasion patches and one nearby coating compared to (C) convolved lab spectra from six dunites. Convolved lab spectra from the (B) andesite and (D) basalt slabs are also included for reference.

Known Complications

The lab spectra collected for this thesis used an uncalibrated Spectralon that we had assumed was a perfectly diffuse, Lambertian white reference. As a result, there is a spectral artifact at ~2150 nm where variations in the white reference are not appropriately corrected; it appears as a small peak in that region. A new well-calibrated Spectralon has been acquired and the spectral data is in the process of being recollected without the artifact. Until then, observations and interpretations of spectral features in that region should be confirmed with additional analyses. The data is still very good overall, but mineral identification based on bands and peaks between 2100-2200 nm is challenging. To avoid the problem entirely, spectra can be plotted with a wavelength range of 400-2000 nm.

These analog samples were collected from field sites very different from Mars’ surface. The rocks have been exposed to relatively warm and wet climates for a much shorter period of time. For the most part, rocks on Mars’ surface have been exposed for several billions of years, while the analogs are 93 Ma at their oldest, with post-glacial exposure ages <15 ka. The viewing geometry trends discussed here are expected to hold true despite differences in environment, so long as the sampled rocks share similar surface characteristics (e.g. texture). Care should still be taken when making interpretations on Mars observations using the results here.

Another major difference between the lab samples and Martian rocks, is biologic material on the lab samples. Established techniques to remove biological material from the samples can be time intensive, expensive, and/or hazardous. In the interest of time, the material was left on the samples and its presence is noted where found.

CONCLUSIONS

The main question I set out to answer was: *what are the combined effects of rock surface alteration and viewing geometry on the spectral signature of a subset of naturally weathered igneous rock surfaces?* VNIR spectral changes related to viewing geometry and weathering are:

1. When phase angle is high, absorption band depths decrease and near-infrared slopes are more positive (red sloped). These changes do not affect mineral identification in most cases but recognizing their effect on spectra can make identification easier by removing two complicating factors. There is no correlation between viewing geometry and band center position, but noise can cause some shifting. This is important for interpreting spectra collected at angles much different from lab standard geometries; it indicates spectra collected in those angles can be handled similarly or the same as spectra collected in standard geometry.
2. Weathering alters the composition and texture of rock surfaces, and their VNIR reflectance spectra change as a result. Dunite and andesite spectra become increasingly hematite-like with surface reddening. Thin sections show reddening and the formation of opaque oxides in transmitted light, but SEM analysis reveals relatively few new minerals forming at the surface. Small changes in composition have large effects on the spectra. Weathering textures affect the scattering behavior by changing the way surfaces interact with light compared to relatively unaltered samples. Weathered samples are generally more backscattering than relatively unweathered surfaces and interior slabs. This relationship is most clear in the dunites where the samples are largely homogeneous in composition and differences in composition and/or texture are mainly the result of weathering.

Comparing convolved versions of the lab spectra shows that the tan dunites are a good spectroscopic analog for olivine-rich rocks found in the Séítah region within Jezero crater on Mars. The spectra are olivine-like with peaks shifted to slightly longer wavelengths and show limited hematite-like characteristics. Olivine-rich rocks in Séítah abrasion patches could therefore be ultramafics that have undergone incipient weathering. Their spectral similarities to weathered dunites indicate olivine-rich Séítah rocks will likely exhibit backscattering behavior when viewed at multiple phase angles. Mastcam-Z observations in the Séítah region were taken over a range of viewing geometries; investigating photometric behavior among the Séítah rocks is a logical next step for future studies.

This study focuses on a narrow subset of igneous rocks that have all experienced incipient aqueous alteration. Other rock types and other types of weathering are not addressed here and will be the focus of future studies. Work on sedimentary rocks and sands were started by previous students (e.g. Seppi, 2020; Lapo, 2021) and would be appropriate to revisit now that the hemispheric goniometer is available. Several dunite samples with thick coatings are available for additional study and were not included in this project. My results will allow future studies to expand out to a wide range of rock and weathering types, and they will provide a point of comparison for potentially very different photometric behavior. My results can also be used to form hypotheses for *in situ* viewing geometry experiments on Mars that will provide insight into the weathering history of individual rocks, which will in turn improve our understanding of the planet's geologic history as a whole.

REFERENCES

Baker, L.L., and Neill, O.K., 2017, Geochemistry and mineralogy of a saprolite developed on Columbia River Basalt: Secondary clay formation, element leaching, and mass balance during weathering: American Mineralogist, v. 102, p. 1632–1645, doi:10.2138/am-2017-5964.

Balbas, A.M., Barth, A.M., Clark, P.U., Clark, J., Caffee, M., O'Connor, J., Baker, V.R., Konrad, K., and Bjornstad, B., 2017, 10Be dating of late Pleistocene megafloods and Cordilleran Ice Sheet retreat in the northwestern United States: Geology, v. 45, p. 583–586, doi:10.1130/G38956.1.

Bell, J.F. et al., 2021, The Mars 2020 Perseverance Rover Mast Camera Zoom (Mastcam-Z) Multispectral, Stereoscopic Imaging Investigation: Space Science Reviews, v. 217, p. 24, doi:10.1007/s11214-020-00755-x.

Brown, E. H., 2012, Obducted nappe sequence in the San Juan Islands–northwest Cascades thrust system, Washington and British Columbia: Canadian Journal of Earth Sciences, 49(7), 796-817.

Carli, C., Roush, T.L., Pedrazzi, G., and Capaccioni, F., 2016, Visible and Near-Infrared (VNIR) reflectance spectroscopy of glassy igneous material: Spectral variation, retrieving optical constants and particle sizes by Hapke model: Icarus, v. 266, p. 267–278, doi:10.1016/j.icarus.2015.10.032.

Clark, R.N., 1999, Spectroscopy of Rocks and Minerals, and Principles of Spectroscopy: Manual of Remote Sensing: Remote Sensing for the Earth Sciences, v. 3, p. 3–53.

Colman, S.M., 1982, Chemical Weathering of Basalts and Andesites: Evidence from Weathering Rinds: , p. 57.

Cudahy, T.J., and Ramanaidou, E.R., 1997, Measurement of the hematite:goethite ratio using field visible and near-infrared reflectance spectrometry in channel iron deposits, Western Australia: Australian Journal of Earth Sciences, v. 44, p. 411–420, doi:10.1080/08120099708728322.

Eggleton, R.A., 1987, Weathering of Basalt: Changes in Rock Chemistry and Mineralogy: Clays and Clay Minerals, v. 35, p. 161–169, doi:10.1346/CCMN.1987.0350301.

Ehlmann, B.L. et al., 2009, Identification of hydrated silicate minerals on Mars using MRO-CRISM: Geologic context near Nili Fossae and implications for aqueous alteration: Journal of Geophysical Research: Planets, v. 114, doi:https://doi.org/10.1029/2009JE003339.

Ehlmann, B.L., Mustard, J.F., and Murchie, S.L., 2010, Geologic setting of serpentine deposits on Mars: Geophysical Research Letters, v. 37, doi:https://doi.org/10.1029/2010GL042596.

Ehlmann, B.L., Mustard, J.F., Murchie, S.L., Bibring, J.-P., Meunier, A., Fraeman, A.A., and Langevin, Y., 2011, Subsurface water and clay mineral formation during the early history of Mars: Nature, v. 479, p. 53–60, doi:10.1038/nature10582.

Ehlmann, B.L., and Edwards, C.S., 2014, Mineralogy of the Martian Surface: Annual Review of Earth and Planetary Sciences, v. 42, p. 291–315, doi:10.1146/annurev-earth-060313-055024.

Fischer, E.M., and Pieters, C.M., 1993, The Continuum Slope of Mars: Bidirectional Reflectance Investigations and Applications to Olympus Mons: Icarus, p. 185–202.

Frasse, F.I., 1981, Geology and Structure of the Western and Southern Margins of Twin Sisters Mountain, North Cascades, Washington: WWU Graduate School Collection, 639. https://doi.org/10.25710/45d4-eq31

Greenberger, R.N., Mustard, J.F., Kumar, P.S., Dyar, M.D., Breves, E.A., and Sklute, E.C., 2012, Low temperature aqueous alteration of basalt: Mineral assemblages of Deccan basalts and implications for Mars: Journal of Geophysical Research: Planets, v. 117, doi:10.1029/2012JE004127.

Hayes, A.G. et al., 2021, Pre-Flight Calibration of the Mars 2020 Rover Mastcam Zoom (Mastcam-Z) Multispectral, Stereoscopic Imager: Space Science Reviews, v. 217, p. 29, doi:10.1007/s11214-021-00795-x.

Hildreth, W., Fierstein, J., and Lanphere, M., 2003, Eruptive history and geochronology of the Mount Baker volcanic field, Washington: Geological Society of America Bulletin, v. 115, p. 729–764, doi:10.1130/0016-7606(2003)115<0729:EHAGOT>2.0.CO;2.

Horgan, B.H.N., Smith, R.J., Cloutis, E.A., Mann, P., and Christensen, P.R., 2017, Acidic weathering of basalt and basaltic glass: 1. Near-infrared spectra, thermal infrared spectra, and implications for Mars: Journal of Geophysical Research: Planets, v. 122, p. 172–202, doi:10.1002/2016JE005111.

Horgan, B.H.N., Anderson, R.B., Dromart, G., Amador, E.S., and Rice, M.S., 2020, The mineral diversity of Jezero crater: Evidence for possible lacustrine carbonates on Mars: Icarus, v. 339, p. 113526, doi:10.1016/j.icarus.2019.113526.

Hoza, K., 2019, Photometric investigations of weathering rinds and coatings with implications for Mars: *WWU Graduate School Collection*, Master's Thesis, Western Washington University, Bellingham, Washington, https://cedar.wwu.edu/wwuet/921.

Hurowitz, J.A., McLennan, S.M., Tosca, N.J., Arvidson, R.E., Michalski, J.R., Ming, D.W., Schröder, C., and Squyres, S.W., 2006, In situ and experimental evidence for acidic weathering of rocks and soils on Mars: Journal of Geophysical Research: Planets, v. 111, doi:10.1029/2005JE002515.

Hurowitz, J.A., and McLennan, S.M., 2007, A ~3.5 Ga record of water-limited, acidic weathering conditions on Mars: Earth and Planetary Science Letters, v. 260, p. 432–443, doi:10.1016/j.epsl.2007.05.043.

Jackson, M. L. (2005). Soil Chemical Analysis: advanced course. UW-Madison Libraries parallel press.

Johnson, J.R., and Grundy, W.M., 2001, Visible/Near-Infrared Spectra and Two-Layer Modeling of Palagonite-Coated Basalts: Geophysical Research Letters, v. 28, p. 2101–2104.

Johnson, J.R., Grundy, W.M., and Shepard, M.K., 2004, Visible/near-infrared spectrogoniometric observations and modeling of dust-coated rocks: Icarus, v. 171, p. 546–556, doi:10.1016/j.icarus.2004.05.013.

Kinch, K.M. et al., 2020, Radiometric Calibration Targets for the Mastcam-Z Camera on the Mars 2020 Rover Mission: Space Science Reviews, v. 216, p. 141, doi:10.1007/s11214-020-00774-8.

Kraft, M.D., Michalski, J.R., and Sharp, T.G., 2003, Effects of pure silica coatings on thermal emission spectra of basaltic rocks: Considerations for Martian surface mineralogy: Geophysical Research Letters, v. 30, doi:10.1029/2003GL018848.

Lapo, Kristiana, "Martian Spectroscopy: Laboratory calibration of the Perseverance rover's Mastcam-Z and photometric investigation of Mars-analog ferric-coated sand" (2021). *WWU Graduate School Collection*. 1011. https://cedar.wwu.edu/wwuet/1011

Maurice, S. et al., 2021, The SuperCam Instrument Suite on the Mars 2020 Rover: Science Objectives and Mast-Unit Description: Space Science Reviews, v. 217, p. 47, doi:10.1007/s11214-021-00807-w.

Minitti, M.E., Weitz, C.M., Lane, M.D., and Bishop, J.L., 2007, Morphology, chemistry, and spectral properties of Hawaiian rock coatings and implications for Mars: Journal of Geophysical Research, v. 112, p. E05015, doi:10.1029/2006JE002839.

Michalski, J.R., Kraft, M.D., Sharp, T.G., and Christensen, P.R., 2006, Effects of chemical weathering on infrared spectra of Columbia River Basalt and spectral interpretations of martian alteration: Earth and Planetary Science Letters, v. 248, p. 822–829, doi:10.1016/j.epsl.2006.06.034.

Million, C.C., St. Clair, M., Rice, M., and Vaughn, A., 2022, Software tools for rapid analysis of Mastcam-Z multispectral data: 53rd Lunar and Planetary Society Conference, abstract 2533.

Moeller, R.C. et al., 2020, The Sampling and Caching Subsystem (SCS) for the Scientific Exploration of Jezero Crater by the Mars 2020 Perseverance Rover: Space Science Reviews, v. 217, p. 5, doi:10.1007/s11214-020-00783-7.

Moore, N.E., and DeBari, S.M., 2012, Mafic magmas from Mount Baker in the northern Cascade arc, Washington: probes into mantle and crustal processes: Contributions to Mineralogy and Petrology, v. 163, p. 521–546, doi:10.1007/s00410-011-0686-4.

Morris, R.V., Lauer Jr., H.V., Lawson, C.A., Gibson Jr., E.K., Nace, G.A., and Stewart, C., 1985, Spectral and other physicochemical properties of submicron powders of hematite (α-Fe2O3), maghemite (γ-Fe2O3), magnetite (Fe3O4), goethite (α-FeOOH), and lepidocrocite (γ-FeOOH): Journal of Geophysical Research: Solid Earth, v. 90, p. 3126–3144, doi:10.1029/JB090iB04p03126.

Mustard, J.F. et al., 2008, Hydrated silicate minerals on Mars observed by the Mars Reconnaissance Orbiter CRISM instrument: Nature, v. 454, p. 305–309, doi:10.1038/nature07097.

Nesbitt, H.W., and Wilson, R.E., 1992, Recent chemical weathering of basalts: American Journal of Science, v. 292, p. 740–777, doi:10.2475/ajs.292.10.740.

Nuñez, J et al., 2022, Stratigraphy and Mineralogy of the Deposits Within Séítah Region on the Floor of Jezero Crater, Mars as Seen With Mastcam-Z: 53rd Lunar and Planetary Society Conference, abstract 2937.

Onyeagocha, A.C., 1978, Twin Sisters dunite: Petrology and mineral chemistry: Geological Society of America Bulletin, v. 89, p. 1459–474.

Poppe, L.J., Fredericks, J.J., and Hathaway, J.C., 1988, A computer program to calculate centrifugation parameters for sedimentation analyses: Computers & Geosciences, v. 14, p. 541–545, doi:10.1016/0098-3004(88)90034-9.

Poppe, L. J., Paskevich, V. F., Hathaway, J. C., & Blackwood, D. S. (2001). A laboratory manual for X-ray powder diffraction. US Geological Survey open-file report, 1(041), 1-88.

Ragan, D.M., 1963, Emplacement of the Twin Sisters dunite, Washington: American Journal of Science, v. 261, p. 549–565, doi:10.2475/ajs.261.6.549.

Reidel, S.P., Spane, F.A., and Johnson, V.G., 2002, Natural Gas Storage in Basalt Aquifers of the Columbia Basin, Pacific Northwest USA: A Guide to Site Characterization: PNNL-13962, 15020781, PNNL-13962, 15020781 p., doi:10.2172/15020781.

Rice, M. S., J. R. Johnson, C. C. Million, M. St. Clair, B. N. Horgan, A. Vaughan, J. I. Núñez, B. Garczynski, S. Curtis, K. M. Kinch, A. Hayes and J. F. Bell, 2022a, Summary of

Mastcam-Z Visible to Near Infrared (VNIR) Multispectral Observations from Perseverance's Mission in Jezero Crater, Mars: 53rd Lunar and Planetary Society Conference, abstract 2559.

Rice, M.S., Hoza, K., and Lapo, K., 2022b, Tanager: An Automated Spectrogoniometer for Bidirectional Reflectance Studies of Natural Rock Surfaces: 53rd Lunar and Planetary Society Conference, abstract 2570.

Salvatore, M.R., Mustard, J.F., Head, J.W., Cooper, R.F., Marchant, D.R., and Wyatt, M.B., 2013, Development of alteration rinds by oxidative weathering processes in Beacon Valley, Antarctica, and implications for Mars: Geochimica et Cosmochimica Acta, v. 115, p. 137–161, doi:10.1016/j.gca.2013.04.002.

Salvatore, M.R., and Christensen, P.R., 2014, Evidence for widespread aqueous sedimentation in the northern plains of Mars: Geology, v. 42, p. 423–426, doi:10.1130/G35319.1.

Sautter, V. et al., 2015, In situ evidence for continental crust on early Mars: Nature Geoscience, v. 8, p. 605–609, doi:10.1038/ngeo2474.

Seppi, Isabella, "Spectral Variability of Weathered Basalts and Sandstones" (2020). *WWU Honors College Senior Projects*. 399. https://cedar.wwu.edu/wwu_honors/399

Singer, R.B., 1982, Spectral evidence for the mineralogy of high-albedo soils and dust on Mars: Journal of Geophysical Research: Solid Earth, v. 87, p. 10159–10168, doi:10.1029/JB087iB12p10159.

Smith, K.L., Milnes, A.R., and Eggleton, R.A., 1987, Weathering of Basalt: Formation of Iddingsite: Clays and Clay Minerals, v. 35, p. 418–428, doi:10.1346/CCMN.1987.0350602.

St. Clair, M., Million, C., Rice, M.; *marslab* software suite (2022); https://zenodo.org/badge/latestdoi/498892781

Thordarson, T., and Self, S., 1998, The Roza Member, Columbia River Basalt Group: A gigantic pahoehoe lava flow field formed by endogenous processes? Journal of Geophysical Research: Solid Earth, v. 103, p. 27411–27445, doi:10.1029/98JB01355.

Toy, V.G., Newman, J., Lamb, W., and Tikoff, B., 2010, The Role of Pyroxenites in Formation of Shear Instabilities in the Mantle: Evidence from an Ultramafic Ultramylonite, Twin Sisters Massif, Washington: Journal of Petrology, v. 51, p. 55–80, doi:10.1093/petrology/egp059.

Velbel, M.A., 2009, Dissolution of olivine during natural weathering: Geochimica et Cosmochimica Acta, v. 73, p. 6098–6113, doi:10.1016/j.gca.2009.07.024.

Wyatt, M.B., and McSween, H.Y., 2002, Spectral evidence for weathered basalt as an alternative to andesite in the northern lowlands of Mars: Nature, v. 417, p. 263–266, doi:10.1038/417263a.

Yang, Y., Lin, H., Liu, Y., Lin, Y., Wei, Y., Hu, S., Yang, W., Xu, R., He, Z., and Zou, Y., 2020, The Effects of Viewing Geometry on the Spectral Analysis of Lunar Regolith as Inferred by in situ Spectrophotometric Measurements of Chang'E-4: Geophysical Research Letters, v. 47, p. e2020GL087080, doi:10.1029/2020GL087080.

Zhou, K.-F., and Wang, S.-S., 2017, Spectral properties of weathered and fresh rock surfaces in the Xiemisitai metallogenic belt, NW Xinjiang, China: Open Geosciences, v. 9, p. 322–339, doi:10.1515/geo-2017-0027.